Transient x-ray and ultraviolet phenomena in solar polar coronal holes

DOTTORATO DI RICERCA IN FISICA E ASTRONOMIA

CICLO XXVI

COORDINATORE Prof. Livi Roberto

Transient X-Ray and Ultraviolet Phenomena in Solar Polar Coronal Holes

Settore Scientifico Disciplinare FIS/05

Dottorando
Dott. Pucci Stefano

Tutore
Dott. Romoli Marco

Coordinatore
Prof. Livi Roberto

Anni 2011/2014

Abstract

In the last few years several new missions have been developed and launched to observe our star in order to understand the physical processes that dominate the plasma dynamics of the solar atmosphere. These missions have provided solar scientists with unprecedented high temporal and spatial resolution images of the Extreme UltraViolet (EUV) and X-rays corona. In these thesis we have focussed on the study of transient phenomena within coronal holes (CH) that can be observed with the imaging instruments on board of these new missions.

In the first three chapters of this thesis we give an introduction to these transient phenomena and to their studies by means of observations of their EUV and X-rays emissions, we describe the main characteristics of the missions and of the instruments whose data have been analysed in this work and we review the diagnostics techniques that have been adopted to derive the plasma parameters of the observed features.

In the second part of this thesis we present in detail the observations, the methods and the results of the three main works that have been carried out during the PhD. Three main publications, that are here presented, resulted from these works.

In the first work we present an analysis of X-ray Bright Points (BPs) and X-ray jets observed by *Hinode/X-Ray Telescope* (XRT) on November 2–4 2007, within the solar northern polar CH. After selecting small subregions that include several BPs, we followed their brightness evolution over a time interval of a few hours, when several jets were observed. We find that most of the jets occurred in close temporal association with brightness maxima in multiple BPs: more precisely, most jets are closely correlated with the brightening of at least 2 BPs. We suggest that the jets result from magnetic connectivity changes that also induce the BP variability. We surmise that the jets and implied magnetic connectivity we describe are small-scale versions of the active-region-scale phenomenon whereby flares and eruptions are triggered by interacting bipoles.

The second work is still based on data from the *Hinode* XRT which re-

vealed the occurrence, in polar coronal holes, of much more numerous jets than previously indicated by the *Yohkoh*/*Soft X-ray Telescope*. These plasma ejections can be of two types, depending on whether they fit the standard reconnection scenario for coronal jets or if they include a blowout-like eruption. In this second work we analyze two jets, one standard and one blowout, that have been observed by *Hinode* and *STEREO* experiments, aiming at inferring differences in physical parameters that correspond to the different morphology of the events. To this end we adopt spectroscopic techniques and give the profiles of plasma temperature, density and outflow speed vs. time and position along the jets. It turns out that the blowout jet has a higher outflow speed, marginally higher temperature and is rooted in a stronger magnetic field region than the standard event. Our data provide evidence for recursively occurring reconnection episodes within both the standard and the blowout jet, pointing either to bursty reconnection or to reconnection occurring at different locations over the jet lifetimes. We make a crude estimate of the energy budget of the two jets and show how energy is partitioned among different forms. Also, we show that the magnetic energy that feeds the blowout jet is a factor 10 higher than the magnetic energy that fuels the standard event.

In the third work we analyze a solar polar-coronal-hole plume over its entire $\approx$ 40 h lifetime, using high resolution *Solar Dynamic Observatory* (SDO) *Atmospheric Imaging Assembly* (AIA) data. We examine (1) the plume's relationship to a bright point (BP) that persists at its base, (2) plume outflows and their possible contribution to solar wind mass supply, and (3) physical properties of the plume. We find that the plume started $\approx$2 h after the BP first appeared and became undetectable $\approx$1 h after the BP disappeared. We detected radially-moving radiance variations from both the plume and from interplume regions, corresponding to apparent outflow speeds ranging over $\approx$(30 to 300) km s^{-1} with outflow velocities being higher in the "cooler" AIA 171 Å channel than in the "hotter" 193 Å and 211 Å channels, which is inconsistent with wave motions; therefore we conclude that the observed radiance variations represent material outflows. If they persist into the heliosphere and plumes cover $\approx$10 % of a typical coronal hole area, these flows could account for $\approx$50 % of the solar wind mass. From a Differential Emission Measure analysis of the AIA images, we find that the average electron temperature of the plume remained approximately constant over its lifetime, at $T_{\rm e} \approx 8.5 \times 10^5$ K. Its density however decreased with the age of the plume, being about a factor-of-three lower when the plume faded compared to when it was born. We conclude that the plume died due to a density reduction rather than to a temperature decrease.

Contents

Chapter 1

Introduction

In this thesis we study small-scale short lived structures that are observed within polar Coronal Holes (CH) of the Sun. These structures that emit at X-ray and Extreme UltraViolet (EUV) wavelengths, are the smallest evidences of the solar activity, and hence strongly related with the solar cycle. The aim of this work is thus twofold: first, we determine the physical parameters of plasma in these transient phenomena, and then we examine the role that these structures play in one of the most important open questions of Solar Physics, i.e. the acceleration and mass supply of the Solar Wind (SW).

The first step of this chapter is a description of the environment hosting these structures, namely the solar corona and its polar CHs, followed by the morphological characterization of the structures.

1.1 The Solar Corona

Our Sun is by far the nearest star, and thus, in addition to play a key role for the subsistence of life on Earth, it represents a backyard laboratory to study the extremely fascinating physics of stars.

The layer of the Sun that emits most of the energy that reaches the Earth is called *photosphere*. Such energy is emitted mostly at visible wavelengths, and its spectrum has been studied for long time. Furthermore, the observation of the photosphere has revealed the presence of transient features (e.g. sunspots[1]), whose study can be carried out directly from the Earth surface, and has been one of the milestones in the birth of modern science. More than two hundred years of reliable and continuous observations of Sunspots have

[1]The study of these dark regions that can be easily observed on the solar disk led Galileo in 1612 to assume that the Sun was rotating and in contrast with Aristotle, changing with time.

shown that their number follows a periodic trend, going from a minimum to a maximum phase and then back to minimum in nearly 11 years. These two centuries of regular observations have also shown that such periodic development, known as *solar cycle*, is not only related to photospheric Sunspots, rather concerning the overall solar activity and its magnetic field. Indeed, by observing the spectrum of light coming from Sunspots, the observers could notice that some spectral line appeared as strongly splitted[2], revealing an important role of the magnetic field in the generation of Sunspots and thus in controlling the solar cycle.

Above the photosphere, the solar atmosphere has been historically divided, on the base of eclipse observations, in *chromosphere* and *corona*, which are separated by a thin layer called *transition region*.

The corona, that is the target of our work, differently from the Earth atmosphere, is not confined in a thin layer. It rather merges into the interplanetary medium, extending beyond solar planets and filling the heliosphere with a stream of ions and electrons, escaping from the Sun, that is called *solar wind* (SW).

The brightness of the corona, is several order of magnitude lower than the emission of the day sky (Kimura & Mann, 1998, e.g.). Hence, the corona has been historically studied during solar eclipses, when the solar disk is occulted by the moon and the emission from the Earth atmosphere is almost totally avoided.

Such observations, that have been performed since the middle of the nineteenth century, showed a spectrum characterized by unidentified spectral lines that led the observers to postulate the existence of a new atomic element, called "Coronium". Only after about 50 years the "new" lines were identified as forbidden lines produced by ions of well known elements in highly ionization states. This implied an extremely high coronal temperature, of the order of million degrees, and an unexpected temperature increase of two-three orders of magnitude from the photosphere to the corona.

Because of such a high temperature, the plasma of the corona emits strongly in UltraViolet (UV) and X-Rays, a region of the spectrum where the day sky does not emit. On the other hand, radiation at these frequencies is almost completely absorbed by the upper layer of the Earth atmosphere, that acts as a shield protecting the Earth surface from this extremely energetic radiation.

Hence, in order to be able to observe the corona continuously, and not only during solar eclipses, out-of-atmosphere observations are required. Further-

[2]Because of the Zeeman effect a strong magnetic field is able to remove the degeneracy of atomic energy levels causing the splitting of certain spectral lines.

more, observations of the Sun at these high frequencies, where the emission from the corona overcomes that of the photosphere, allows for the first time the study of solar corona on disk.

The first out-of-atmosphere data of the solar corona were taken via spectrographs onboard of rocket flights launched by the Naval Research Laboratory (NRL), for UV and X-rays respectively in 1946 already and in 1963 (Mártínez Pillet et al., 2005; Friedman, 1963) These short observations (no more than 10 minutes) and the following rocket experiments allowed the first measurements of electron temperature and density of the coronal plasma, confirming the hypothesis of an extremely hot corona.

A new era of space-observations started with the launch of the space station Skylab in 1973 (Lundquist, 1979), by the National Aeronautics and Space Administration (NASA), that carried on board the Apollo Telescope Mount (ATM), a package that included a white light coronograph, X-ray telescopes and an UV and EUV spectrograph. The first ever images of the X-ray corona led to great progresses in the understanding of the solar corona.

After Skylab, a great number of space missions was dedicated to the study of the Sun, each mission providing a wealth of higher quality observations and leading to an improvement of the understanding of the Sun and its atmosphere. Among them, a key role in the study of the corona was played by the Solar Maximum Mission (1980-1989, Bohlin et al., 1980), the *Yohkoh* mission (1991-2001, Ogawara et al., 1991), the Solar and Heliospheric Observatory (*SOHO*, 1995-today, Domingo et al., 1995). At the present several very important and successful missions are observing the Sun. In our work we use data from the three most important missions of these years: the *Hinode* mission (2006-today), the *STEREO* mission (2006-today), and the Solar Dynamic Observatory (2010-today), which will be described in sections 2.1, 2.2 and 2.3 respectively.

In spite of the huge amount of new observational data collected by these missions and of the improved understanding that has been obtained thanks to the international community of solar scientists, some crucial topics remain still unclear, making the Solar Physics a very exciting branch of the modern science. Which are the physical processes that produce such a high temperature plasma in the corona? and how the solar wind is created and accelerated? In particular in this work we will analyze a few coronal transient phenomena in an effort to acquire additional information that might improve our understanding of solar wind origin and acceleration.

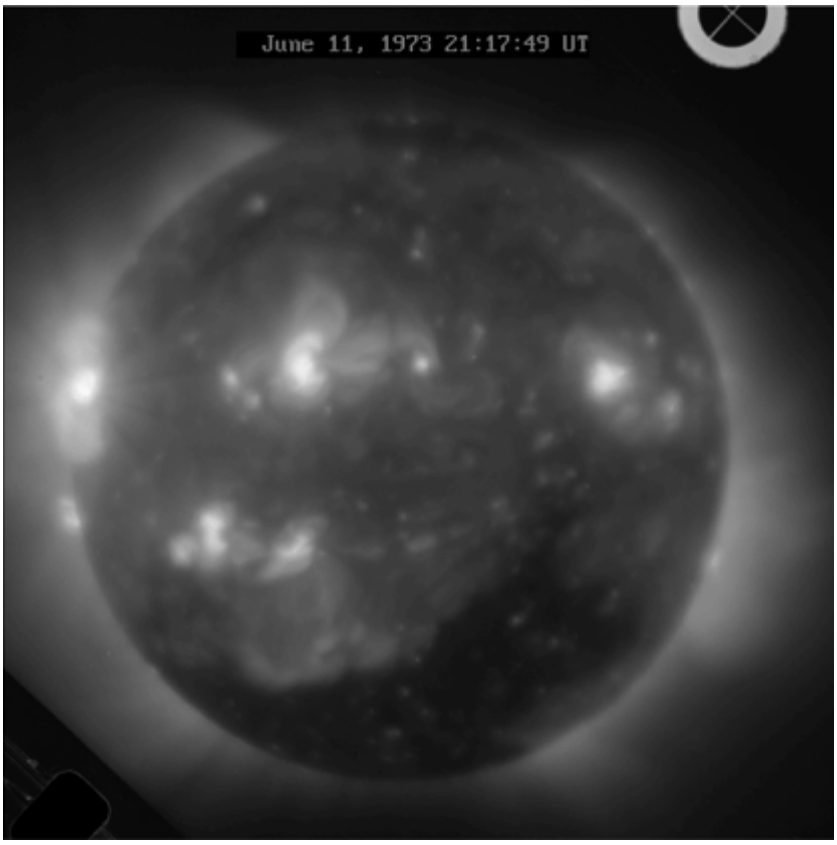

Figure 1.1 The X-ray corona as observed from the x-ray telescope on board of the *Skylab* mission.

1.2 Coronal Holes

Fig.1.1 shows an image of the X-ray corona taken by the x-ray telescope on board of the Skylab on 11 June 1973.

Already from this early image we can observe that the X-ray corona, rather than being uniform, is characterized by localized strong emission regions, often located at low latitude and associated with the so called *active regions*[3] (AR), a quite continuos background of emission, called the *quiet sun* (QS) that is somewhere abruptly interrupted by dark regions, called *coronal holes* (CH).

CHs develop more often during minimum of solar activity and around the poles of the Sun, taking the name of polar CH, but can also be observed at

[3]Groups of coronal loop-structured features that are rooted in photospheric Sunspots of opposite magnetic polarity.

lower latitude (equatorial CH).

Lower densities characterize the plasma within CHs, causing a weaker X-ray emission, compared to the other parts of the corona. The understanding of CHs is tied to the study of the solar magnetic field which regulates how this coronal feature is related to the solar wind. On a global scale the magnetic field of the Sun at its minimum phase can be compared with a bipolar magnetic field produced by a current loop, where high-latitudes magnetic field lines emerging from the poles can be considered to be open field lines while closed loops are constituted by lower-latitude closed field lines. Due to the Lorentz force charged particles are bounded to follow spiral trajectories around magnetic field lines. Hence, closed magnetic field lines act as a trap for the plasma of the solar atmosphere, while, along open magnetic field lines, charged particles can escape from the Sun into the interplanetary space and eventually reach the Earth.

Several years of in-situ space-borne measurements of the composition and velocities of the solar wind combined with remote sensing observations of the X-ray corona has confirmed that CHs are located in regions of open magnetic field, and hence constitute an important source for the high velocity regime of solar wind, called *fast solar wind* (Balogh & Forsyth, 1998). Such regime is characterized by higher and less variable velocity values of the ion stream and is specific of the minimum phase of the solar cycle.

1.3 Bright Points

A careful observation of a CH shows that even within this dark area a lot of small roundish X-ray emitting features can be found. These emitting spots, dubbed *bright points* (BPs), have been identified by Vaiana et al. (1970) from images of rocket-borne X-ray telescopes. With the first space data from the S-054 X-ray Telescope on board of the Skylab mission, Golub et al. (1974) carried out a detailed study on BPs, focussing on their lifetime, appearance and dimensions. Because they represent the small-scale end of ARs, BPs have been subject of a large number of studies that have tried to enlighten both physical/morphological aspects of these features and their role in local and global dynamics of the corona.

BPs appear as spots of dimension that can typically vary from few to 30" and are often characterized by an unresolved bright core smaller than 5". They can be observed at all solar latitudes and their daily number varies from several hundreds and up to few thousands (Golub et al., 1974).

Early after their discovery, BPs have been correlated with small-scale bipolar magnetic features that emerge in the ambient magnetic field. Indeed,

the comparison of X-ray observations with magnetic field measurements has shown that BPs and bipoles are almost cospatial. The fact that BP are observed at all latitude, both inside and outside CHs, suggests that these small bipolar magnetic features emerge independently of the characteristics of the ambient magnetic field that hosts them. Furthermore, the existence of BPs within CHs points out that solar magnetic activity is characterized by different scales: on one hand the global magnetic field and its open field lines that emerge from the photosphere in correspondence of CH, on the other hand small magnetic bipoles that emerge giving rise to BPs.

By comparing series of S-045 Skylab images, Golub et al. (1974) found that BPs are characterized by a mean lifetime that follows a Poisson distribution, reaching up to 30 hours and with an average value of 8 hours. During this time BPs follow often a standard evolution pattern, in which the spot appears first as a diffuse cloud, then, in a second stage, a bright core (usually not larger than 10") becomes visible in the middle of the cloud, and finally both the cloud and bright core disappear.

BPs are also characterized by significant luminosity fluctuations, that contribute to the variability in luminosity of the overall X-ray corona. These intensity oscillations have been carefully studied and their typical time-scale varies from few minutes to hours (Kariyappa & Varghese, 2008). It has been shown that these variations are often associated with temperature oscillations and thus, probably, variations in the energy deposition efficiency.

Some studies have shown that the plasma filling a BP is usually characterized by temperatures of about 2×10^6 K and electron densities of $n_e = 5\times10^{-9}$ cm^{-3} (Golub & Pasachoff, 1997), but cooler BP have been observed (Habbal et al., 1990).

In this time-interval, BPs radiate energy via X-ray and UV emission, and as suggested by models, also the thermal conduction towards the cooler chromosphere plays an important role in the energy balance of BPs (Habbal et al., 1990). These energy losses need to be balanced by an energy source that must heat the plasma in order to justify its bright emission over its lifetime.

It is still not well understood which are the causes of temperature and luminosity fluctuations and how these changes are related with the morphology evolution of BPs and the related plasma properties. Furthermore there is a lack of studies about the relationship between BPs and other features in CHs, and how activity in BPs can cause/trigger variations in nearby structures. The understanding of BPs is important from a global point of view as probes of the larger-scale magnetic environment.

In our work we will focus on determining the relation between BPs luminosity oscillations and occurrence/variation in other CH structures like X-ray

jets (see Par. 1.4) and polar plumes (see Par. 1.5).

1.4 Coronal jets

The breakthrough in X-ray observations of the solar corona carried out by the SXT Telescope on board of the *Yohkoh* mission has shifted the focus of X-ray coronal studies from steady or at least slowly varying features, to fast varying, short lived events. Indeed, the first SXT images, showed that both the QS corona and CHs are full of transient x-ray enhancements characterized by an apparent collimated motion. These transient phenomena, called X-ray coronal jets, were first reported by Shibata et al. (1992) (see Fig. 1.2) and since their discovery, they have rised the interest of solar scientists. The XRT on board of the *Hinode* mission, due to its higher spatial and temporal resolution, detected a much larger number of X-ray jets than previously expected. Indeed, the estimated occurrence rate increased from 20 jets per month (Shibata et al., 1992) to 10 jets per hour (Cirtain et al., 2007).

X-ray jets have been found for the first time in full frame SXT images, with a 5" space resolution and time resolution ranging from few minutes to hours. Such jets presented a typical size of $5 \times 10^3 - 4 \times 10^5$ km (Shibata et al., 1992) an average length of 2×10^5 km and apparent velocity of 200 km s^{-1} (Shimojo et al., 1996). Later, Savcheva et al. (2007) used data from a coordinate *Hinode*/*SOHO* campaign to carry out an extensive study of the formation and evolution of X-ray polar jets. From a statistical study on a large number of jets, they found that a typical jet is 5×10^4 km high, 8×10^3 km wide and lasts 10 minutes. Furthermore they found that such a typical event shows evidence for apparent outward flows at a mean velocity of 160 km s^{-1}, and a transverse motion with velocities ranging from 0 to 35 km s^{-1}. These authors claim that these new values, being obtained on the basis of a larger and higher quality statistical set of events compared with Shimojo et al. (1996), are more accurate and can be better trusted.

X-ray jets are often observed in region where there is evidence for emerging magnetic flux. The morphology of the jet depends on the ambient field where the new flux is emerging. When the pre-existing magnetic field extends horizontally the resulting jet forms horizontally toward both sides of the emerging flux (two sided-loop jets) On the other hand, if the ambient field is characterized by open lines (i.e. the typical field configuration of a CH) the interaction between the emerging flux and the vertical pre-existing field produces a vertical shaped jets. This second sort of jets, on the basis of their manifold geometries have been dubbed with different names: Eiffel jets (symmetric), lambda-jets (asymmetric) and Anemone jets (cylindrical

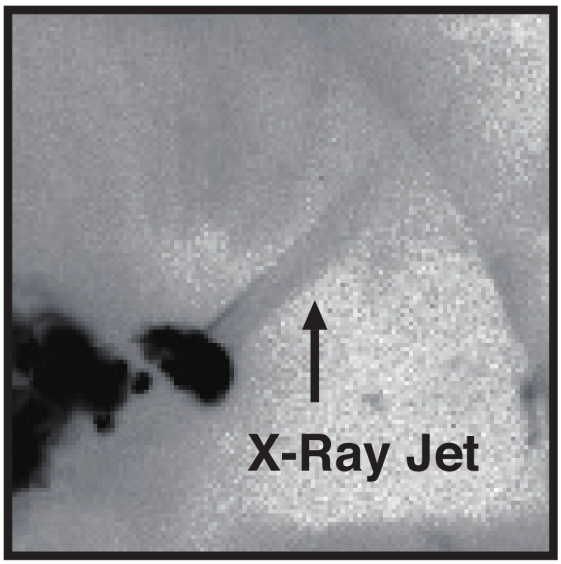

Figure 1.2 An X-ray jet imaged by the Soft X-Ray Telescope on board of the *Yohkoh* mission, shown with inverted colors. From (Shibata et al., 1992).

symmetric). In this work we will focus on vertical jets that originate in CHs.

Since the first observations, a standard model has been proposed to describe the common morphology that identifies most of the jets. Indeed, many jet events share a common behavior where 1) a BP is observed flaring on a side of the jet and 2) during the evolution of the event, the jet spire is observed to migrate away from the flaring BP.

In the cartoon by Moore et al. (2010) shown in Fig. 1.3 the magnetic configuration of a standard jet event is shown. Only the most representative field lines are drawn, with blue and red lines. The first panel shows how the magnetic field looks like before the jet event takes place. A bipole (closed field lines) is emerging within a negative unipolar ambient field (open vertical field lines). The polarity inversion line is represented by the dashed oval that encloses the positive flux. The emergence of magnetic arch in the ambient field has caused the formation of a current sheet, here represented by a small curved black segment. In the second panel the magnetic arch continues to

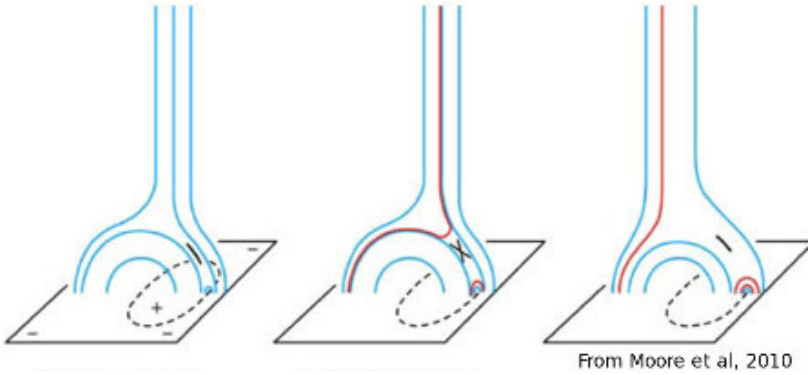

Figure 1.3 A cartoon sequence depicting the phases of the standard model for X-ray jets. Blue and red lines represent normal and reconnected magnetic field lines. The inversion polarity line is represented by the dashed oval. The curved black segment stands for a portion of the current sheet before reconnection, while the slanted X is the collapsed current sheet during reconnection. From Moore et al. (2010).

emerge, causing the instability of the current sheet. This collapsed current sheet is now represented by an X and the burst due to magnetic reconnection heats the plasma to such a high temperature that it emits strongly in X-ray. This hot plasma is confined within reconnected field lines (red lines), that are released both upward and downward. The upward reconnected lines are open field lines that contain the hot plasma forming the jet spire. On the other hand, the remaining reconnected lines form new X-ray flaring bipoles located over the polarity inversion line, that appear as a flaring BP. During the maximum phase the jet spire usually migrates away from the flaring BP and both of them fade out as the reconnection ends (right panel).

In addition to jets that follow this standard behavior, non-standard jets have recently been studied by Moore et al. (2010), who showed that also these non-standard events are almost always characterized by some peculiar charateristics and dubbed them Blowout jets. The main observational peculiarity of blowout jets are: 1)the X-ray flaring of the whole base arcade in addition to the BP beside the base-arcade, 2) the blowout eruption of the core field that remains unperturbed during a standard event, 3) the extra jet strands rooted at different locations around the flaring BP, 4) cool material ejection together with the X-ray emitting plasma.

Fig.1.4 from Moore et al. (2010) shows a cartoon sequence that describes the blowout jet scenario. Many are the similarities with the standard sce-

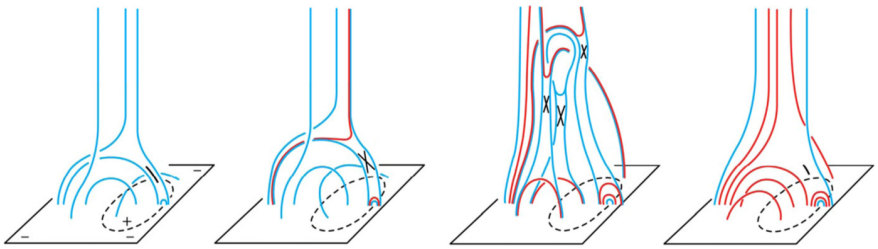

Figure 1.4 A cartoon sequence from Moore et al. (2010) showing the phases of the blowout model for X-ray jets. For notations see Fig.1.3.

nario. A magnetic arcade that is still emerging within an unipolar ambient field, but, opposite to the standard case, this emerging magnetic field is characterized by a strong shear. Such a twisted field carries a large amount of free energy that can cause an ejective eruption of the whole base arcade, hence the name blowout. In the leftmost frame the pre-jet situation is shown. As for the standard event, the emerging loops cause the formation of a current sheet at the interface between the emerging and the pre-existing field. But, differently from the standard model, the emerging closed magnetic field lines are extremely sheared. The second panel shows the onset of the jet, with reconnection occuring at the interface current sheet, just as for the standard event. X-ray emitting plasma fills both the open field lines that constitute the jet spire and the closed field lines that form the side BP. While the red lines do not differ from the standard model, a different dynamics characterizes the core field that will undergo the eruption. The reconnection occurring at the interface current sheet removes the external loops of the emerging arch. These outer fields help to prevent the twisted emerging loops from erupting. Once this external "pressure" is removed (third panel) reconnection occurs also in the arch core that becomes bright at X-wavelengths. The upward reconnected field lines that result from these second reconnection event form extra-strands of the jet spire, that are rooted near the adjacent BP. In the end phase, illustrated by the rightmost panel, the jet has assumed a curtain-like structure and quickly stops its X-ray emission because reconnection is no more undergoing.

Several authors have determined the temperature and density of the jet plasma, but their results do not completely agree. From *Yohkoh* SXT data, Shimojo & Shibata (2000) found temperature ranging from 3 to 8 $\times 10^6$ K. Culhane et al. (2007) on the basis of spectral images obtained from the

EUV imaging spectrometer (EIS) on board of the *Hinode* mission, found the jet emission plasma at a temperature range from 0.4 to 5 $\times 10^6$ K, while Nisticò et al. (2011), from the *STEREO* Extreme UltraViolet Imager (EUVI), obtained temperature from 0.8 to 1.3 $\times 10^6$ K. Madjarska (2011) performed a combined *SOHO*/SUMER, *Hinode*/XRT, EIS, and *STEREO* EUVI analysis, finding temperatures in the range between 0.5 to 2 MK for the outflowing plasma and as high as 12 MK for the plasma located at the jet footpoint. Concerning electron densities, the inferred values are more consistent with each others. Shimojo & Shibata (2000) found values of 0.7 - 4.0 $\times 10^9$ cm^{-3}, while Culhane et al. (2007) provide density values of 4×10^9 cm^{-3}. On the other hand the value given by Madjarska (2011) is higher by an order of magnitude than the other values.

In their analysis Culhane et al. (2007) reconstruct the jets' light curves in several coronal lines from different ions as observed with EIS, finding that lines associated with colder plasma showed a post-jet enhancement. On the basis of this result, together with the observational fact that the apparent outflow speeds were below the escape velocity, the authors suggest that the jet plasma does not manage to escape from the gravitational field of the Sun and thus it is observed falling down to the Sun at temperatures slightly lower than when ejected.

Whether or not (and if yes, how often) the jet plasma manages to escape from the Sun is still a controversial issue in the study of coronal jets. It is important to clarify this point in order to understand how and whether jets do contribute to solar wind.

Up to now no comparisons of physical parameters for the two kind of jets, standard vs blowout, have been performed. Understanding the difference between these two classes is important in order to assess how and if they contribute to the solar wind. Indeed, being their morphology quite different, it is crucial that whenever results are given, the type of the analysed jet is specified.

We thus propose a new work, in which we analyze two ejecta, which fully comply with either the standard or the blowout models for X-ray jets. We determine outflow speeds, temperatures and densities in order to investigate whether the two jet types present different physical parameters. Furthermore, we calculate both the axial and temporal profiles of these quantities. We use the measured values to make a crude evaluation of the energy involved in standard versus blowout event and, finally, we define some constraints on the magnetic field energy that is released and that fuels the jets.

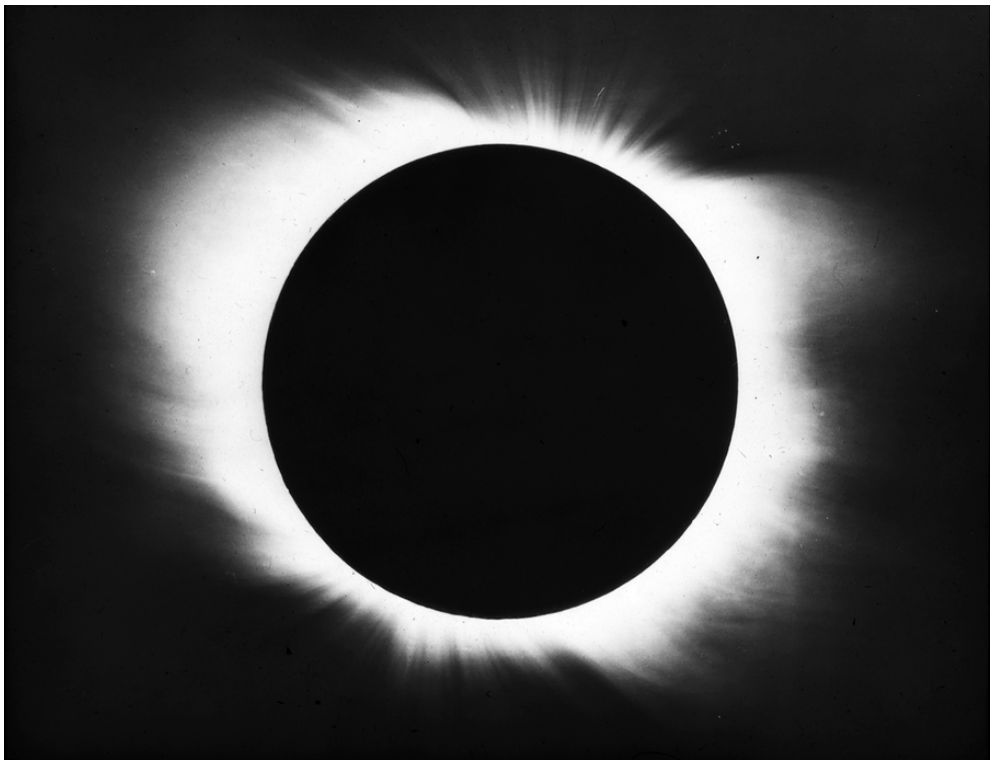

Figure 1.5 An amazing picture of the solar eclipse of 28th may 1900 taken from Barnard during an expedition of Yerken Observatory in North Carolina.

1.5 Polar plumes

Coronal plumes are another variety of transient phenomena that can be observed within polar region of the solar corona. These narrow structures that extend from the chromosphere into high corona and are rooted in CHs, can be observed both in visible and UV wavelengths. Because of their visibility in "white light", plumes, previously called polar rays, have been observed since the beginning of the 20th century, i.e. since the first images of the corona were taken.

Fig.1.5 shows a wonderful image of the solar corona, taken during the eclipse of 28th may 1900 by an expedition of the Yerken Observatory in North Carolina. After fifty years van de Hulst (1950) used this observation to carry out the first systematic analysis of polar plumes, finding that plumes exceed the background emission by a twenty per cent, and deriving a five times higher electron density of plumes compared with the background. Furthermore the question about the hydrostatic equilibrium of plasma within plumes

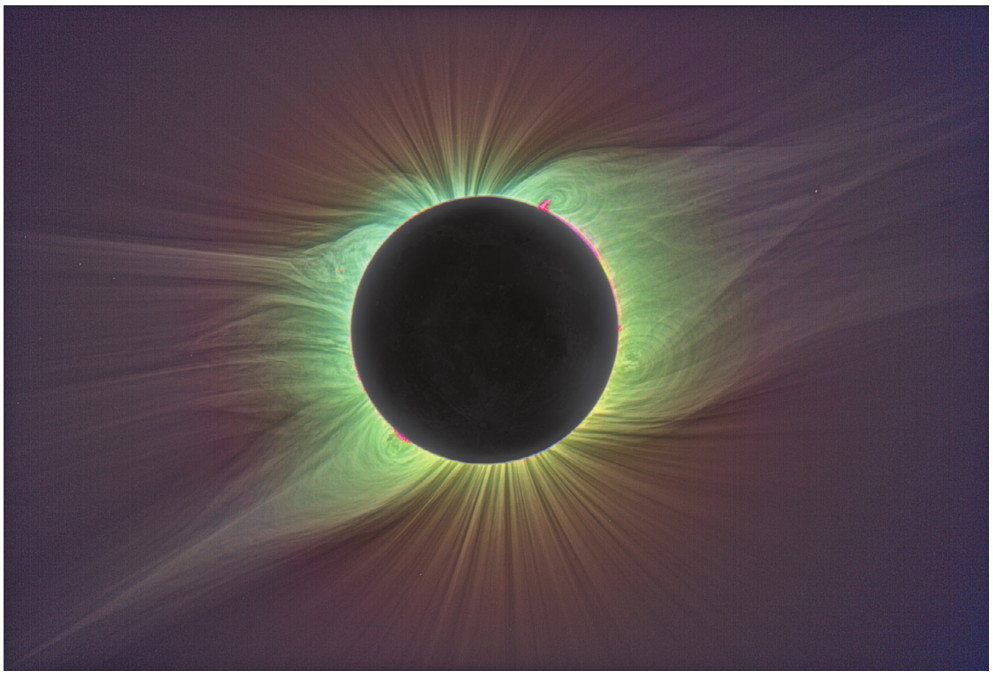

Figure 1.6 A color enhanced image of the visible light corona as observed during the 1 august 2008 solar eclipse (Pasachoff et al., 2009).

was raised by the authors, who suggest that plumes are made of plasma in hydrostatic equilibrium, like its surrounding, that is forced in this peculiar ray-like shape by the line of force of the general magnetic field of the Sun.

Fig.1.6 shows another spectacular image of the solar corona oberved during the eclipse of 1 august 2008 (from Pasachoff et al., 2009). Polar plumes dominate the scenario around poles and are clearly distinguishable even at heliocentric distances larger than a solar radius. By comparing this kind of plume observations with simultaneous space-borne images of the UV corona it has been definitely confirmed that polar plumes are strictly rooted in Polar CHs.

Since polar CHs develop best during minimum in the solar activity many dedicated plumes studies have been performed during the last two minimum of the 11 years solar cycle, i.e. in 1997-1998 and 2008-2009 (see for a review Wilhelm et al., 2011). Anyway, there is still a lack of agreement about a model that can explain the formation of plumes and even many observational facts result to be in contrast with each other (Wilhelm et al., 2011).

Plumes are obviously 3D structures but it is not possible to determine their 3D configuration from 2D observations, in which the plume emission

appears as integrated along the line of sight. Furthermore, not all plumes might be of cylindrical shape and it has been proposed that some plumes, dubbed "curtain" plumes, become visible only when the curtain is aligned along the line of sight (Gabriel et al., 2003). These authors based their conclusion on the impression that most of the plumes appear as rooted in the far side of the CH. Since there is no reason to justify such an asymmetry, the effect is thought to be caused by the increase in the line of sight that is obtained when the curtain is oriented perpendicularly to plane of the sky. On the other hand there is no doubt that many of the observed plumes associated with BPs do show a cylindrical shape. These second type of plumes are referred as "beam plumes".

In order to characterize polar plumes and the surrounding regions, called Inter Plume Regions (IPRs), many observational fact have been collected, both from ground-based and space-borne instruments. The ground-based observations present the advantage given by the possibility to use large telescope and thus permitting high spatial and temporal resolution. On the other hand, because of the atmospheric absorption, plumes can only be studied from Earth within the restricted window of the visible wavelengths, that, as we have seen, represents only a small portion of the entire spectrum of the coronal emission. Furthermore, with the exception of high altitude white light coronographs such as MkIV K-coronameter of the Mauna Loa solar observatory (DeForest et al., 2001) plumes studies can be performed only during solar eclipse.

Space instruments present size and mass restrictions (hence limits to the resolution) but are able to deliver both continuous and wide-spectrum observation. Furthermore space instruments permit in-situ analysis of plumes or at least the research of plumes remnants in the solar wind. Indeed, the Ulysses spacecraft found variations in the plasma velocity profile that could represent the signature of polar plumes into the SW Reisenfeld et al. (1999).

van de Hulst (1950) with their work confirmed Alfvén theories that plumes shape correspond with open magnetic field line and they outline the global magnetic field of the Sun.

Many electron density measurements have shown that the plasma in a CH is characterized by two clearly different density regimes, associated respectively with plumes and IPRs. Wilhelm (2006) has shown that within a CH plumes occupy at maximum 10% of the whole CH.

Plumes show brightness variations in timescale of less than 10 minutes while on the other hand the general shape of the plume appears to remain unchanged for interval ranging from hours to days.

It is difficult to answer the question of how long is the life of a plume because of the difficulty in separate plumes from IPR over long time intervals.

Such long term observations were not available before the launch of SDO and this lack constitute one of the motivation of our work.

In the study of polar plumes a crucial point is understanding the importance of wave phenomena, that could help in the generation of the plume itself. Wave could be an efficient mechanism to transport energy from the solar surface up to the corona. In order to detect wave signature, periodic brightness variations have been studied in plumes by Deforest et al. (1997) who found wave trains propagating in plumes at speed of 75 - 150 km s^{-1} and periods between 10 and 15 minutes. Anyway, other authors (see f.e. McIntosh et al., 2010; Tian et al., 2011) claim that these quasi periodic oscillations are caused by high velocity outflows.

Understanding whether this brightness oscillations are due to wave or outflow is fundamental in order to get a clear comprehension of formation and fueling mechanism that control plume evolution. Clarify this point is also important in order to understand the role of plume and IPR in the formation and contribution to the mass budget of the solar wind.

Chapter 2

Instrumentation

The work described in this thesis has been carried out on the basis of data acquired by several instruments on board of three space missions: the *Hinode*, the *Solar TErrestrial RElations Observatory* (*STEREO*) and the *Solar Dynamics Observatory* (SDO) missions. In this chapter we will briefly describe each mission and review the main characteristics of the instruments that have been used to collect the data analyzed in this work.

2.1 The *Hinode* mission

Hinode (sunrise in Japanese) is a Japanese mission of the Japan Aerospace Exploration Agency's Institute of Space and Astronautical Science (ISAS JAXA) (Kosugi et al., 2007), with the collaboration of the National Aeronautics and Space Administration (NASA), the European Space Agency (ESA), the Science and Technology Facilities Council (STFC, United Kingdom) and the Norwegian Space Centre (NSC). Formerly named Solar-B, *Hinode* is the follow-up of the *Yohkoh* mission (Solar-A) and was launched on 22 september 2006 with a JAXA M-V rocket.

The *Hinode* mission aims at understanding how magnetic energy is transferred from the photosphere to the upper layers of the solar atmosphere and how this energy can produce explosive phenomena. In details, the scientific goals of the mission are (Kosugi et al., 2007):

1. To understand the processes of magnetic field generation and transport including the magnetic modulation of the Sun's luminosity.

2. To investigate the processes responsible for energy transfer from the photosphere to the corona and for the heating and structuring of the chromosphere and the corona.

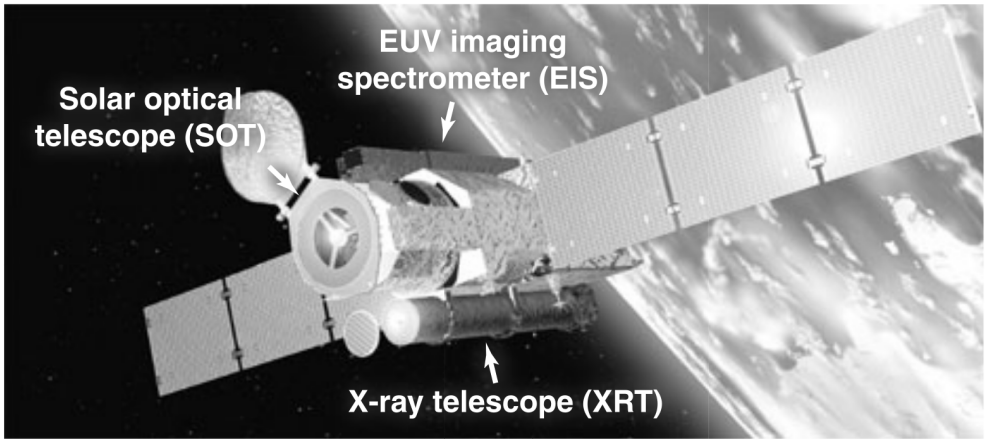

Figure 2.1 The *Hinode* spacecraft with its payload: the Solar Optical Telescope (SOT), the EUV Imaging Spectrometer (EIS), and the X-Ray Telescope (XRT). From Narukage et al. (2011).

3. To determine the mechanisms responsible for eruptive phenomena, such as flares and coronal mass ejections, and understand these phenomena in the context of the space weather of the Sun - Earth System.

The science questions that *Hinode* aims to answer are based on the scientific knowledge gained by the *Yohkoh* mission which showed that the corona is an highly dynamic and structured environment where rapid phenomena like mass acceleration and heating are ordinary events. The *Yohkoh* observations at the time of a high solar maximum provided evidences that support the hypothesis of magnetic reconnection being the main actor in energy release processes during explosive phenomena like flares. The *Hinode* mission is designed to further operate along this direction and account for solar variability in terms of the interaction between magnetic field and plasma. Hence the observational characteristics of the mission and of its instruments have been designed focussing on describing the magnetic field.

The payload of the *Hinode* satellite is composed by the Solar Optical Telescope (SOT) that is able to measure the photospheric magnetic field producing magnetograms, dopplergrams and vector magnetographs, the EUV Imaging Spectrometer (EIS) and the X-Ray Telescope (XRT) which measure how the solar atmosphere react to magnetic field changes. All these instruments may collaborate analyzing a same feature (located where the spacecraft is pointed), at different heights in the solar atmosphere. In our work we have used data acquired from XRT.

The *Hinode* spacecraft after the launch and approaching phase reached a

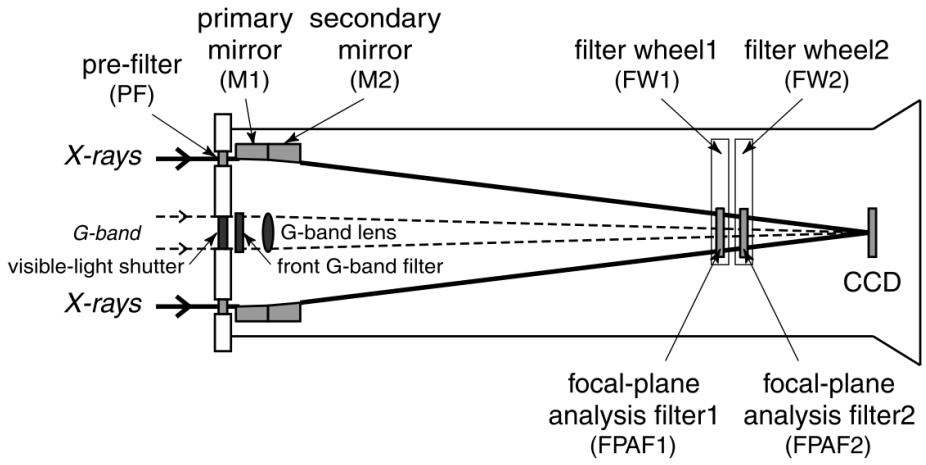

Figure 2.2 The configuration of XRT and its optical elements. The solid line represents the optical path of X-rays (from Narukage et al., 2011)
.

circular polar Sun-synchronous orbit around the Earth at an altitude of 680 km, an inclination of 98.1 degree and a period of 98 minutes. This orbit allows *Hinode* to observe the Sun continuously over a time-interval of 9 months per year. The scientific data collected by the satellite are downloaded through 15 daily contacts between the spacecraft and a high latitude (78°) ground station located in the Svalbard islands (Norway). The amount of data that are downloaded per day is approximately 40 Gbits. These scientific data are then transmitted to ISAS where they are combined with spacecraft data received at the command ground station in Japan and the finally reformatted FITS file (level0) are made available to the scientific community.

2.1.1 The X-ray Telescope

The XRT provides an unprecedented combination of high spatial and temporal resolution surpassing all previous X-ray solar telescopes (Golub et al., 2007).

It is a grazing incidence telescope with a Wolter I design. Fig. 2.2 from Narukage et al. (2011) shows the structure and the optical elements of XRT. The X-ray path is shown by the solid line while the dashed line depicts the optical path of the visible light (G-band), that is used to co-align the instrument with the SOT. The main elements that constitute the telescope

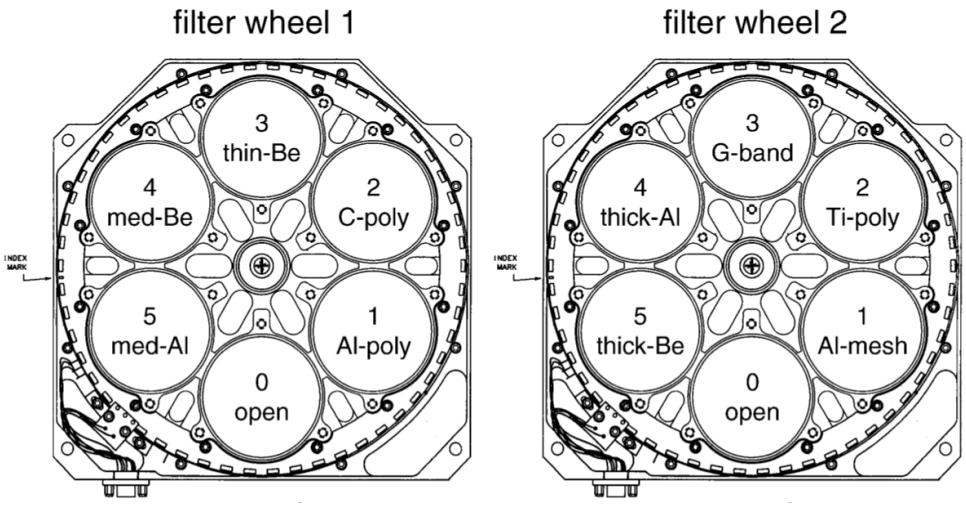

Figure 2.3 The Focal Plane Filter Wheels of XRT. XRT has two filter wheels and each wheel has 6 position and hosts 5 analysis filter (from Narukage et al., 2011).

are the pre-filter, the primary and secondary mirrors, two focal plane filter wheels and the CCD.

The pre-filter is made of 8 annular filter segments of aluminum on a polyimide film that acts as entrance aperture for the incoming X-rays.

The mirrors are grazing-incidence annular mirrors, made of Zerodur, corresponding to a total geometric aperture are of 2.28 cm^2.

Each of the two focal plane filter wheels has 6 positions that host the filters as shown in Fig. 2.3. The first filter wheel has 5 X-ray different filters (called Al-poly, C-poly, thin-Be, med-Be and med-Al) and an open position, while the second wheel hosts 4 X-ray filters (Al-mesh, Ti-poly, thick-Al and thick-Be) and a visible-light filter (G-Band) plus the open position. The nine X-ray filters are characterized by different metals and supports, with varying thickness.

These filters are designed to image the corona in the temperature range of 1 - 10 $\times 10^6$ K. Indeed, the most important scientific of XRT is the temperature diagnostic via the filter-ratio technique (see Sec. 3.4.2). Narukage et al. (2011) give a detailed analysis about how this diagnostic technique can be applied to XRT data: the high number of available filters provides the possibility to choose the filter pair that better probes the observed plasma. In particular, in our work we used XRT data acquired in the Al-mesh, Al-poly, C-poly and Ti-poly filters that are most sensitive to plasma at $\approx 1 \times 10^6$ K,

as shown in Fig. 2.4.

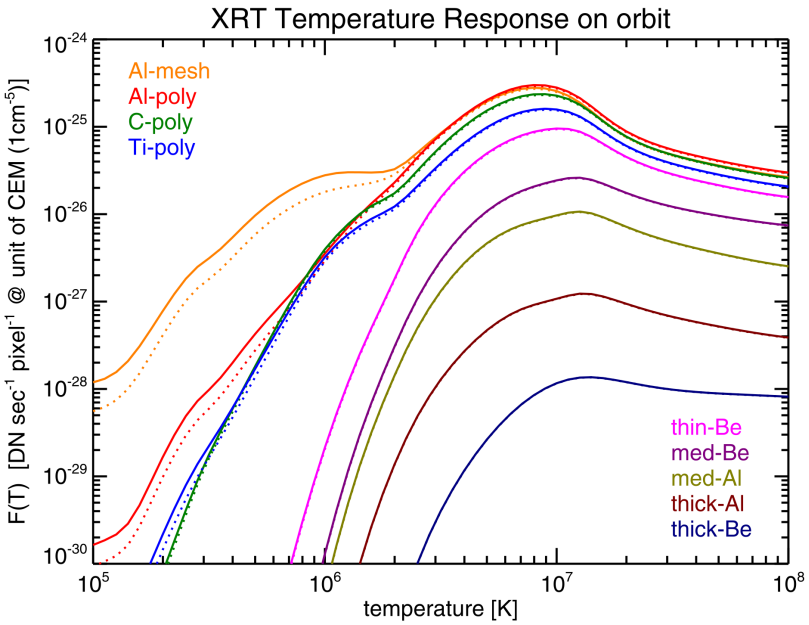

Figure 2.4 The response function of different XRT filters to coronal temperatures. The filter adopted in this work are the four filters that are most sensible to lower temperatures, whose name is given in the upper left corner (from Narukage et al., 2011)

A few months after the first light of XRT (on 23 october 2006) the *Hinode* scientists realized that the observed X-ray intensities started decreasing. This intensity decrease was observed in all filters, the thinner filters (used in our work) being more affected. For example the Quiet Sun intensity observed with the Al-mesh filter decayed from the initial value of 10 DN s^{-1} $pixel^{-1}$ to almost 3 DN s^{-1} $pixel^{-1}$. Narukage et al. (2011) concluded that this decreases was caused by the accumulation of some contaminants along the optical path of the XRT. Since this contamination did not affect all filters in the same way the ratio between different filters was changed with respect to the calibration value and kept varying with time because of the continuously growing thickness of the contaminants. Hence, the temperature diagnostic capability of XRT was altered. Luckily, by means of regular bake-out of the CCD, the contaminants thickness was kept to an almost constant value. Furthermore, by undertaking a systematic calibration process, Narukage et al. (2011) were able to determine the thickness and composition of contaminants and thus

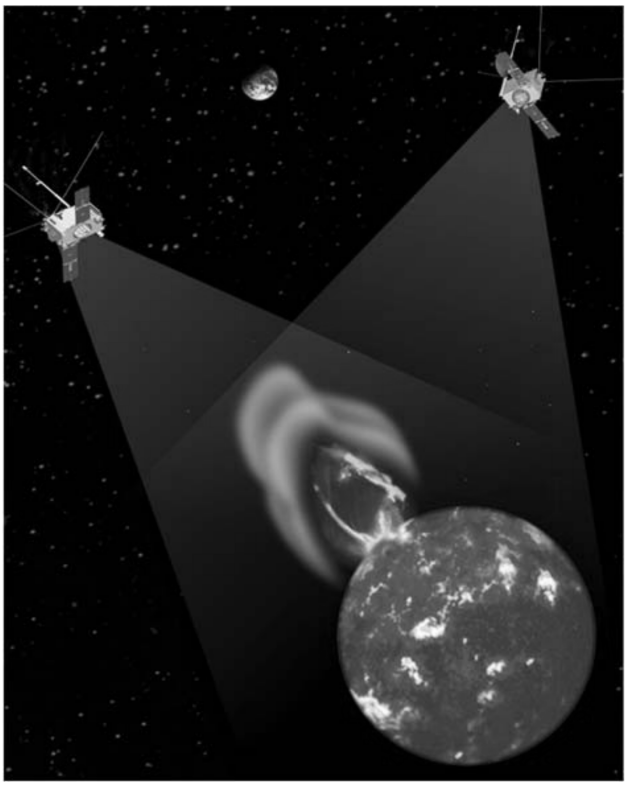

Figure 2.5 Artist view of the *STEREO* mission. The two spacecraft observe the Sun from two positions each side of the Earth-Sun line (Kaiser et al., 2008).

recalculate the temperature response function for all filters as a function of time, restoring the temperature-diagnostic capability of XRT.

2.2 The *STEREO* mission

The *Solar Terrestrial Relations Observatory* (*STEREO*) is a NASA mission composed of two nearly identical spacecraft orbiting the Sun at two different heliocentric distances that provide stereoscopic measurements of the Sun and of the Sun-Earth connecting environment. The *STEREO* mission was launched from Kennedy Space Center (USA) on 26 October 2006 and had its first light on December 2006.

As we have seen the solar magnetic activity is characterized by an intense variability. Among all the phenomena that are caused or linked to such activity, extremely energetic solar storms and the associated Coronal

Mass Ejections (CME) are probably the most Earth-involving events, because the ejected high speed, high temperature plasma can reach the Earth and deeply influence its magnetic environment. Such impacting CMEs cause large scale geomagnetic storms, and, beside the beautiful aurorae, such disturbances can disrupt telecommunications, damage electrical transmission lines and cause long-lasting blackouts. Furthermore, outside the protection shield of the Earth atmosphere, both satellites and manned space-activities are extremely sensitive to the harmful radiation storms that accompany major CMEs. Despite all the solar missions that have been observing the Sun over the last decades, the actual capability of prediction and observation of the birth and propagation of CMEs is still rather poor. The difficulty in forecasting the characteristics of the space environment around the Earth (the so called space weather) arises, at least partially, from all of the available observations being acquired from a single vantage point, i.e. along the line Earth-Sun. In this scenario, the *STEREO* mission has been designed to provide for the first time images of both the Sun and Earth-Sun connection environment from new perspectives. Having two spacecraft that operate simultaneously from two different position separated by a wide and varying angle (see Fig.2.5) allow the solar scientists to follow the evolution of CMEs as they propagate along the path between the Sun and our planet.

The main scientific goal of the *STEREO* mission is the study of CMEs, to understand and explain how these energetic solar eruptions affect the interplanetary and terrestrial environments and cause disturbances and geomagnetic storms on our planet. Specifically the science objectives are (Kaiser et al., 2008):

- Understand the causes and mechanisms of CMEs initiation.
- Characterize the propagation of CMEs through the heliosphere.
- Discover the mechanisms and sites of solar energetic particle acceleration in the low corona and the interplanetary medium.
- Develop a three-dimensional, time-dependent model of the magnetic topology, temperature, density and velocity structure of the ambient solar wind.

The orbit of the two nearly identical spacecraft have been designed such that one of the two spacecraft, called "Ahead" precedes the Earth in its revolution path around the Sun while the other spacecraft, dubbed "Behind", follows the Earth. The drift rate, that is the variation in the separation angle between the spacecraft and the Earth, is $\approx \pm 22^\circ$ per year.

The two observatories, that were launched aboard a single rocket, have been placed in such different orbits via "lunar swingbys", a method in which the gravity of the Moon is used to redirect each spacecraft to its appropriate orbit. In a first three-month-lasting phase both spacecraft were following a highly eccentric orbit extending from very close to Earth to behind the Moon. After two months one of the spacecraft approached the moon close enough to take advantage of the lunar gravitational pull and being redirected into an heliocentrical orbit behind the Earth (mean distance from the Sun ≈ 1.06 AU). After one more month the other spacecraft was sent by another lunar swingbys to an orbit ahead of the Earth, at an heliocentric distance of ≈ 0.96 AU.

Because of the different scientific targets that can be observed at different separation angle, the mission has been divided in four phases. During Phase 1 ($\approx$ 1 year) the spacecraft are less then 50° apart and the configuration is optimal for taking stereoscopic image pairs of the corona that can be used to construct the first 3D images of our star. In Phase 2 the spacecraft reaches the quadrature configuration and can image directly in the plane of the sky all the phenomena like CMEs that are going to reach the Earth. Phase 3 and 4 are part of the extended mission when the spacecraft will have a complete view of the Sun allowing an hopefully high increase in the ability of predicting changes in solar activity and space weather conditions.

Each of the two twin observatories has an instrument payload made of four different packages, as shown in Fig.2.6:

- the Sun Earth Connection Coronal and Heliospheric Investigation package (SECCHI), a suite of remote sensing instruments, containing an Extreme UltraViolet Imager (EUVI), an inner and an outer white-light coronograph (COR1 and COR2) and two white-light Heliospheric Imagers (HI) (Howard et al., 2008),

- the In-situ Measurements of PArticles and CME Transients (IMPACT), a package of in-situ instruments that measure magnetic fields, solar wind electrons and energetic electrons and ions,

- the PLAsma and SupraThermal Ion Composition (PLASTIC) that measure mass and charge state composition of heavy ions via in-situ measurements

- the *STEREO*/WAVES, a radio-burst tracker that measures radio disturbances with a set of 3 orthogonal monopole antennas of 6 meter each.

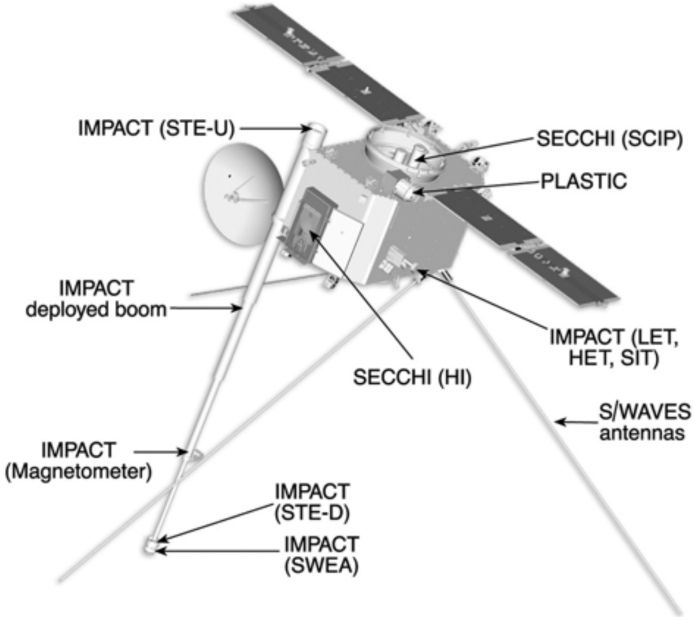

Figure 2.6 A representation of one of the two spacecraft of the *STEREO* mission, where the location of the different packages is shown. All the SECCHI instruments points at the Sun, with the exception of the Heliospheric Imagers that is oriented perpendicularly to the other remote sensing instruments.

In our work we have used images taken by the EUVI and COR1 instruments from both the *STEREO* Ahead and Behind spacecraft. Since both instruments take regularly cadenced full-disk images, it has been possible to detect in *STEREO* images the small-scale CH events that we observed in *Hinode* XRT data. Such *STEREO* images show the events from two different points of view and allowed us to locate the observed events on the solar disk and to reconstruct their 3D configuration.

2.2.1 The Extreme UltraViolet Imager

Among the 5 telescopes that compose the SECCHI suite and observe the entire inner heliosphere, i.e. from the solar disk out to the Earth, the Extreme UltraViolet Imager (EUVI, Wuelser et al., 2004) has the role of observing directly the solar disk.

The EUVI, developed at Lockheed Martin Solar and Astrophysics Laboratory (LMSAL, USA), is a normal incident Ritchey-Chretien telescope, with

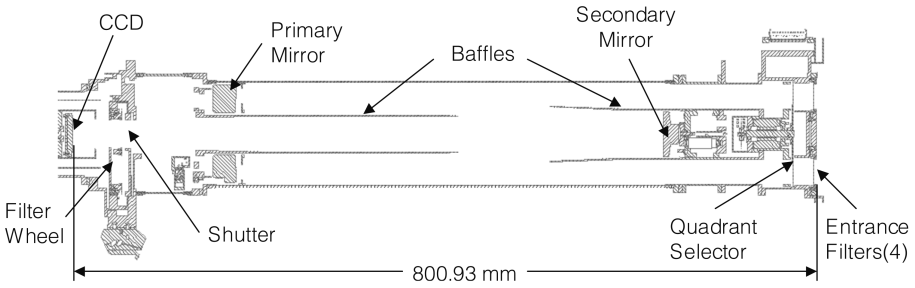

Figure 2.7 The cross section of the EUVI instrument, showing the different components. From Wuelser et al. (2004).

an effective focal length of 1.75 m, designed to observe the transition region and corona in four different EUV emission lines, at respectively 171 Å (Fe IX), 195 Å (Fe XII), 284 Å (Fe XV) and 304 Å (He II).

The EUV radiation coming from the solar corona enters the telescope through thin aluminum filters located at the entrance aperture that suppress the incoming visible, infrared (IR) and UV light, shielding the telescope from the solar heat. As shown in Fig. 2.7 from Wuelser et al. (2004), the quadrant selector located just behind the entrance aperture sends the incoming radiation to one of the four quadrants in which both the primary and secondary mirrors are divided. Each of these mirror sectors is characterized by a different narrow passband multilayer coating that is optimized for one of the 4 EUV channels. The residual IR and visible radiation is removed from the incoming beam by means of a second series of metal filters located on a filter wheel near the focal plane. Finally, after passing a rotating blade shutter the image is formed on a 2048 x 2048 backside illuminated CCD.

The pre-flight calibrations for the individual components, i.e. the mirrors, the CCD, the entrance and focal plane filters have been combined together to plot the effective areas as a function of wavelengths for the different channels, as shown in Fig. 2.8.

By combining the effective areas of the instrument with the coronal lines emissivities given as a function of temperature (obtained via the CHIANTI software, Young et al., 2003), with a standard assumed coronal composition (coronal abundances from Feldman, 1992) and with the ionization equilibrium of Mazzotta et al. (1998), we can calculate the temperature response functions for the different EUVI channels. As shown in Fig. 2.9 the temperature response functions are measured in photon s^{-1} for a column emission measure of 10^{44} cm^{-3} (from Aschwanden et al., 2008). For a detailed analysis

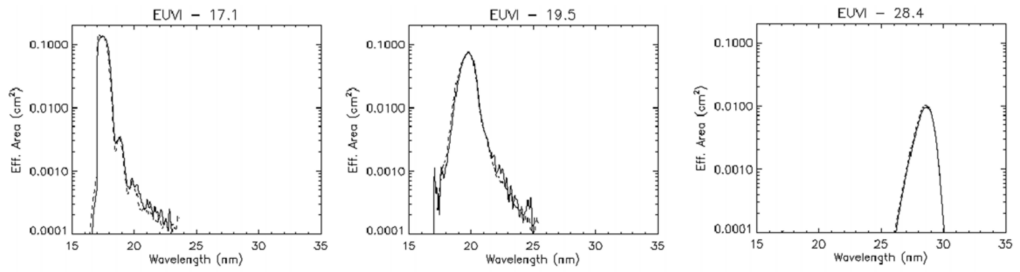

Figure 2.8 The effective areas plotted as a function of wavelength for the EUVI channels 171, 193 and 284 Å. The solid line shows the areas for the Ahead and the dashed line for the Behind spacecraft. Adapted from Howard et al. (2008)

of these physical quantities and the adopted assumptions see Sec.3.4.2.

2.2.2 The inner coronograph

In addition to EUVI data in our work we also used a few images obtained by the inner coronograph of *STEREO*, of which we give here a concise description. The inner coronograph (COR1) is a Lyot internal occulted refractive coronograph, with a field of view that goes from 1.4 to 4 solar radii (Howard et al., 2008) and is designed to measure the weak visible light emitted from the corona by scattering light from the much brighter photosphere.

Opposite to LASCO C1 (Brueckner et al., 1995), the inner coronograph of the *SOHO* mission, COR1 is a refractive telescope and it is the first coronograph of such kind on a space mission. The internally occulted design allows a spatial resolution, close to the solar limb, higher than with externally occulted coronograph.

A polarizer located between the telescope lens allows the reconstruction of the polarized brightness that helps removing the scattered light from the photosphere that, contrary to the visible light emitted from the corona, is in general unpolarized.

2.3 The SDO mission

The *Solar Dynamics Observatory* (SDO, Pesnell et al., 2012), the first NASA mission of the space-weather program "Living with a star", was launched on 11 February 2010 with an ATLAS V 401 launch vehicle from Kennedy Space Center (USA) and on 1 May 2010 returned the first scientific data.

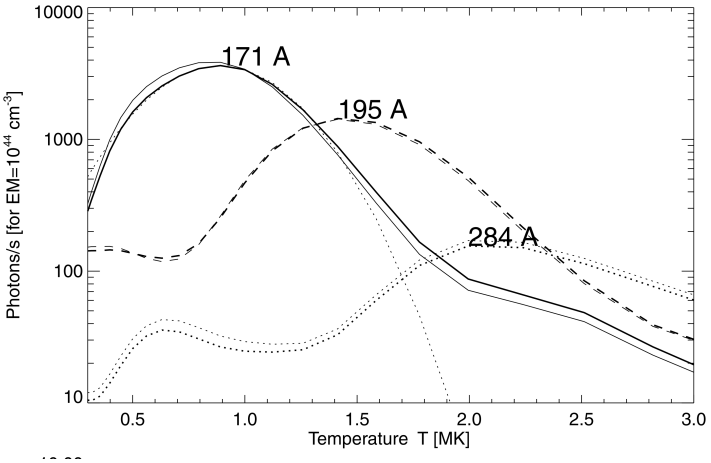

Figure 2.9 The temperature response functions for the EUVI channels 171 Å (solid lines), 193 Å (dashed lines) and 284 Å (dotted lines). The response functions for EUVI Ahead and Behind are shown respectively with thick and thin curves. From Aschwanden et al. (2008).

The main goal of the "Living with a star" program is to increase the understanding of how heliospheric phenomena affect life and society, with the ultimate target of create a predicting capability that will allow scientists to forecast the conditions of the Sun and of the near-Earth space environment. Understanding the cause of the "space weather" effects, like satellite damages, telecommunications interruptions, power grid failure and global positioning system disruptions, is a fundamental step towards building a technologically based society.

Within this program the SDO mission is designed to provide high quality data with the best available space and time resolution. Such high resolution images will allow the identification of the precursors of high energetic events like flares and CMEs that strongly influence the heliosphere. The SDO data will help aslo reconstructing the magnetic field topology: this step is necessary to recognize the typical features where reconnection events, characterized by an high amount of energy release, occur. The SDO mission will act as a monitor of the global solar magnetic field, from the interior to the outer layer of the solar atmosphere. Indeed, a deep understanding of how magnetic field are created, amplified and ejected from the Sun is needed to forecast the emergence and evolution of active regions. In order to do so the SDO will observe the Sun during the activity maximum of the 24th Solar Cycle, begun at the end of 2008.

One of the main objects of the SDO observations is the variability of the EUV radiation emitted from the Sun. These high energetic photons are the main agents for both the radiative cooling of the solar atmosphere and for the heating of the upper layer of the Earth atmosphere. The EUV energy flux can vary abruptly by 2-3 order of magnitudes within few seconds. Such a rapid increase of the energy flow can heat the outer Earth atmosphere and modify the drag on satellites and create an ion layer that disturbs telecommunications and global positioning systems.

In details, the SDO mission aims at improving our understanding of the following science questions (Pesnell et al., 2012):

- What mechanisms drive the quasi-periodic 11-year cycle of solar activity?
- How is the active region magnetic flux synthesized, concentrated, and dispersed across the solar surface?
- How does magnetic reconnection on small scales reorganize the large-scale field topology and current systems, and how significant is it for the heating of the corona and the acceleration of the solar wind?
- Where do the observed variations in the Sun's extreme ultraviolet spectral irradiance arise, and how do they relate to the magnetic-activity cycles?
- What magnetic-field configurations lead to the coronal mass ejections, filament eruptions, and flares that produce energetic particles and radiation?
- Can the structure and dynamics of the solar wind near Earth be determined from the magnetic-field configuration and atmospheric structure near the solar surface?
- When will explosive phenomena occur, and is it possible to make accurate and reliable forecasts of space weather and Earth's climate?

The SDO mission is equipped with three remote-sensing packages:

- the Atmospheric Imaging Assembly (AIA, Lemen et al., 2012) is a package composed of 4 similar telescopes that observe the solar atmosphere in 10 different wavelength bands, as explained in details in Sec.2.3.1.
- the Extreme-ultraviolet Variability Experiment (EVE, Woods et al., 2012) measures the spectral irradiance of the Sun in the EUV, from

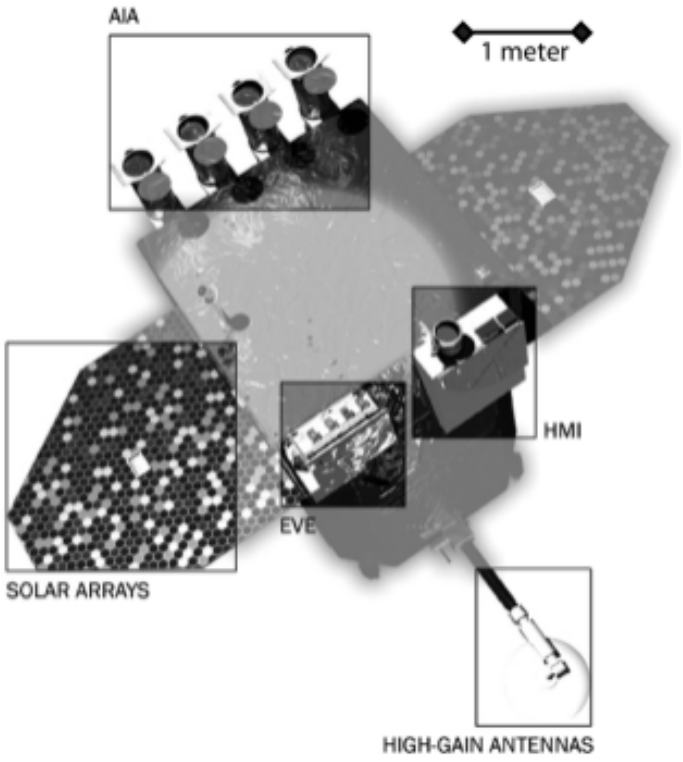

Figure 2.10 The Solar Dynamics Observatory spacecraft: the payload instruments, the solar arrays and the high-gain antennas have been highlighted to facilitate their identification.

1 to 1050 Å and at 1216 Å, thus monitoring continuously the EUV emission with a cadence of 10 seconds.

- the Helioseismic and Magnetic Imager (HMI, Schou et al., 2012) through full-disk measurements of the Doppler and Zeeman effects on the Fe I 6173 Å line is able to provide both velocity and magnetic field maps over the entire solar disk with high cadence.

Fig. 2.10 shows the SDO spacecraft, with boxes that highlight the different components of the satellite, i.e. the instruments (AIA, EVE and HMI) plus the solar arrays and the high-gain antennas.

The science requirements of uninterrupted high cadence and high resolution images led to an huge amount of daily produced science data. Every day the SDO instruments assembly acquire 150000 full-Sun images plus 9000 EUV spectra, that correspond to 1.5 terabyte of data. Hence, the need for a

continuous downlink of data led to the choice of an inclined geosynchronous orbit that allows an uninterrupted contact with a single dedicated ground station, located in New Mexico. On the other hand, SDO could not be placed in a Sun-synchronous low Earth orbit because of the need of data storage between contacts with ground stations: data-recorder, with such a high storage capability, to be used in space applications still do not exist. The selected inclined geo-synchronous orbit, however, implies higher launch cost because of the high final orbit altitude (35800 km), and two eclipse "seasons", each lasting tre weeks, over which the Sun is obscured by the Earth. The SDO mission has a nominal duration of 5 years, after which the spacecraft will be moved outside the geosynchronous belt to a disposal orbit.

In our work we have used data from the AIA package, described in the next session, to study polar plumes, best visible when originate in polar CHs during the minima of solar cycle. SDO is a mission designed to observe the Sun during the maximum phase, but, since the solar minimum of 2008-2009 was unexpectedly deep, minimum features as polar CHs were also visible in the first months of SDO data (2010).

2.3.1 The Atmospheric Imaging Assembly

The AIA package is a suite composed of 4 Cassegrain telescopes that observe continuously the solar corona and transition region producing 0.6 arcsec per pixel, full-disk, 12 seconds cadence images in 10 different channels: 7 EUV narrow bands (94, 131, 171, 193, 211, 304 and 335 Å), 2 UV band (centered at 1600 and 1700 Å) and a visible light channel.

The main science goal of AIA is understanding the processes determining the development of the magnetic environment in the solar atmosphere, with focus on the interaction between the local magnetic field and the ambient plasma. Such science target requires observations of the multi-temperature corona at as high as possible space and time resolution. This has been implemented by a package of four different telescopes imaging the Sun continuously and simultaneously in several channels corresponding to different plasma temperatures.

Fig. 2.11 gives the cross section of one of the four Cassegrain telescopes of the AIA suite, and shows the main components of the instruments, that are:

- The aperture door that protects the telescope during launch
- An entrance filter and a focal-plane filter-wheel that suppress unwanted infrared, visible and UV radiation. The selection of the desired passband in telescopes 1 and 4 is obtained by means of the filter wheels,

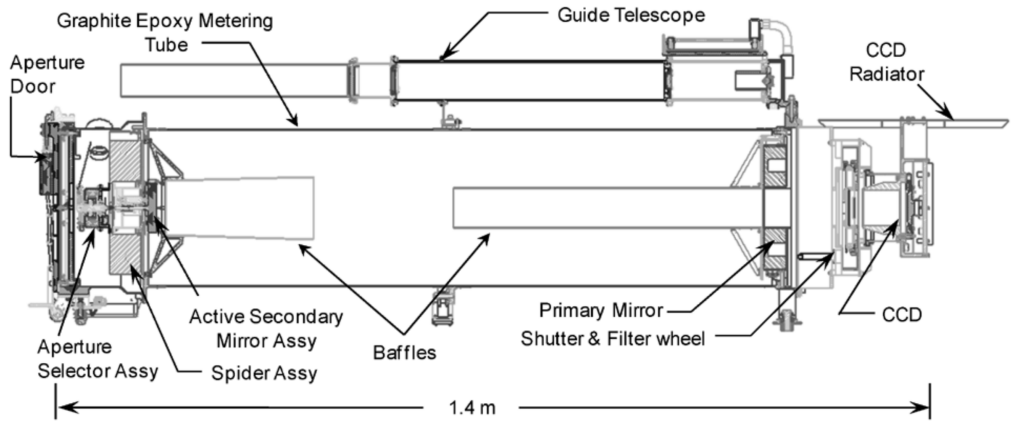

Figure 2.11 One of the four telescopes of the AIA package with its own guide telescope (from Lemen et al., 2012).

where aluminum is adopted for 171 Å and longer wavelengths, while zirconium is used to select shorter wavelengths.

- The aperture selector that is used to expose only half of the aperture at any time. Since telescope 2 is the only one that observes in two passbands that are associated with the same aluminum filter (i.e. 193 Å and 211 Å, see Fig. 2.12), only this telescope requires a mechanical aperture selector.

- The primary (20 cm diameter) and secondary mirrors, that are normal incidence mirrors made of Zerodur and divided in two sectors, each with a different multilayer coating designed to provide a narrow wavelength band response. The secondary mirror, by means of active optics, is pointed in response to signals from the guide telescope, mounted above each telescope tube.

- a back-thinned CCD camera located at the focal plane, with 4096 4096 pixels, each pixel corresponding to 0.6 arcsec

- buffles that prevents charged particle from reaching the CCD

- a mechanical shutter that regulates the exposure time

Fig. 2.12 gives the arrangement of the four AIA telescopes as viewed from the Sun, showing each telescope with the corresponding wavelength passbands. Of the 7 EUV channels, 6 are centered on specific iron ion lines

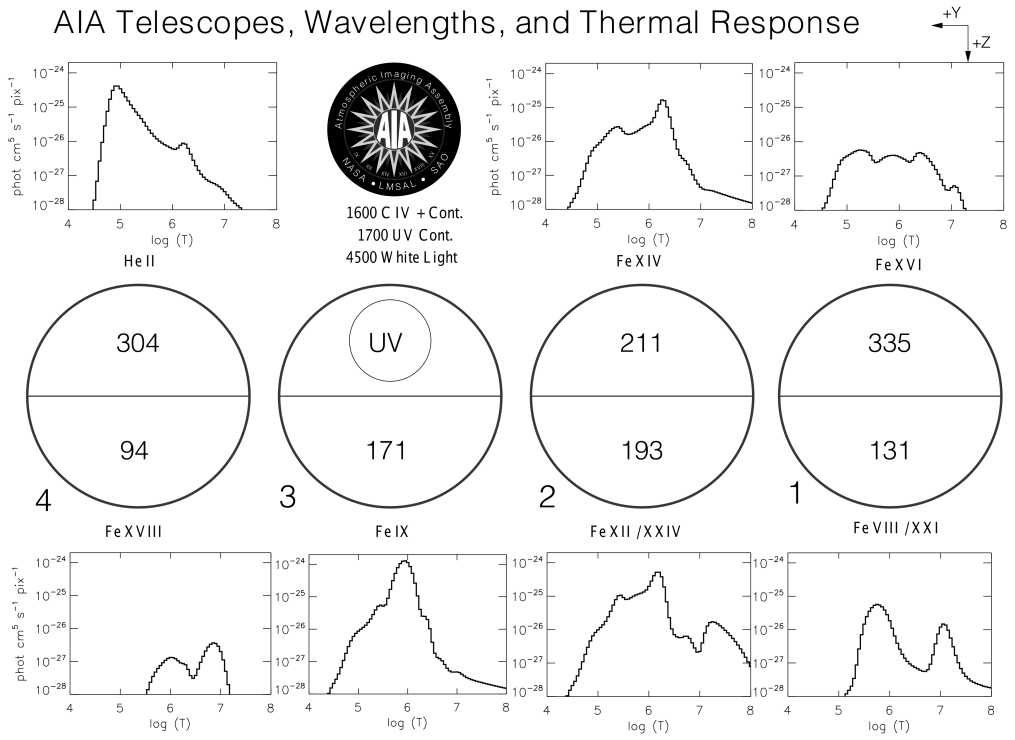

Figure 2.12 The arrangement of the four telescope of AIA as seen from the Sun. Each telescope is depicted with the corresponding passbands and the associated filter response for each channel. Source: *AIA Analysis users guide*, www.lmsal.com/sdodocs/public_docs/sdo_analysis_guide.html

(94 Å - FeXVIII, 131 Å - FeVIII and FeXXI, 171 Å - FeIX, 193 Å FeXII and FeXXIV, 211 Å - FeXIV, 335 Å - Fe XVI) covering a wide spectrum of coronal temperatures, from 4×10^5 K of FeVI to 2×10^7 K of FeXXIV. The 304 Å channel, centered on the HeII Lyman alpha line, images chromosphere and transition region plasma at 5×10^4 K. Furthermore, telescope 3 images the Sun also in 2 UV channels, centered respectively at 1600 Å (CIV line) and 1700 Å (continuum) and a visible light channel (4500 Å). Every filter is characterized by a wavelength response that gives the effective area as a function of wavelength. By combining this response with the coronal lines emissivities, abundances and ionization equilibrium data we obtain the temperature response function of each filter as shown in the upper and lower panels of Fig. 2.12.

The AIA data, once compressed onboard, are immediately transmitted to the dedicated ground station in New Mexico, where they are transferred

as Level0 images to a permanent archive at the Joint SDO Operation Center (JSOC) located at the Stanford University (USA). Data at JSOC are processed through a pipeline that involves several calibration steps like subtracting dark images, applying flat field corrections, removing "bad" pixels, "de-spiking" for energetic particles and rotating to put solar North at the top of the image. Finally metadata like roll-angle, camera gain and effective areas are updated to form, together with the image data, a Level 1 FITS files. In order to take advantage of high cadence, multiple wavelength channels characteristics of AIA data, it is important to be able to display different telescopes images as multi-wavelength movies. This requires a further calibration, from Level 1 to Level 1.5, where further corrections are applied to compensate for different roll-angles, focal lengths (and thus plate-scales) and solar center alignements between different telescopes. Since this latter calibration is irreversible it has to be performed by the final user of the data. All the AIA data are made available for free public access 48 hours after they are received at JSOC, so that solar scientists all around the world can take advantage of the great opportunity offered by the AIA observations, quite a short time after data have been acquired.

Chapter 3

Diagnostics Techniques

In this chapter we are going to briefly present the diagnostics techniques that have been employed in our work in order to reconstruct the physical properties of the emitting coronal plasma.

In particular we will focus on the techniques that can be applied to wavelength band (rather than single line) observations in order to analyze the soft X-ray and EUV part of the coronal spectrum on the base of images obtained from the instruments described in the previous chapter.

3.1 The Coronal Emission

From the historical and observative point of view the coronal emission can be divided in three different components: the F (Fraunhofer) corona, the K (Kontinuerlich) corona and the E (Emission) corona. Both the F and K contributes are characterized by a continuum spectrum, in which absorption lines can (F corona) or can not (K corona) be observed.

Fast moving electrons of the corona scatter the light coming from the photosphere and produce the highly polarized K component, in which the absorption lines of the photosphere are blended by the large Doppler shifts due to the high termal velocity of the electrons.

The F component is also due to scattering of photospheric light, this time by heavier dust grains whose lower termal velocities preserve the Fraunhofer lines of the photospheric spectrum.

On the other hand, the E corona is made of all the emission lines that are only produced in the extremely high temperature and low density conditions of the corona and not in the colder and denser photosphere. Since thermal energies are comparable to ionization potentials of the different chemical species that compose the coronal plasma, and because of the low density

that reduces the chance of collisional recombination, high level of ionization is strongly encouraged.

Low density is also the cause of *forbidden transitions* and the resulting lines that are observed only in astrophysical environments. Compared with the allowed transitions, in forbidden transitions electrons from metastable energy levels need longer times to undergo spontaneous transitions. In higher density gases, collisions with other ions and atoms allow electrons to escape from metastable state. In the solar corona, however, such collisions are rare events and, hence, electrons are given enough time to make the spontaneous transitions releasing photons with the corresponding energy.

The electromagnetic radiation of the E-corona covers a wide spectrum that ranges from radio to hard X-rays and γ-rays, where each wavelength regime is associated with different physical processes. In this thesis we have mainly studied the soft X-ray and EUV part of the E-corona.

Due to the high degree of ionization of all the elements that compose the solar corona and to the high temperature induced capability of the corona to excite also high energetic transitions, the E corona is rich in short wavelengths lines. At such short wavelengths, the blackbody continuum from the photosphere is negligible, and consequently any radiation coming from the corona will overhelm the photospheric contribution allowing on-disk observations of the corona.

3.2 Optically thin plasma

In order to study the coronal emission and to relate it with the observed quantities we need to define the *specific intensity* I_λ (erg s^{-1} cm^{-3} sr^{-1}) as the energy (dE_λ) emitted by a source of electromagnetic radiation at a given wavelength λ that passes through a surface of area dA, at a given angle θ with respect to the perpendicular to dA, within a solid angle $d\Omega$, and in a time interval dt:

$$I_\nu = \frac{dE_\lambda}{dt\ dA\ cos\theta\ d\Omega\ d\lambda}\ . \tag{3.1}$$

How this quantity is modified as the emitted radiation passes through some intervening material located between the source and the observer is illustrated by the *radiative transfer equation* (see e.g. Carroll & Ostlie, 1996), where intensity increases are given by the wavelength dependent local emissivity coefficient (ϵ_λ) and intensity decreases are regulated by the absorption coefficient (k_λ):

$$\frac{dI_\lambda(s)}{ds} = -k_\lambda(s)\ I_\lambda(s) + \epsilon_\lambda(s)\ , \tag{3.2}$$

where every quantity is expressed as a function of the position s along the propagation path of the radiation, i.e. along the line of sight (LOS). Defining the optical depth as

$$\tau_\lambda(s) = \int_0^s k_\lambda(\hat{s}) d\hat{s} \tag{3.3}$$

allow us to obtain a limit solution for the radiative transfer equation, in the case of optically thin plasma ($\tau_\lambda \ll 1$) that well represents the evolution of the specific intensity as the light ray travels from the corona to the observer:

$$I_\lambda(\tau_\lambda) \approx I_0 + \frac{\epsilon_\lambda(\tau_\lambda)}{k_\lambda(\tau_\lambda)} \tau_\lambda \ . \tag{3.4}$$

Eq.3.4, where I_0 is the intensity of the background, shows that for optically thin plasma the specific intensity is proportional to the optical depth τ_λ which, assuming a constant absorption coefficient, gives an intensity proportional to the depth of the emitting material.

3.3 Spectral line emissivity

When an atom in an excited state j decays spontaneously to a lower state i, the energy hc/λ_{ij} is released via en emitted photon. Since this thesis is based on the study of radiation emitted by the E-corona we focus on line intensity I_{ij} (erg cm^{-2} s^{-1} sr^{-1}) rather than specific intensity I_λ (erg cm^{-3} s^{-1} sr^{-1}) .

By neglecting the background intensity (I_0), Eq.3.4 applied to line intensity gives

$$I_{ij} = \frac{1}{4\pi} \int_L \epsilon_{ij}(l) dl, \tag{3.5}$$

where the line emissivity, ϵ_{ij}, (erg s^{-1} cm^{-3}) is integrated over the column height L (cm) of the emitting plasma along the LOS.

As mentioned above, the excited atoms and ions of the Corona decay via spontaneous emission, whose probability is described by A_{ji} (s^{-1}), the spontaneous radiative transition probability. The stimulated emission, the other mechanism that induces the photon emission, does not play an important role in the Corona because the probability that an emitted photon interacts with other atoms before leaving this atmospheric layer is negligible (optically thin).

The line emissivity is given by:

$$\epsilon_{ij} = \frac{hc}{\lambda_{ij}} A_{ji} N_j. \tag{3.6}$$

N_j (cm^{-3}) is the number density of the atom in the excited state j, and contains many terms that depend on density and temperature of the plasma. In order to isolate these dependences we rewrite it as:

$$N_j = \frac{N_j}{N_{ion}N_e}\frac{N_{ion}}{N_{el}}\frac{N_{el}}{N_H}\frac{N_H}{N_e}N_e^2, \tag{3.7}$$

where N_{ion}, N_{el} are respectively the ionic specie and the element to which the ion belongs, while N_H is the hydrogen number densities.

The first factor of the right hand side, $N_j/(N_{ion}N_e)$, gives the fraction of ions in the excited level j normalized to the electron number density. The atom processes that are responsible for the excitation of the j level, in the typical Corona plasma condition, are mostly due to collisions between ions and free electrons. Also radiative ionization processes can play an important role for some strong spectral lines. This applies to lines that are emitted also in the underlying atmospheric layers such as chromosphere and transition region. However, the instruments adopted in our work (with the exception of the STEREO COR1) focus on EUV and X-ray lines which are solely emitted in the corona and in which the radiative component is negligible. This fact leads to a strong dependence of N_j/N_{ion} from N_e and explains the adopted normalization in order to remove such dependence.

The second factor, N_{ion}/N_{el}, is the relative abundance of the ion with respect to the element. This term shows a strong dependence on the electron temperature and must account for the different ionization mechanism. At the typical temperature and densities values that can be found in CHs the ionization is dominated by collisional ionization with electrons, while photoionization can be neglected because of the weak radiation field of the Corona. Under the assumption that plasma is in steady state, that is variations in density and temperature occur on time scales that are lower than the ionization time scale, the N_{ion}/N_{el} term looses any density dependence and the ratio between two successive ionization states can be calculated and shows dependence only from the electron temperature. With such approximation, known as ionization equilibrium, many authors in the literature has produced and tabulated the ratio N_{ion}/N_{el} for all the processes of interest in the corona (see e.g. Arnaud & Rothenflug, 1985; Mazzotta et al., 1998)

The third term, N_{el}/N_H, is the elemental abundance with respect to hydrogen. The study of the photospheric chemical composition began with Russell (1929) who determined the abundance of 56 elements, analyzing the spectrum of the photosphere. After a great amount of measurements, the photospheric abundances are now believed to be well known (Grevesse & Sauval, 1998), with the exception of few important elements, like Neon or

Element	FIP(eV)	Photosphere A_x	Corona A_x
H	13.6	12.00	12
O	13.6	8.66	8.83
Mg	7.6	7.58	8.18
Si	8.1	7.55	8.16
Fe	7.9	7.50	8.10

Table 3.1 *First ionisation potentials, photospheric abundances (Grevesse & Sauval, 1998) and coronal abundances (Feldman & Widing, 2003) above typical quiet regions and for selected elements.*

Oxygen (for a comparison between old and new values see Asplund et al., 2004).

While the photospheric abundance is homogeneous, different structures of Corona present important variations in the chemical compositions, and show often a dependence of such composition from the First Ionization Potential (FIP), with an overabundance of low FIP elements in the corona compared with photospheric values (Feldman & Widing, 2003).

The photospheric and coronal elemental abundances are shown in table 3.1. Both coronal and photospheric values are given in standard logarithmic scale $\log A_x = 12 + \log_{10}(N_x/N_H)$. The coronal values have been measured above typical quiet regions (Feldman & Widing, 2003).

The last term of 3.7, N_H/N_e, represents the abundance of hydrogen relative to electrons and depends on the amount of ionization of the plasma. Considering that the solar atmosphere is mainly composed by hydrogen and helium and that, at coronal temperatures, these two elements are believed to be almost completely ionized, the ratio $N_H/N_e \approx 0.85$.

The Eq. 3.7 allow us to almost totally separate the temperature dependent terms from density dependent terms. The formers can be grouped together forming the *Contribution Function* $F_{ij}(T_e)$, which is only weakly dependent of the electron density. We can thus rewrite the collisional component of the line intensity (see Eq. 3.5):

$$I_{ij} = \frac{1}{4\pi} \int_L F_{ij}(T_e) N_e^2 dl, \tag{3.8}$$

where

$$F_{ij}(T_e) = \frac{N_j}{N_{ion} N_e} \frac{N_{ion}}{N_{el}} \frac{N_{el}}{N_H} \frac{N_H}{N_e}. \tag{3.9}$$

3.4 Deriving plasma parameters

Among all the different techniques that allow solar scientists to characterize the coronal plasma from the EUV and X-ray observations, we describe here those techniques that have been adopted in this work. Furthermore, we focus on those techniques that can be adopted to obtain the plasma parameters N_e and T_e while obtaining measurements of ion or elemental abundance, as like as the fraction of ions in an excited level j is beyond the aim of this work.

3.4.1 Density diagnostics

The equation 3.8 represents the starting point for the density diagnostics techniques that have been adopted in this work. In particular, in our analysis of different coronal plasma structures, we have encountered two different plasma regimes that require distinct approaches. The first approach, that can be applied to thin and homogeneous plasma structures, requires that the emitting plasma volume is characterized by a very small temperature range, that, in first approximation, can be reduced to an isothermal plasma scenario. The second case, on the other hand, allows us to describe more complex and spatially extended structures, where the approximation of a constant temperature for the emitting plasma volume is no longer valid.

In our work we have mainly analysed data from imaging instruments which, by the mean of the different filtering materials (see chapter 2), acquire intensity data coming from wavelength range of different widths rather than single spectral lines. However, Eq. 3.8 still applies to the analysis of such wavelength band data, with the trick of substituting the spectral line contribution function F_{ij}, with the filter contribution function F_{fil}, also called filter response, that contains all the elemental abundances, the ion abundances and the fraction of ions in all the excited levels that are able to emit photons which can be detected with the given filter.

In the isothermal plasma approximation the intensity measured with a given filter becomes:

$$I_{fil} = \frac{1}{4\pi} F_{fil}(T_e) \int_L N_e^2 dl, \tag{3.10}$$

where the integral $\int_L N_e^2 dl$ is called Emission Measure (EM) and is a probe of the amount of emitting plasma along the LOS. Once the temperature of the emitting plasma volume is known, by direct measurements (see next session) or by speculation, one can calculate the filter response associated with that temperature. Indeed, for each of the adopted observing instruments a set of filter response curves as a function of temperature is provided by the instrumental scientists (see figs.2.4 and 2.9).

The EM values can thus be obtained directly from the ratio between the measured I_{fil} and the reconstructed $F_{fil}(T_e)$. In order to obtain a value for N_e of the emitting plasma volume is thus necessary to estimate both the morphology and the size of the observed coronal structure. One first approximation approach, often used to solve such problem, is to assume cylindrical shape of the structure and homogeneous electron density within such structure. The value of dL can thus be estimated by measuring the projected width of the observed structure in the plane of the sky.

In the other scenario, where the temperature cannot be considered homogeneous along the LOS of the emitting plasma volume, is useful to rewrite 3.8 as

$$I_{\rm fil} = \frac{1}{4\pi} \int F_{\rm fil} \eta(T_{\rm e}) {\rm d}T_{\rm e}, \tag{3.11}$$

where we have adopted the substitution:

$$\int \eta(T_{\rm e}) {\rm d}T_{\rm e} = \int N_{\rm e}^2 {\rm d}l, \tag{3.12}$$

and where η, defined as $\eta(T_{\rm e}) = n_{\rm e}^2 {\rm d}l/{\rm d}T_{\rm e}$, is the so called Differential Emission Measure. $\eta(T)$ represents the amount of plasma in the temperature interval between T and $T+{\rm d}T$, located along the LOS, that is responsible for the emitted radiation.

In order to reconstruct the DEM profile of an emitting plasma volume is necessary to collect as many different filter intensities as possible. These multiple observations of the same coronal structure with different filters need to be almost simultaneous, to avoid any changes in the morphology to disturb the DEM reconstruction. The only imaging instrument that clearly satisfies these two constraints is the AIA of the SDO mission (see section 2.3.1). The observed intensities I_{fil} are given by the convolution between the filter response functions F_{fil} and the same η for all the filters. To solve the problem we "just" need to find the right η function that is able to reconstruct the observed intensities in all the instrument filters. However, being η a continuos function that we want to infer from a small number of different filters observations, the problem of reconstruct such profile is ill-posed and additional constraints are required. Many algorithms have been developed in order to reconstruct the DEM profile (see e.g. Hannah & Kontar, 2012; Plowman et al., 2013), adopting different constraints to solve such ambiguity. In our work we have chosen to use a regularized inversion algorithm applied with an iteration scheme that removes the eventual negative values for the DEM (Plowman et al., 2013), that have been specially designed to analyse AIA data.

3.4.2 Temperature diagnostics

Temperature of coronal EUV emitting structures are normally obtained via the line-ratio technique, using temperature sensitive line ratios from the same ion or from ions of the same element, obtaining in such a way a measure that is independent both of the elemental abundance and of the EM of the emitting plasma volume. In our work, where we have adopted mainly imaging instrument, this technique have been adapted to wavelength band observations, with the substitution of the line emissivity ϵ_{ij} with the filter emissivity ϵ_{fil}, following the so called filter-ratio technique (see e.g. Narukage et al., 2011). Obviously this technique can be adopted only when the observed plasma can be considered isothermal.

Indeed, by taking the ration between the intensities observed with two different filters (see Eq.3.10), we obtain, for an isothermal plasma structure:

$$R_{12}(T_e) = \frac{I_{fil1}}{I_{fil2}} = \frac{F_{fil1}(T_e)}{F_{fil2}(T_e)}. \tag{3.13}$$

The coronal temperature can thus be obtained inverting the previous formula:

$$T_e = R_{12}^{-1}\left(\frac{I_{fil1}}{I_{fil2}}\right) \tag{3.14}$$

where R_{12}^{-1} is the inverse of R_{12}. In order to could uniquely identify the temperature corresponding to the observed intensity ratio, the filter ratio must be an invertible function. For example, in our work we have adopted the XRT ratio pairs *Al_poly/Al_mesh* and *C_poly/Al_mesh* (see section 2.1.1) because of their monotonous behavior and their high sensitivity in the temperature range of the analysed structures (see fig.3.1).

3.4.3 Applying the adopted techniques

All the general diagnostics techniques here described have been adapted to the different type of data produced by each instrument and to the different observing conditions encountered in each work.

In the following chapters, after introducing the science objective, we have described how we have applied and adjust the diagnostics techniques here summarize to each work and instrument.

In the analysis of the relation between BPs and jets, we have described in section 4.2 how we have obtained an intensity versus time plot for each of the studied BP, taking care of removing the corresponding background coming from the solar disk.

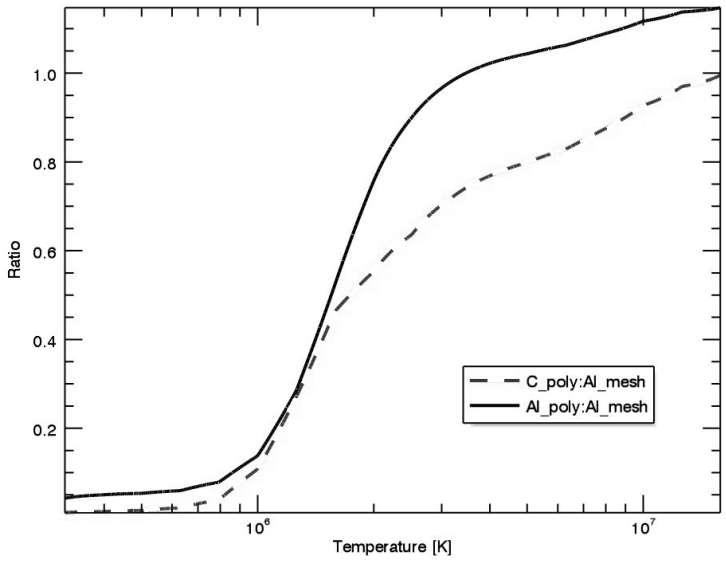

Figure 3.1 *Ratio between the filter response functions of* Al_poly/Al_mesh *(red line) and* C_poly/Al_mesh *(black line) filter pairs of the XRT. Both these ratio pairs shown a high sensitivity in temperature range between* 9×10^5 *K and* 3×10^6 *K.*

In the second work, section5.3 describes how and why we have adopted the isothermal plasma approximation which allow us to use the filter-ratio technique and obtain a measure of the temperature along the jet axis directly from intensity values measured in a pair of filter of XRT or EUVI (see eq.3.14). Next step is deriving the EM of the jet plasma along the line of sight from the measured intensity and the calculated temperature via Eq. 3.10, that gives also the electron density by measuring the jet width and supposing a cylindrical shape. By adopting standard error propagation approach (for details see Narukage et al., 2011) we have calculated the uncertainty of the obtained temperature and density values, taking care of eventually reconstructing the number of observed photons from the Data Number (see eq.5.2)

To obtain an estimate of the outflow velocity of intensity fronts within jets we have adopted space-time maps builded from tilted arrays of pixels centered on the jet axis, as described at the end of section 5.3.

While for jets the isothermal plasma approximation can often be applied

because of the reduced dimension of the analysed structures, polar plumes require a different approach where it is necessary to introduce the differential emission measure. The multichannel simultaneous images of *SDO* AIA allow a good reconstruction of the Differential Emission Measure also for coronal regions like CH where the emitted radiation gives a low photon rate. Furthermore, since the plume emission is embedded in the slightly fainter emission of the ambiente corona, it has been necessary to integrate the emission in each channel above a time interval of ten minutes. Subtracting the Differential Emission Measure profile of the plume + background from that one of the background at positions devoid of plumes gives the $\epsilon(T_e)$ profile for the plume, as described in section 6.4. In order to compare the intensity fluctuations of plume and the associated BP we have used pixel integration techniques similar to those used in chapter 4, this time building "horizontal" space-time maps instead of light curves (see section 6.2). Finally as for the jet work, we have builded detrended "vertical" space-time maps in order to emphasize the presence of outflowing disturbances within plumes as shown in section 6.3.

Concluding this chapter we would like to point out that the focus in this thesis has been posed not only on studying transient EUV phenomena observable in polar CHs, but also on characterizing these features by applying similar *imaging* methods to different structures and on testing the limit and power of such diagnostics techniques, keeping in mind that imaging instruments represent an important piece of the present solar missions and will probably play a prevailing role in the solar physics of tomorrow.

Chapter 4

Solar Polar X-ray Jets and Multiple Bright Points: Evidence for Sympathetic Activity

4.1 Introduction

X-ray jets were first reported by Shibata et al. (1992) based on observations from the *Soft X-ray Telescope* (SXT) on *Yohkoh*. They found most jets to occur in conjunction with X-ray-emitting microflares, and Shimojo et al. (1996) confirmed this association with a statistical study. Yokoyama & Shibata (1995) and subsequent studies have shown with numerical simulations that X-ray jets can occur together with microflares, via magnetic reconnection between an emerging bipole and a pre-existing "open" magnetic field. Most of the jets detected with SXT were outside of solar coronal holes (CHs).

The *Hinode/X-Ray Telescope* (XRT) experiment (Golub et al., 2007) has been crucial in revealing the occurrence of hot, high-speed, collimated jets in polar CHs, in far larger numbers than expected on the basis of previous observations (Cirtain et al., 2007). *Yohkoh* saw fewer jets in CHs, likely due in part to the poorer time cadence compared to XRT, and possibly also due in part to the ability for XRT to detect cooler temperature plasmas than SXT (Narukage et al., 2011). Interest in these ejective events is twofold: (1) their high number suggests they may have a role in coronal heating/solar wind acceleration, and (2), both observational and modeling efforts aim at understanding whether these phenomena are analogous to large scale Coronal Mass Ejections (CMEs), surges, and flares. Indeed, Moore et al. (2010)

identified two kinds of X-ray jets fueled by reconnection, "standard jets" and "blowout jets", the latter representing miniature versions of the large scale eruptions that give rise to CMEs (standard jets lack such an eruption). As in the SXT-observed jets, standard jets are the consequence of flux emergence within the unipolar field of the CH – originating at the time a Bright Point (BP) is being born (and possibly leaving no BP after their decay) – and have been successfully modeled by different authors (e.g. Moreno-Insertis et al., 2008).

CHs host other small-scale features: hereafter, we focus on BPs, identified in the late 1960s (Vaiana et al., 1970) as roundish features, with a diameter $\approx 10" - 20"$, that overlie small-scale bipolar magnetic regions, have a lifetime of hours/day, and temperatures on the order of $(1 - 2) \times 10^6$ K (e.g. Golub et al., 1974, 1977). It has been found that BPs are at least in some cases associated with CH jets (e.g. Doschek et al., 2010), similar to microflares and the SXT jets. Filippov et al. (2009) analyzed the formation of jets above small bright formations in polar CHs, suggesting a further type of X-ray jet not initiated by reconnection. BPs show intensity fluctuations on time scales of a few minutes to hours (e.g. Kariyappa & Varghese, 2008). Previous works have dealt with different aspects of individual events. The present paper, on the contrary, focusses on the interaction between closely located CH BPs that appear to undergo intensity fluctuations as a group: in other words, complexes of BPs undergo coordinated intensity variations; sometimes these fluctuations accompany jet occurrence.

In this chapter we investigate the question of whether the BP complex intensity changes are *correlated* with jet occurrence, and consider implications for such a correlation for the jet-production mechanism. We examined *Hinode*/XRT observations of BP complexes and made a photometric analysis of their brightness fluctuations over several hours. We then searched through the data for jets occurring within the BP complex. Based on our findings, we present a new aspect of X-ray jets that is perhaps critical to their generation.

4.2 Observations

We analyzed *Hinode*/XRT observations of the northern polar CH, acquired on 2–4 November, 2007. The XRT images have a cadence of 1 min, a spatial resolution of 1.032 arcsec/pixel and have been calibrated with the standard tools, including the Solar SoftWare (SSW) packages's xrt_prep.pro IDL routine. We selected two sub-regions of the CH where several BPs are present, as shown in Figure 4.1. Individual BPs within the sub-regions of Figure 4.1 were marked off by rectangular boxes, and we follow these boxes (tracking

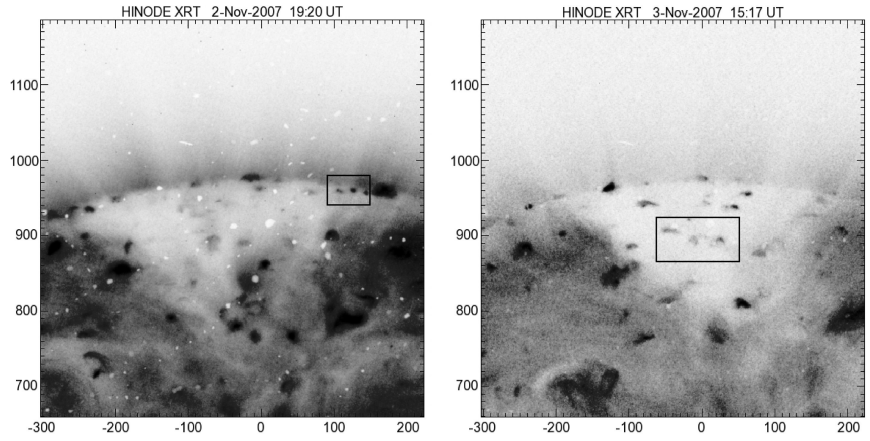

Figure 4.1 *Hinode/X-Ray Telescope* images of the North polar coronal hole, with superposed small rectangular areas selected for: our first study, over 2–3 November 2007 (left panel); and our second study, over 3–4 November 2007 (right panel). The x and y axes are arcsec from Sun center. Left panel: Al-mesh image taken on November 2; right panel: Al-poly image taken on November 3.

solar rotation) over the entire period of our study. For each BP we analyzed, we verified that the box we defined contained within its boundaries the entirety of the BP, for the duration of that BP's lifetime.

Brightness fluctuations of the BPs have been evaluated by summing the intensities of all pixels within the boxes and subtracting a background value. The latter has been estimated by summing the intensity values of all pixels along the borders of the boxes and normalizing the value we obtained to give the average background value per pixel. The following subsections describe the sequence of events observed in the first data set (acquired on November 2/3) and in the second data set (acquired on November 3/4) within the selected sub-regions.

4.2.1 First data set: Bright Points and Jets on November 2/3, 2007

Within the sub-region shown in the left panel of Figure 4.1, we identified seven BPs over $\approx$ 20 hours of observations, from Nov. 2, 11:45 UT to Nov. 3, 08:00 UT. During this period, some BPs fade out, while others become visible.

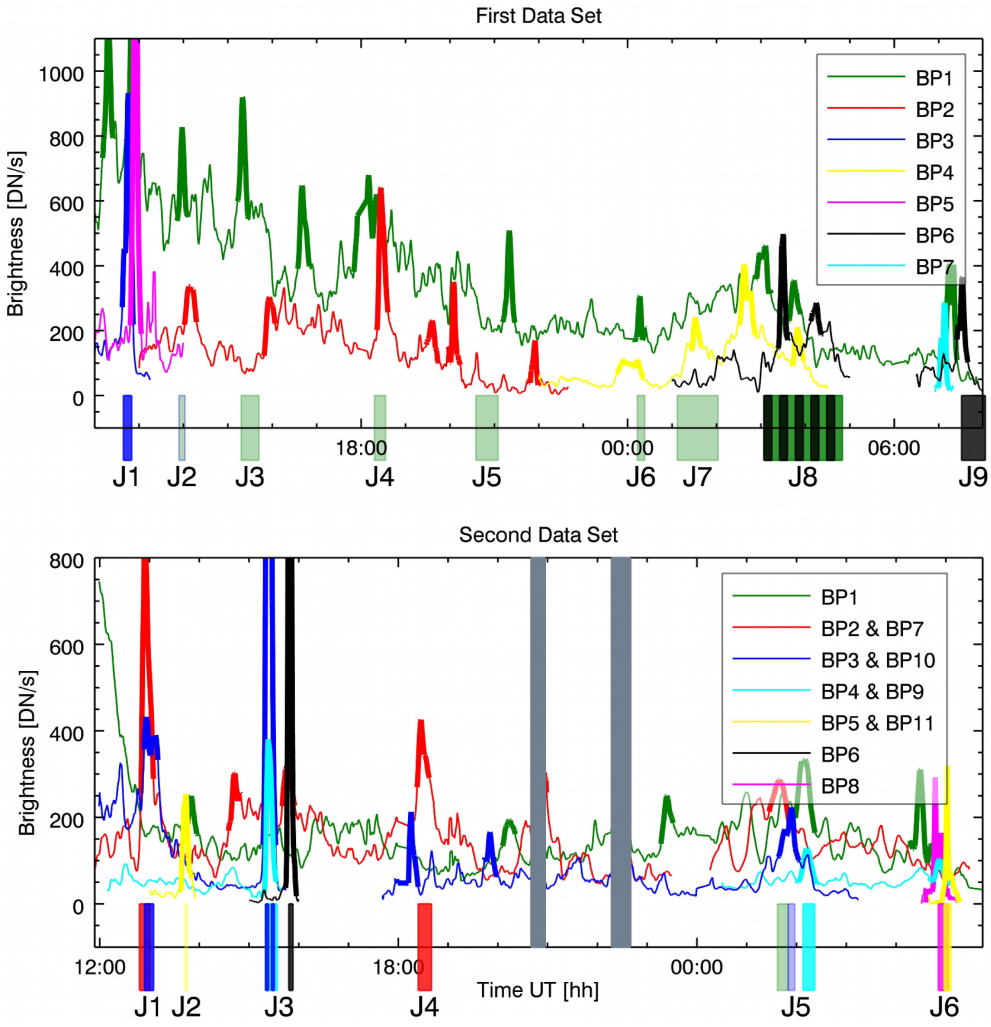

Figure 4.2 Top: Bright point (BP) brightness (DN/s) profiles as functions of time, within the coronal hole (CH) region selected on November 2, 2007. Different BPs are identified by different colors, with intensities determined as explained in the text. Thicker lines highlight the "local brightness maxima". Boxes along the abscissa indicate jets, with the colors the same as that of the BP where the respective jets originate, the box width giving the duration of the jets, and the box hue giving an approximate relative indication of the jet intensity. The horizontal axis gives time (hours), starting on 2007 Nov. 2, 12:00 UT; the full data set covers $\approx$ 20 hours. We point out that the two-colored box J8 corresponds to a unique jet originating in BP1 and gradually shifting to BP6. Bottom: same as the top plot, but for the CH region selected on November 3, 2007. Time (hours), along the horizontal axis, starts on 2007 Nov. 3, 12:00 UT; the full data set covers $\approx$ 18 hours. Between 13 and 16 UT, some local brightness maxima are so intense that they fall off the vertical scale of the plot. The grey shaded vertical stripes around 21 and 22 UT correspond to time intervals of noisy data that we omitted from our analysis.

Figure 4.2 shows the variation in intensity (DN/s) with time of all seven BPs. Solid lines are color coded, each corresponding to a specific BP. In order to clearly correlate jet events with a BP activity increase, we define "local brightness maxima" as any brightness interval whose values are at least six sigma higher than the 1-hour averaged background brightness curve. Such maxima are highlighted in the figure with thicker lines, and have a typical full width at half maximum of about 15 minutes. Jets observed within the examined sub-region are represented, along the abscissa, by small boxes sequentially numbered, whose color matches the color of the BP where the jet originates. The width of these jet boxes gives the duration of the respective jet, and their hues are roughly proportional to the respective jet's brightness. The time resolution adopted for the plot is that of the data (about 80 images per hour), but a 4-point running mean of the original data is used in the figure. Weaker jets have been identified only after summing up a few images, and thus they have a degraded temporal resolution compared to the original data. Whenever the duration of two events (either BP local brightness maxima or jets) at least partially overlap, they are considered to be "almost simultaneous".

From the top panel of Figure 4.2, we find the following when a jet occurs. 1) The BP at the jet's base most of the time brightens almost simultaneously with the jet; 7 out of 9 jets do this, with the exception of J7, which does not show any significant BP brightness increase, and J5, which has a delayed (15 minute) BP brightness maxima. 2) Almost always, there is also a brightening in a nearby BP, where "nearby" means within the rectangular box under study; 7 out of 9 cases are like this, with the exceptions being J3 and J5. These points suggest that jets are the manifestation of some kind of activity that involves multiple BPs, rather than a lone BP. In addition, we have found that even in cases where jets appear to be accompanied by fluctuations in a single BP only, they might be correlated with one or more additional BPs located just outside the studied region. For example the jet J5 is related with a huge brightness increase of a BP centered at West 165″, North 960″, hereafter BP10 (see Fig.4.1, left panel), whose brightness vs. time profile appears in Fig. 4.3.

So in addition to the above two conclusions, we may add a third: 3) caution should be exerted whenever jets appear not to be accompanied by multiple BP brightness fluctuations, because they may be associated with peaks of BPs external to the examined area. We conclude that 7 out of 9 jets observed in this first data set are associated with at least two BP maxima, 3 of them being correlated with peaks in three BPs (J1, J8 and J9).

In most cases there is an apparent propagation of energy/disturbances through the BPs complex.

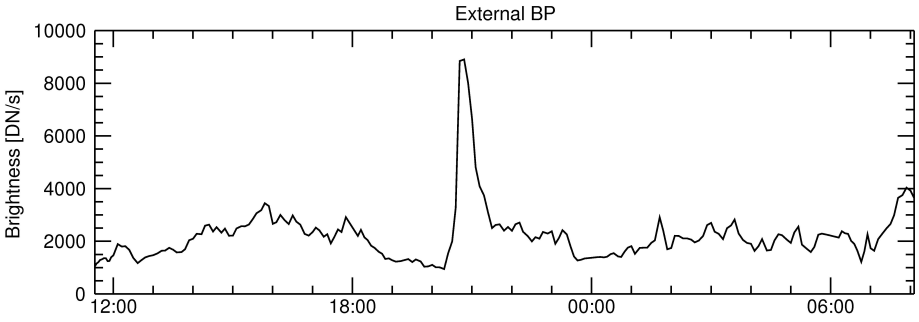

Figure 4.3 Brightness vs time profile of BP10, a Bright Point located just outside the studied region. The time (hours), given by the horizontal axis, starts on 2007 Nov. 2, 11:45 UT.

In Figure 4.4, upper panels, we present a typical example of a propagating brightness fluctuations accompanied by jet occurrence. The peak brightness of BP3a (at $\approx$ 12:40 UT) is followed (after $\approx$ 6 min) by the peak brightness of BP3b, which, in turn (after $\approx$ 4 min), is followed by the simultaneous brightenings of BP1 and BP5a, and, 6 minutes later, by the BP5b maximum. Along with this sequence of brightenings, two jets occur: a brief jet (Ja) is observed at the time of the BP3 maximum, and a second one (Jb), lasting about 3 minutes, occurs at the time when BP3b reaches its brightness maximum.

This sequence of events is summarized in Table 4.2.1, top section, where jets and BPs appear with the same notation used in the upper panels of Figure 4.4.

4.2.2 Second data set: Bright Points and Jets on November 3/4, 2007

Figure 4.2, bottom panel, shows the BP brightness fluctuations and jets occurring in the CH sub-region selected on November 3/4, 2007 (right panel of Fig. 4.1). This plot is based on data taken in the Al_poly filter. The Al_mesh filter used in the previous data set is more sensitive to cooler temperatures than is the Al_poly. Nonetheless we find similar results in both data sets regarding the correlation between BP intensity fluctuations and occurrence of X-ray jets, and hence our results are independent of the filter adopted when taking data (and of the contamination filters might have suffered; Narukage et al., 2011).

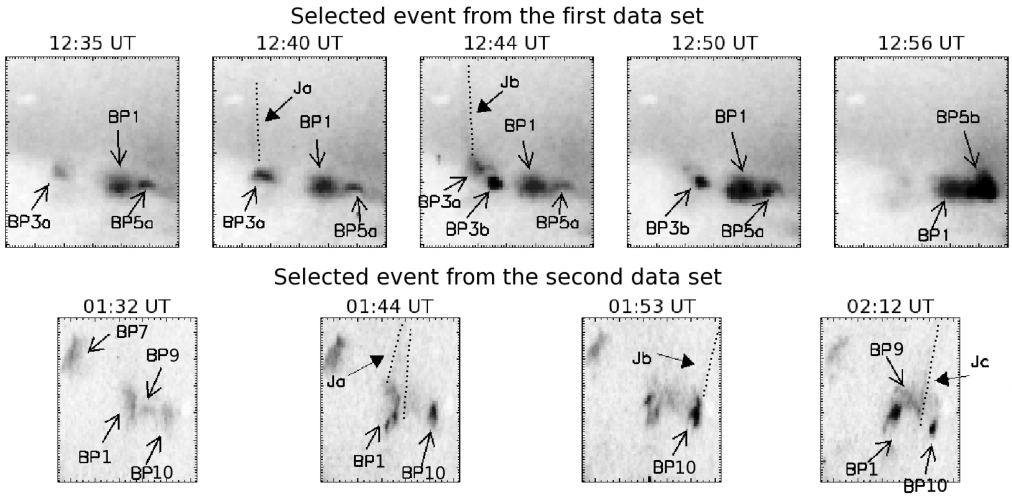

Figure 4.4 Upper panels: A sequence of images taken on November 2, 2007, by *Hinode*/XRT in the Al_mesh filter, over about 21 min, where Bright Points (BPs) brightness fluctuations are apparent and sequentially move through the BP complex. The time sequence of the event is summarized in Tab. 4.2.1, upper panel. To help visualize the two jets occurring over this time interval dotted lines have been drawn onto them (second and third panel).
Lower panels: A sequence of images taken on November 4, 2007, by *Hinode*/XRT in the Al_poly filter, over about 40 min, where BPs brightness fluctuations are apparent and sequentially move through the BP complex. The time sequence of the event is summarized in Tab. 4.2.1, lower panel. The occurrence of jets is highlighted by dotted lines.

Several BPs in this second data set occur over very short periods and have sharp maxima in intensity. After they fade away, occasionally a new BP appears in the same location. BPs observed in the same location have been assigned the same color in Fig. 4.2, but are referred to with different numbers. Furthermore in this second data set, jets from different BPs can occur almost simultaneously: we consider them as components of the same "jet event", and they are referred to with the same number.

As in the previous data set, there are cases where jets appear to be correlated also with local brightness maxima occuring in BPs outside our selected observation box. For instance the jet J4 is also correlated with the brightness maximum at 18:37 UT of a BP located 15" south and 25" east of BP2. From the analysis of this second data set we can surmize that 6 cases out of the 6 jets events satisfy both point 1) and point 2) of the previous

First data set		
Date	Time	Event
2-Nov	12:40	Maximum for BP3a
2-Nov	12:40	Start and end of Ja
2-Nov	12:44	Start of Jb
2-Nov	12:46	Maximum for BP3b
2-Nov	12:47	End of Jb
2-Nov	12:50	Maximum for BP1
2-Nov	12:50	Maximum for BP5a
2-Nov	12:56	Maximum for BP5b
Second data set		
4-Nov	01:41	Start of Ja from BP1
4-Nov	01:52	End of Ja
4-Nov	01:53	Start and end of Jb
4-Nov	01:53	Maximum for BP10
4-Nov	02:05	Maximum for BP1
4-Nov	02:10	Second maximum for BP10
4-Nov	02:10	Start of Jc
4-Nov	02:14	Maximum for BP1
4-Nov	02:19	End of Jc

Table 4.1 Time sequences for two multiple brightenings events

section. Furthermore, 3 out of 6 cases jet are associated with local brightness maxima from more than two BPs.

The lower panels of Figure 4.4 show a sequence from this second data set where BPs sequentially brighten and fade while jets occur, as summarized in Table 4.2.1, bottom section. We conclude that the phenomena seen in the two datasets are consistent and analogous. This suggests that the correlation between jet occurrence and the brightening of multiple BPs is fundamental to the nature of the jets, and both should be accounted for by a common mechanism.

4.2.3 Results and Discussion

The two data sets concur; summarizing the findings: when a jet occurs, there are likely to be multiple X-ray BP intensity fluctuations at the base of the jet.

There may be standard jets/blowout jets within our sample, however the analysis of individual jets will pre presented in the following chapters. Models and ideas for jet formation can, to more-or-less of a degree, provide one explanation for correlation between jet occurrence and BP brightenings. In standard jets, one main X-ray brightening should occur, as in Fig. 1 of Moore et al. (2010), which is based on the works of Shibata et al. (1992), Yokoyama & Shibata (1995), and others. For the blowout jets at least one distinct BP is expected, in the same location where it appears in the standard jets (the compact "flare-like" loops formed following reconnection between the emerging bipole and the open field; see Figs. 1 and 10 in Moore et al., 2010). Also, an additional X-ray brightening occurs after the bipole blows out and the expelled fields reconnect, but in the examples of Moore et al. (2010) the blown out bipoles have a diffuse nature in XRT images (see their Figs. 6 and 8), instead of the rather distinct BPs we observe in this study. Other models for jet formation that do not invoke reconnection energy input have been proposed by Filippov et al. (2009), It is not obvious whether any of the current X-ray jet models can explain correlations that include more than two BPs.

We now present an alternative possible explanation for the apparent propagation of activity among multiple BPs in conjunction with jet formation.

Brightness fluctuation of BPs can result from either the BP area changing with time, and/or because the BP undergoes a variation in temperature (Kariyappa et al., 2011). In actuality, area and temperature changes may be related and naturally result from magnetic field emergence/submergence/-reconnection as the agent responsible for the observed modifications. We suggest that gradual BP brightenings, leading to the brightening of a whole BP complex and to minor brightness peaks (see, for instance, the slow brightening of BP1, BP7 and BP10 and the minor peaks in these BPs that occur on Nov. 4 between 00:00 and 04:00 UT), are promoted by gradual phenomena such as flux emergence or flux cancellation, possibly coupled with BP motions and changes in their mutual separations (as sometimes observed in our data) and ensuing gradual reconnection. On the other hand, in this scenario abrupt changes (narrow brightness maxima and/or jets) could be triggered by sudden connectivity changes, that occur when some magnetic field stability threshold value is reached. As a consequence, sudden connections to nearby regions are established, and/or extra energy pushes plasma

along open field lines.

Our speculation for these field interactions occurring on the relatively small-size and weak-field scales found in polar CHs is motivated by events that have been observed on larger scales. Machado et al. (1988), analyzing flares observed by the *Hard X-ray Imaging Spectrometer* experiment (van Beek et al., 1980) on *Solar Maximum Mission*, came to the conclusion that interaction of magnetic bipoles was essential for triggering flares. According to those authors, there was not a single case, in their data sample, where flares did not encompass "two or more bipoles", and the impulsive phase of flares occurred at the time of rapid spreading of activity over adjacent structures. Also, they argued that gradual evolution of the magnetic configuration leads to gradual changes in the energy of the interacting bipoles. On an even larger scale, Poletto et al. (1993), studying flares within an active region complex, pointed out that intermittent, sequential, sympathetic activity between the two regions of the complex led to flare occurrence. Based on these studies of larger-scale events, we propose that the BP and CH X-ray jet activity observed in our data is the small-scale end of the flare and interacting-region phenomena occurring on active-region size scales. Changes in the connectivity cells (i.e., magnetic regions bounded by separatrix surfaces, e.g. Poletto et al., 1993) induced by the evolution of the magnetic field are at the root of this behavior: interactions among the cells and the ensuing instabilities lead to flares and to a spread of activity over distant locations. This happens on the active-region scale for large flare events; we are proposing that it also occurs on much smaller scales inside of polar CHs for the BP and X-ray jet events.

Quite obviously, these ideas are speculative at this time, as our current data set, lacking adequate-resolution magnetic data, does not allow investigation of this possibility. This idea is however potentially testable by using simultaneous magnetic field observations with high spatial and temporal resolution; this is a challenging prospect for events near the pole, but may be possible for events occurring within low-latitude CHs, if suitable analogous jets and BPs can be observed there.

Chapter 5

Physical parameters of standard and blowout jets

5.1 Introduction

The *Hinode/X-ray Telescope* (XRT) telescope, because of its higher spatial and temporal resolution and its wide temperature coverage (Kano et al., 2004; Golub et al., 2007), detected a higher number of X-ray jets in polar coronal holes (CHs) than expected on the basis of previous *Yohkoh* observations (Cirtain et al., 2007). This raised high interest in these events, with the prospect that they could be small-size, low-energy phenomena corresponding to classical flares, and that the polar jets might contribute to the high speed solar wind emerging from polar holes. As far as their similarity to large scale events, Moore et al. (2010, 2013) presented evidence that jets come in two different kinds, about one-half of them being "standard" events, that fit the standard reconnection scenario between emerging flux and open unipolar fields, with the remaining ones being "blowout" jets that result from the eruption of a magnetic arch along with the ejection of plasma in a process that may be the miniature scale of what happens in major CME events.

The overall characteristics of jets, including their size, frequency, and duration, have been examined by, e.g. Savcheva et al. (2007), while their physical properties have been described by several authors who, however, did not differentiate between the two proposed categories of jets. The outflow speed of jets has been studied by, e.g., Kim et al. (2007), on the basis of *Hinode/Extreme-ultraviolet Imaging Spectrometer* (EIS) data. Culhane et al. (2007) used the same kind of data to study the temperatures and

outflow speed of two jets: because their light curves showed a post-jet enhancement in cooler lines the authors suggested that plasma was falling back to the Sun and hence that jets did not reach the outer corona. Nisticò et al. (2011) built temperature maps of jets observed by the *Extreme UltraViolet Imager* (EUVI) and *Coronagraph1* (COR1) telescope on the SECCHI package (Howard et al., 2008) onboard the *STEREO* (Kaiser et al., 2008) mission; they used the 195 Å to 171 Å filter ratio technique, and gave the thermal evolution of the observed events. The temperatures inferred from *Hinode*/EIS and *STEREO*/SECCHI did not completely agree: Culhane et al. (2007) give values ranging between 0.4 and 5 MK, while Nisticò et al. (2011) find values range between 0.8 and 1.3 MK. Whether this difference originates from the inadequacy of the single-ratio technique to describe the jet temperatures fully, or whether there are differences between jets reaching high in the corona and jets falling back to the Sun, is not clear. In other work, also not specifying the type of jets being analyzed, Doschek et al. (2010), observed one jet with *Hinode*/EIS and concluded that plasma within the jet had a temperature around 1.4 MK. Also, Madjarska (2011) performed a thorough analysis of a jet observed with *SOHO*/SUMER, *Hinode*/XRT and EIS, and *STEREO*/SECCHI EUVI *A* and *B* instrumentation, and found temperatures as high as 12 MK at the jet footpoint, while the outflowing plasma had temperatures ranging between 0.5 and 2 MK. On the other hand, blowout events have been recently studied, mainly using data from the *Atmospheric Imaging Assembly* (AIA, Lemen et al., 2012) instrument on board of the *Solar Dynamic Observatory* (*SDO*) mission, by Morton et al. (2012) and Shen et al. (2012) who focused, respectively, on the quasi-periodic phenomena associated with these kind of ejections and on observations of the bubble-like and jet-like CMEs associated with the blowout event. The latter studies aim at understanding the mechanism giving rise to blowout jets and identifying their accompanying features, rather than at deriving their physical parameters.

In this work we analyze two ejections, one each whose characteristics comply with the properties of standard jets and blowout jets. We determine their temperatures, densities and outflow speeds, in order to investigate whether the two jet types have different physical parameters. We also give the temporal profiles of these quantities and their profile along the jet structures. Using the estimates obtained for physical parameters of the events allows us to make a crude evaluation of the energy budget of the standard vs. the blowout ejection, and to put some constraint on the magnetic field energy release that fueled the jets. The chapter is organized as follows: in Section 5.2 we describe the data sets used in our analysis and the properties of the jets we examined; in Section 5.3 we illustrate the spectroscopic techniques by which we inferred the jet physical parameters; Section 5.4 gives results;

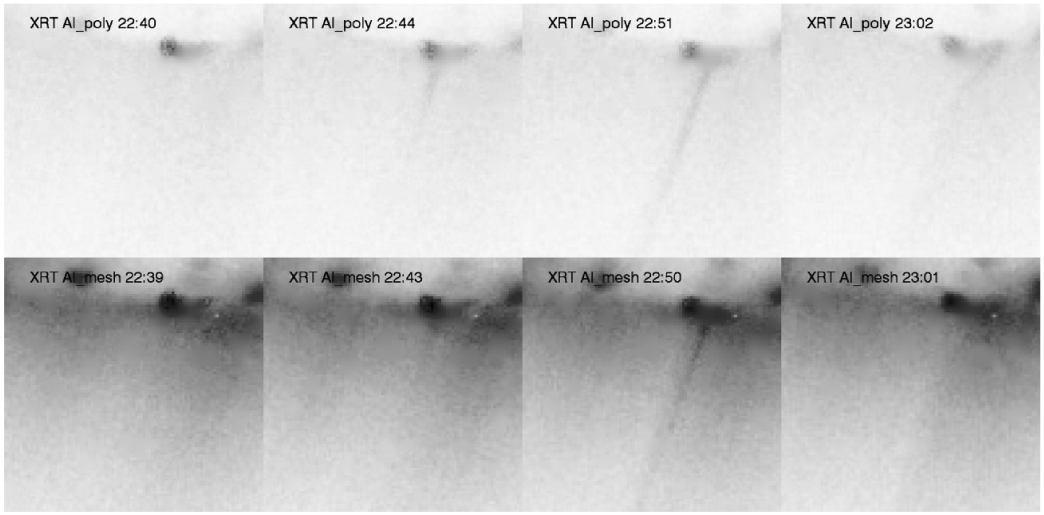

Figure 5.1 Images showing the evolution of the standard jet, as observed in the *Hinode*/XRT *Al_poly* (top row) and *Al_mesh* (bottom row) filters, on 2008 July 1. The first panel on the left (top and bottom rows) shows the pre-jet corona.

in Section 5.5 and Section 5.6 we concluded and give a crude estimate of the jets energy budget, and then compare our results with predictions from theoretical models.

5.2 Observations

We have selected two prominent events that are well-observed and good representatives of the two jet types. Both are limb events, with this choice we are able to minimize problems associated with isolating the jet emission from the contribution of the fore- and background corona.

As a good example of standard jet we selected an event, rooted in the southern polar CH at 115 arcsec E, 970 arcsec S (as seen by *Hinode*/XRT), that started at 22:44 UT on 2008 July 1, and lasted $\approx$ 20 minutes. *Hinode*/XRT images of the jet (Fig. 5.1) show that it has the typical features of a standard jet: an X-ray flaring bright point (BP) located off to the side of the jet and a jet spire that migrates in a direction away from the BP with time over the event's lifetime. These properties comply with predictions from the standard model of Shibata et al. (1992), where the jet occurs as a consequence of reconnection between emerging flux and unipolar ambient fields. The jet and the associated BP were observed also by *STEREO B*, while they fall outside the *STEREO A* field of view, the two spacecraft at that time

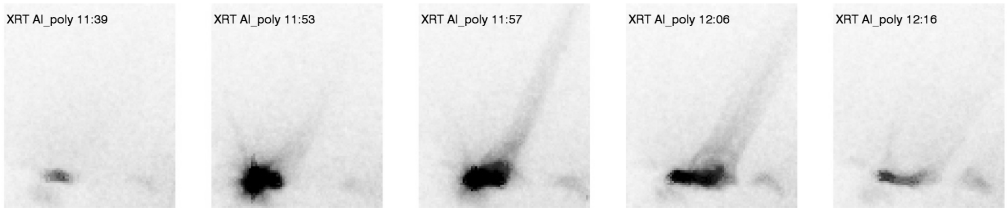

Figure 5.2 *Hinode*/XRT *Al_poly* images of the evolution of the blowout jet, which occurred on 2007 Nov 3. The left panel shows the pre-jet corona. There are no images closer in time to the jet initiation because of a 15 minutes gap in *Hinode* data.

being separated by ≈ 59 degrees.

Over the jet lifetime the *Hinode*/XRT telescope took data in three different filters: *C_poly*, *Al_poly* and *Al_mesh*, with a cadence of about 110 s, exposure times, respectively, of 33, 12 and 23 s with a plate scale of 1.0 arcsec pixel^{-1}. The response functions of these filters (together with some filter ratios) can be found in Narukage et al. (2011). The EUVI instruments on board the *STEREO B* satellite acquired images in 4 different narrow band filters with a plate scale of 1.6 arcsec pixel^{-1}: the 171 Å waveband (which includes FeIX and FeX lines with peak sensitivity for plasma at 1.3×10^6 K), with an average cadence of ≈ 150 s and an exposure time either of 16 s or 4 s; the 195 Å waveband (which includes lines from the FeXII and FeXXIV ions and is most sensitive to plasma at $T = 1.5 \times 10^6$ K), with a cadence of 600 s and exposure time of 16 s; the 284 Å waveband (which includes the FeXV line at 284 Å and is most sensitive to plasma at $2 \times 10^6 K$) with a 1200 s cadence and 32 s exposure time; and the 304 Å (that is dominated by the HeII line and has its peak sensitivity at $\approx 6 - 8 \times 10^4$ K) with cadence of 600 s and 4 s exposure time. The response functions of these filters as a function of temperature are given by Wuelser et al. (2004) and by Howard et al. (2008).

The blowout jet occurred on November 3, 2007, in the northern polar CH, at 170 arcsec W, 950 arces N, as seen by *Hinode*/XRT, at $\leq$ 11:53 UT and had a duration of about 30 minutes. *Hinode*/XRT took data only in the *Al_poly* filter, acquiring images with a 40 s cadence and an exposure time of 16 s.

Fig. 5.2 shows a sequence of XRT images from this event that display the typical characteristics of a blowout jet, such as the X-ray flaring of the whole base arcade, the blowout eruption of the core field and the extra jet strands rooted at different locations within the flaring BP. Further evidence

for classifying this event in the blowout category are given in Sec. 5.4.2.

Observations of the jet and the associated BP have been acquired also by both *STEREO* spacecraft (separation $\approx$ 40 degrees). The cadence and exposure times for both EUVI *A* and *B* are, in the 171, 195, 284 and 304 Å wavebands, respectively: 150 and 4 s; 600 and 16 s; 1200 and 32s; 600 and 4s. By comparing simultaneous images of the jet acquired by *STEREO A* and *B* [1] in the 171 EUVI channel we can reconstruct its 3-dimensional structure at a given time. This is especially useful in considering the possibility that we could be observing a "magnetic twist jet", produced by reconnection between twisted and untwisted flux tubes; such jets were suggested twenty years ago by Shibata et al. (1992), and one was indeed observed in *STEREO* data by Patsourakos et al. (2008) and modeled e.g. by Pariat et al. (2009). Emergence of a twisted flux rope might relatively easily result in a blowout jet where the base arch erupts. Indeed, *SDO*/AIA have recently provided evidence of blowout jet and untwisting field (Morton et al., 2012; Chen et al., 2012).

In Fig. 5.3 the left panels show one strand of our blowout jet (see Sec. 5.4.2) as observed by EUVI *B* in the 171 Å channel at 12:01 UT (upper panel) and at 12:06 UT (lower panel). The right panels show the 3-dimensional reconstruction obtained by comparing the EUVI *B* 171 images with the corresponding simultaneous[1] images from EUVI *A* using the *scc_measure* routine of the Solar SoftWare (SSW) package. While the 3D reconstruction at 12:01 UT shows clearly that the jet strand is, at that time, characterized by a twisted magnetic line, the 12:06 UT reconstruction presents evidence for the relaxing to an untwisted field line.

Another telescope that might provide relevant information about the events is the COR1 coronagraph onboard the *STEREO* missions, which acquires images with a cadence of 5 minutes over a FOV that extends from 1.4 to 4 solar radii. Detecting the jet in COR1 FOV implies the jets reach high enough to possibly escape into the heliosphere. We will examine this in Sections 5.4.1 and 5.4.2.

5.3 Data Analysis

XRT and EUVI multi-filter data of, respectively, the standard and blowout jets allow us to measure the temperature and the electron density of the

[1] We point out that simultaneous images of the Sun are acquired by the STEREO A and B instrumentation by imaging the Sun at slightly different times, depending on the distance from the Sun of the two spacecraft. For the jet on November 3, 2007, images have been taken with a 43 s time separation. See $http://stereo-ssc.nascom.nasa.gov/cgi-bin/make\_where\_gif$

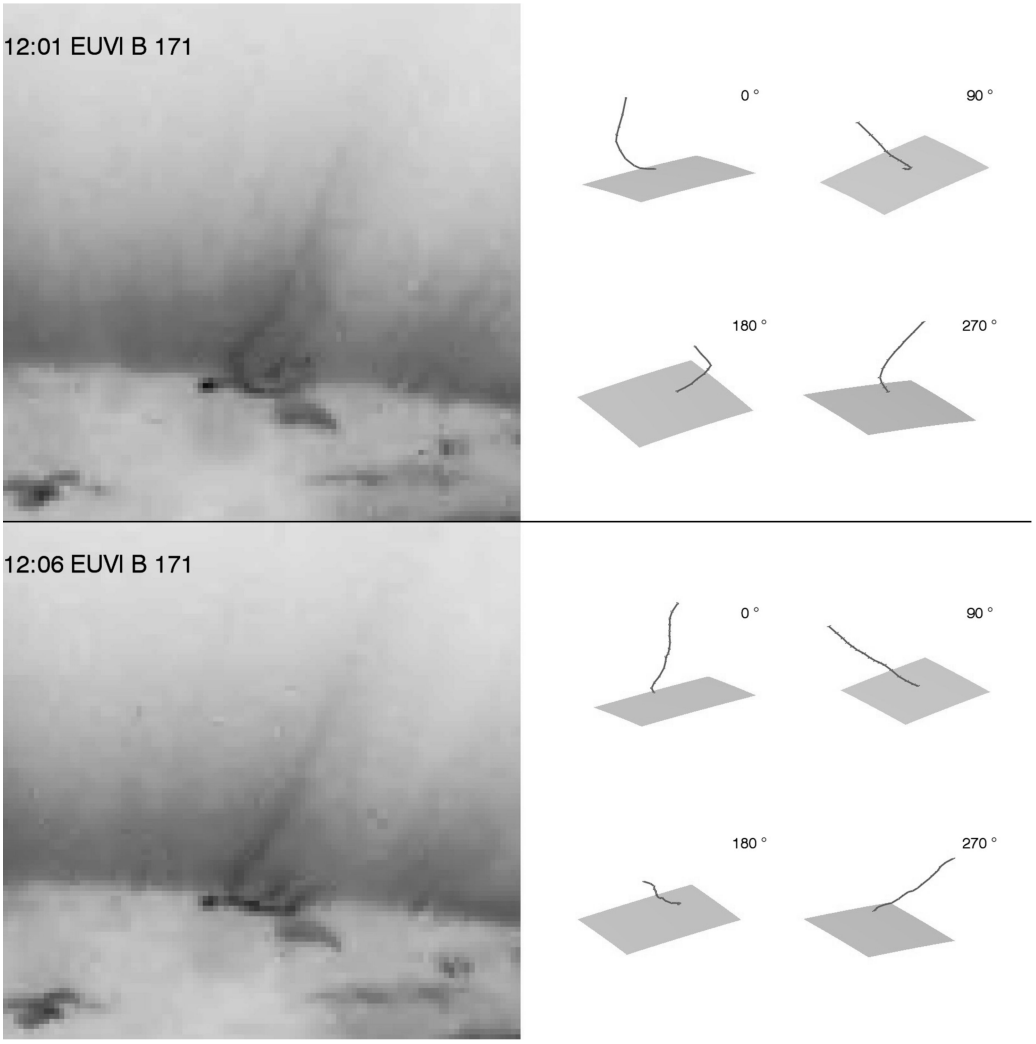

Figure 5.3 Left panels: one strand of the blowout jet as observed by EUVI B in the 171 Å channel at 12:01 UT (upper panel) and at 12:06 UT (lower panel). Right panels: the 3D reconstruction at 12:01 and 12:06 UT of the strand from *STEREO A* and *B* EUVI images in the 171 Å channel, indicating an untwisting of the flux tube (viewing angles in degrees).

jet plasma via the "filter-ratio method". Filters on the XRT and EUVI telescopes are characterized by a response that depends on temperature, F_{fil} (usually given as DN s^{-1} $pixel^{-1}$ for a unit Column Emission Measure (CEM, cm^{-5})). The measured intensity I_{fil} in a given filter can be written as

$$I_{fil} = F_{fil}(T) \int n_e^2 dl, \tag{5.1}$$

which shows that the measured intensities (in DN s^{-1} $pixel^{-1}$) depend on the filter response, which is a function of temperature; this filter response also depends upon the abundance of the element whose lines enter the temperature regime probed by the filter. The intensity also depends on the plasma column emission measure, CEM= $n_e^2 l$, where we assumed $n_e = n_i$, and l is the depth of the emitting region along the line of sight (LOS). If the intensity of lines formed at temperature T_{line} is measured by two different filters, the ratio of the measured intensities gives the temperature of the plasma where the lines form, provided they originate within the same region and, hence, have the same EM.

While the "filter-ratio method" is quite simple in principle, it conceals problems not immediately obvious. For instance, the same value of the filter ratio may correspond to a number of different temperatures. Or the emitting plasma may not be isothermal, which is a quite serious problem that may be somewhat overcome by using multiple filter ratios. Additional difficulties arise when we need to find the temperature of a feature embedded in a region whose contribution has to be separately identified before finding the temperature of the confined structure; for example, for a jet, this means subtracting the contribution of the fore- and background corona that add to the jet LOS emission.

We now describe how we inferred the jet temperatures via the filter-ratio technique. As a first step, *Hinode* and EUVI images were calibrated via the SSW *xrt_prep* and *euvi_prep* routines to obtain calibrated images normalized to the exposure time. We then selected an image at a time prior to, but as close as possible to, the time of the jet initiation, to be used as a background reference image. We then identified the jet in successive images, and a "mask" of fixed width and height was determined such that a significant part of the jet could fit in the box, including at the time of its maximum extension; the mask changes position with time, following the jet displacement mentioned above, but keeps a fixed height and width. We did this for each wavelength that we used for the study.

The same mask was used to select an area of the same size and location in the background image: pixels within this area are representative of the coronal hole emission and, possibly, of the plumes that overlap the jet along

the LOS. We then degraded the resolution of XRT data, binning over 2 × 8 pixels (i.e., 2.1 × 8.2 arcsec) respectively across and along the jet axis. Analogously EUVI data have been degraded binning over a 2 × 2 pixels (3.2 × 3.2 arcsec). The binning across the jet has been dictated by the width of the jet (2 arcsec), - hence we ignored the transverse structure of the jet -, while we selected the binning along the jet axis to provide a signal to noise ratio ≥ 20. We adopted the same binning to infer the profile of the intensity vs. distance of the background over the positions later occupied by the jet. These degraded data have been used to build the profiles of intensity vs. distance-along-the-jet axis that appear in Figs. 5.4 and 5.8. The jet intensity profile has been fitted with a fourth-order polynomial (to allow dishomogeneities, if any, to show up), while the background profile has been fitted with a second-order polynomial, adequate to represent its behavior, as we assumed the background intensity keeps constant over the duration of the jet. Because the jet intensity profile includes emission from the ambient corona, the jet emission has been isolated by subtracting the background intensity profile from the jet intensity profile. At each time, the maximum height reached by the jet is set to the height where the jet and background intensities differ by at least 2σ, where $\sigma = \sigma 1 + \sigma 2$ is the sum of the standard deviation, $\sigma 1$, of the background, and of the jet, $\sigma 2$. The latter has been calculated assuming a Poisson distribution for the incoming photons. For the XRT data we have used the SSW routine xrt_cvfact to obtain the temperature-dependent conversion factor $K^{(1)}$ between the measured Data Number, DN, and the incoming photons N_{ph}:

$$N_{ph} = \frac{DN}{K^{(1)}(T)}, \tag{5.2}$$

(see eq.10 in Narukage et al., 2011), and followed the procedure of Narukage et al. (2011) to calculate the standard deviation in the filter ratios and temperature.

The EUVI data are converted to photons by the calibration procedure. The error of the background intensity is given by the 1σ uncertainty in the adopted fit coefficients.

Once the jet intensity has been isolated, we take the ratio between the available filters. In particular for XRT we use the filter pairs Al_poly/Al_mesh and C_poly/Al_mesh, as these ratios are monotonic functions of temperature over the range expected in our analysis. For EUVI data we take the ratios 195/171 and 284/195, because the 171 and 284 filters are sensitive to different temperature regimes. The EUVI ratios are monotonic over limited temperature intervals; this implies that we have to select a temperature range a priori for each filter ratio. In this work we selected $7 \times 10^5 K < T_{195/171} < 2 \times 10^6 K$

and $1.26 \times 10^6 K < T_{284/195} < 2.8 \times 10^6 K$, as over these intervals the ratios are linear functions of temperature; lower temperatures are unrealistic and temperatures higher than 2.8×10^6 K correspond to temperatures too high to be compatible with our ratios and/or they would imply no emission in the 195 Å waveband, contrary to what we indeed observe.

The observed ratios have been compared with the predicted ratios of the filters, computed from the filter response functions F_i, assuming the coronal abundances from Feldman (1992) and the ionization equilibrium of Mazzotta et al. (1998), and we obtained a temperature profile along the jet at each time an image had been acquired. Assuming a cylindrical jet shape with a cross section diameter (l) given by the width of the jet, we also calculated the jet and background EMs, and the jet electron densities (see Eq. 5.1). Obviously, our approach implicitly neglects out-of-equilibrium effects that might be at work in the jet plasma: these have been described, in flaring loops, in, e.g., the work of Bradshaw & Mason (2003). Recalculating filter responses and ratios for out-of-equilibrium plasmas is a major effort far beyond the aim of the present work. However, we call the readers' attention to this possibility and point out that non-equilibrium effects are minimized whenever jets keep a constant temperature in time and throughout their structure.

A further parameter we calculated from the XRT data analysis is the outflowing plasma speed in the jet. To infer its value, for the standard jet, we evaluated visually the height reached by the jet on images taken at different times, while for the blowout jet, where we have higher temporal resolution data, we used the images within the mask adopted for the temperature/density analysis (which lies along the direction of the propagating outflow) and placed them side by side for all available images. These "stacked" intensity images build up a space-time plot (see, e.g., Sakao et al., 2007) where the intensity fronts form bright strips whose slope (angular coefficient) gives the outflow speed value.

In the next Section we give the results of our analysis.

5.4 Results

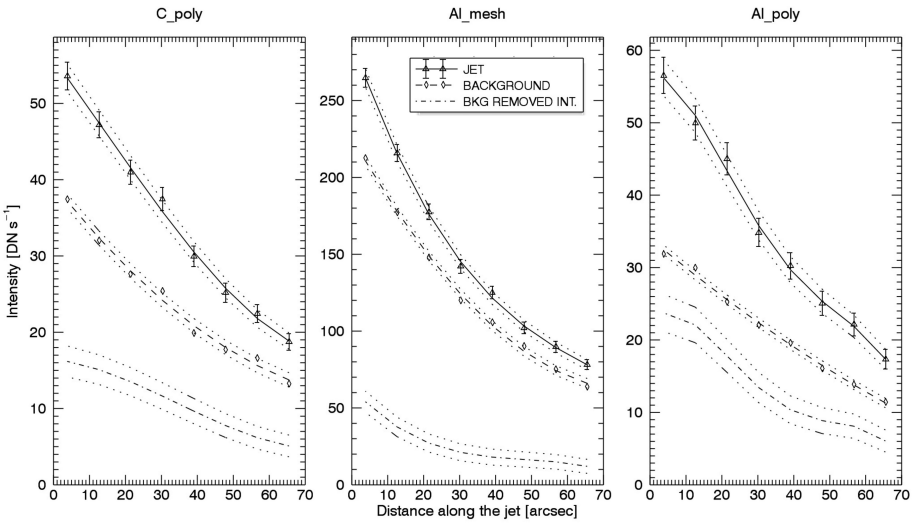

Figure 5.4 Measured values and fitted profiles of the intensity vs. distance: along the standard jet with background (solid line and triangles); in the background (dashed line and diamonds); and along the standard jet after removing the background contribution (dash-dotted line). Data are taken in the XRT *C_poly* (left panel), *Al_mesh* (middle panel) and *Al_poly* (right panel) filters at ≈ 22:51 UT for the jet profile, and at ≈ 22:30 UT for the background profile. Errors have been calculated following the Narukage et al. (2011) procedure. Dotted lines bound values of the fitted profile, plus and minus the 1σ statistical uncertainty.

5.4.1 The standard jet

Fig. 5.4 gives the profiles of the *C_poly*, *Al_mesh* and *Al_poly* filters intensities vs. distance along the jet at ≈ 22:51 UT; and in the background over the jet area at 22:30 UT, which was before the occurrence of the jet. Triangles and the error bars represent average intensities over the jet width with their statistical 1σ uncertainties, and the solid line is a fourth-order polynomial fit to the jet intensity data. Dotted lines bound values of the fitted profile, plus and minus the 1σ statistical uncertainties. Diamonds and the dashed line represent the background intensity and the polynomial fit to the data, while

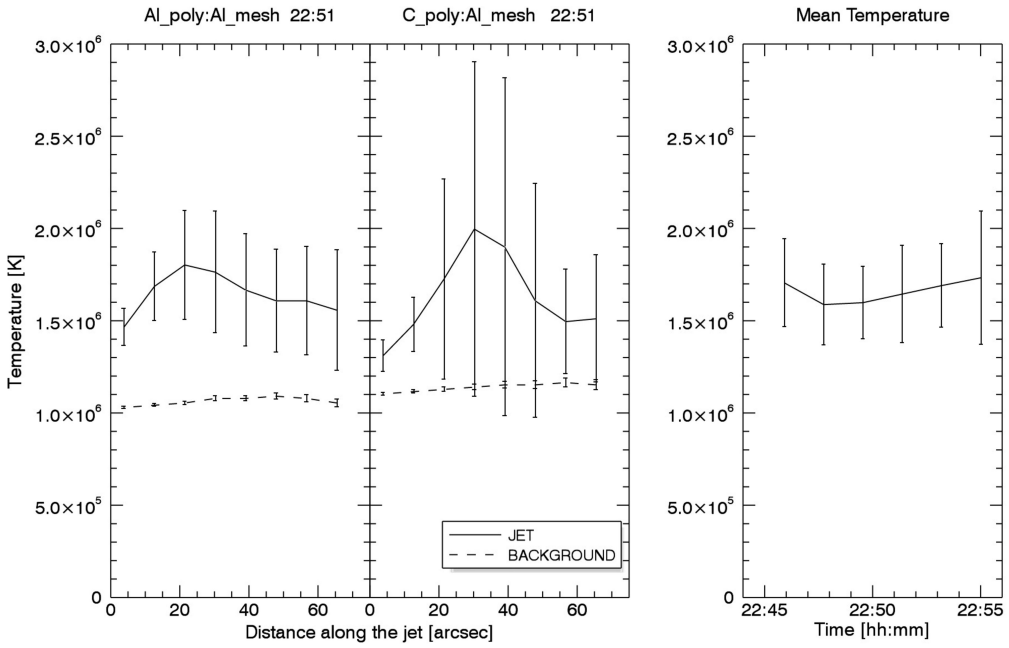

Figure 5.5 The plasma temperature versus distance-along-the-jet profile for the standard jet at 22:51 UT obtained from the ratio *Al_poly/Al_mesh* (left panel) and *C_poly/Al_mesh* (middle panel); distance is given in image pixels from the base of the jet. The dashed lines with (very small) error bars are the derived temperatures of the background corona. The right panel gives the profile of the temperature, averaged over the jet length, as a function of time (from the *Al_poly/Al_mesh* filter ratio).

the dash-dot line gives the jet intensity-vs.-distance profile after removal of the background.

As long as the lower dotted jet line lies above the upper dotted background line, i.e. as long as the jet intensity is higher than the background intensity by 2σ, temperatures inferred via the filter ratio technique are statistically significant.

Temperatures derived from these data are shown in Fig. 5.5 (left and middle panels), which gives the temperature vs. distance profile for the standard jet, derived, respectively, from the *Al_poly/Al_mesh* and *C_poly/Al_mesh* filter ratios. The black bars represent the temperature of the jet plasma with its statistical errors, while the dashed line is the temperature of the background material. Jet temperatures from the two filter ratios are consistent

within the error bars at about 1.5×10^6 K, suggesting agreement between the values of the mean temperature in the volume that has been integrated over.

The increase in the error bars of temperatures from the *C_poly/Al_mesh* ratio (middle panel) in pixels 25 to 50 arcsec distant from the jet base, is due to a sudden decrease in the slope of the ratio of the filter response functions for values measured at these positions; since the error is inversely proportional to the derivative of this ratio, the error increases noticeably (see eq. 15 of Narukage et al., 2011). Hence, temperatures inferred from the *Al_poly* over *Al_mesh* ratio are more reliable than those derived from the noisier *C_poly* to *Al_mesh* ratio, although being not inconsistent with each other. The right panel of the figure shows the profile of temperature vs. time, averaged over the whole jet length, from values obtained only from the more reliable ratio. Over the examined time interval temperatures appear to be constant. The background coronal temperature of $\approx 1.0 \times 10^6$ K agrees with e.g. the Doschek et al. (2010) polar coronal hole background value.

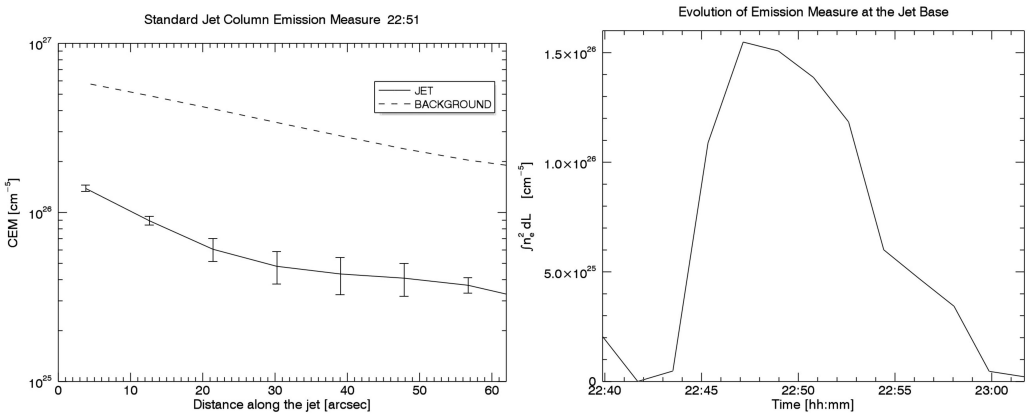

Figure 5.6 The Column Emission Measure (cm^{-5}) of the standard jet vs. distance along the jet axis (left panel), inferred from the ratio *Al_poly/Al_mesh* at $\approx$ 22:51 UT. The right panel shows the profile of the base EM vs. time over the lifetime of the jet.

The Column Emission Measure (CEM, cm^{-5}) has been inferred from Eq. 5.1; in Fig. 5.6 we show (left panel) the profiles of the CEM vs. distance along the jet, at 22:51 UT, inferred from the ratio *Al_poly/Al_mesh*. The solid line with error bars gives the CEM of the jet with 1σ uncertainties: errors have been calculated following the procedure worked out by Narukage et al. (2011) and, in particular, we used Eqs. 15 and 16 of their paper. The

dashed line shows the CEM for the background and foreground CH plasma.

The highest CEM turns out to be at the jet base, decaying steadily with distance from the base up to about 40 arcsec, where it stabilizes around values of 5×10^{25} cm^{-5}. The CEM of the background plasma is about one order of magnitude higher (6.5×10^{26} cm^{-5}) because of its longer LOS-integration path, compared with the thickness of the jet. Fig. 5.6 (right panel) shows that the CEM of the jet increases initially, reaching a maximum of about 2×10^{26} cm^{-5} at 22:49 UT, and later decreases accounting for the jet disappearance in the *Al_mesh* filter at $\approx$ 23:00 UT.

If we assume a cylindrical shape for the standard jet, we can estimate the jet width along the line of sight to be about 2×10^3 km, and obtain a density profile for the jet plasma both along the jet and in time. Densities n_e at the time of maximum jet brightness are $\approx 1 \times 10^9$ cm^{-3} at the jet base and half of this value 60 arcsec above the base. Similar values have been found by several authors (e.g. Culhane et al., 2007; Doschek et al., 2010), and Doschek et al. (2010) analogously found jet densities to fall as a function of height in the data sample they studied. Our density values eventually decrease in time, accounting for the jet disappearance.

The temperatures we found are slightly higher/lower than the temperatures inferred respectively by Nisticò et al. (2011) (0.8 to 1.3×10^6 K) and by Culhane et al. (2007) (2 to 3×10^6 K), and agree with the 1.4×10^6 K estimate of Doschek et al. (2010). Temperatures obtained by Madjarska (2011) of up to 12×10^6 K at the footpoints of a jet are not present in our data, as they would imply ratios a factor 2 to 3 higher than those we measure. Possibly the energy deposition site with such a high temperature is tiny and undetectable in limb observations because of the more extended LOS of limb events with respect to disk events. On the other hand, temperatures in Madjarska (2011) of outflowing plasmas ranging from 0.5 to 2×10^6 K are consistent with our results.

Because the jet is within the field of view of *STEREO A*, we made an extensive search for a signature of the event in EUVI, but, while the BP shows up in all four EUVI channels, we only identify a very weak jet-like structure above the flaring BP in the 195 and 284 wavebands, with too low a count rate to allow us to evaluate temperatures from those EUVI data. In order to check whether the weak emission of the EUVI jet is consistent with the XRT-inferred jet physical parameters, we used the latter to calculate the expected EUVI background/jet emission ratios at about 20 arcsec above the base of the jet, taking into account the EUVI filter responses. It turns out that the ratios are, in the 171, 195, 284 channels, respectively, $\geq$ 100, 3.6, and 2. Hence, while we obviously cannot expect to detect the jet in the 171 channel, we might expect the jet to be more clearly detectable in the

other channels. We ascribe the weakness of the EUVI jet to the different vantage point of *Hinode* and *STEREO A*, that results in a higher *STEREO* background that washes out most of the jet feature. As we will see in the next Section, something similar occurs in the blowout jet, whose components do not always appear in both *STEREO* spacecraft.

We also derived the outflow plasma speed ($(2.5 \pm 0.3) \times 10^2$ km s^{-1}) visually from the increase in time of the top of the jet. Obviously what we measure represents only the component of the speed normal to the line of sight, but because these events are within polar CHs, where the magnetic field is radial, we can assume that outflows are radially oriented.

So far, little information in the literature has been given about the spatial and temporal evolution of the jet parameters. Hence, we analyzed the variation of temperature vs. time and temperature vs. distance along the jet. Temperature does not decrease along the jet axis; this suggests that, at any given time, the jet intensity decreases with distance only because of a density decrease. This density decrease with distance could be due in part to a funneling out of the jet material into the outer solar atmosphere. The rightmost panel of Fig. 5.5 reveals that, at least over a time interval of about 10 minutes, the temperature of the jet remains about constant; over this time interval the jet appears to move laterally. This is not a real movement of the jet, rather, it shows that reconnection migrates sideways with time; that is, a sequence of jet strands brighten progressively at increasing distances from the first jet. Hence, a jet structure is maintained at a constant temperature by a shifting reconnection location that occurs progressively-shifting sideways with respect to the episode that initiated the jet, but the amount of plasma that is carried upwards changes with time. The lateral motion (meaning the apparent lateral motion of the jet, or the shifting motion of the reconnection point) occurs at a speed ≈ 7 km s^{-1}, this being the projected speed onto the plane of the sky. This value is in agreement with predictions from the Moreno-Insertis et al. (2008) model. The Pariat et al. (2009) model suggests the lateral shift to occur at a speed of one-fifth to one-tenth of the upward plasma speed along the jet axis; this would imply that projection effects lead us to underestimate the speed at which reconnection migrates laterally. Because the jet occurs in polar regions, we lack a magnetic field map that would allow us to make a more realistic estimate of the speed at which reconnection moves laterally and ascertain whether our lateral speed could take a higher value than we estimated.

The open question of whether the jet plasma escapes from the solar gravitational field can be addressed with the help of data from COR1, the coronagraph aboard the *STEREO* missions. However, we did not find any evidence of the jet in COR1 data.

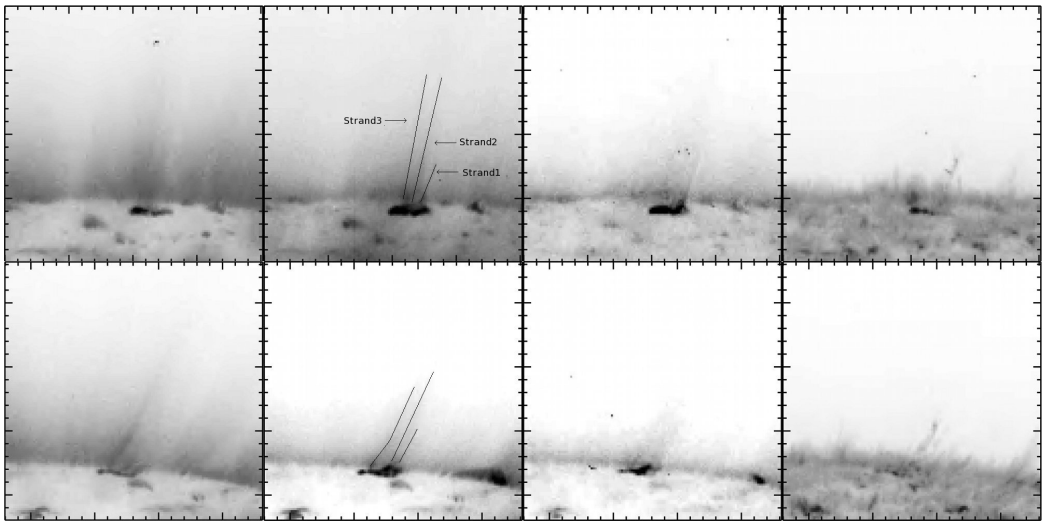

Figure 5.7 Images of the blowout jet of 2007 Nov 3, acquired by the EUVI telescopes onboard *STEREO A* (upper panels) and *STEREO B* (lower panels) at 12:06 UT in (from left to right) the 171, 195, 284, and 304 Å channels.

5.4.2 The blowout jet

Because *Hinode*/XRT acquired images of the blowout jet only in the *Al_poly* filter, we determined the jet temperature applying the filter ratio technique only to EUVI data. The jet area was imaged in all EUVI channels of *STEREO A* and *B*, as shown in Fig. 5.7. The upper and lower panels show simultaneous images of the blowout jet acquired at 12:06 UT, on Nov 3, 2007, by, respectively, *STEREO A* and *B*, in the 171 Å (left panel), 195 Å (middle-left panel), 284 Å (middle-right panel), and 304 Å (right panel) filters. The occurrence of the jet in the 304 Å channel is a key signature of blowout jets (Moore et al., 2010, 2013), and hints to the blowout eruption of the base arch.

The composite multi-strand structure of the blowout shows up clearly: in particular in the 195 Å images we identify 3 different strands, each of which reaches a different altitude. In the following we illustrate results from the temperature analysis of the three substructures of the jet, which we refer to as Strand1, Strand2, and Strand3, from right to left. We notice that the strands are not always visible in both spacecraft: for instance Strand3 does not show up in the 171 images of *STEREO A*, while it shows up clearly in *STEREO B* images. Because strands are not always seen by the two spacecraft, we cannot say whether different strands come in a variety of

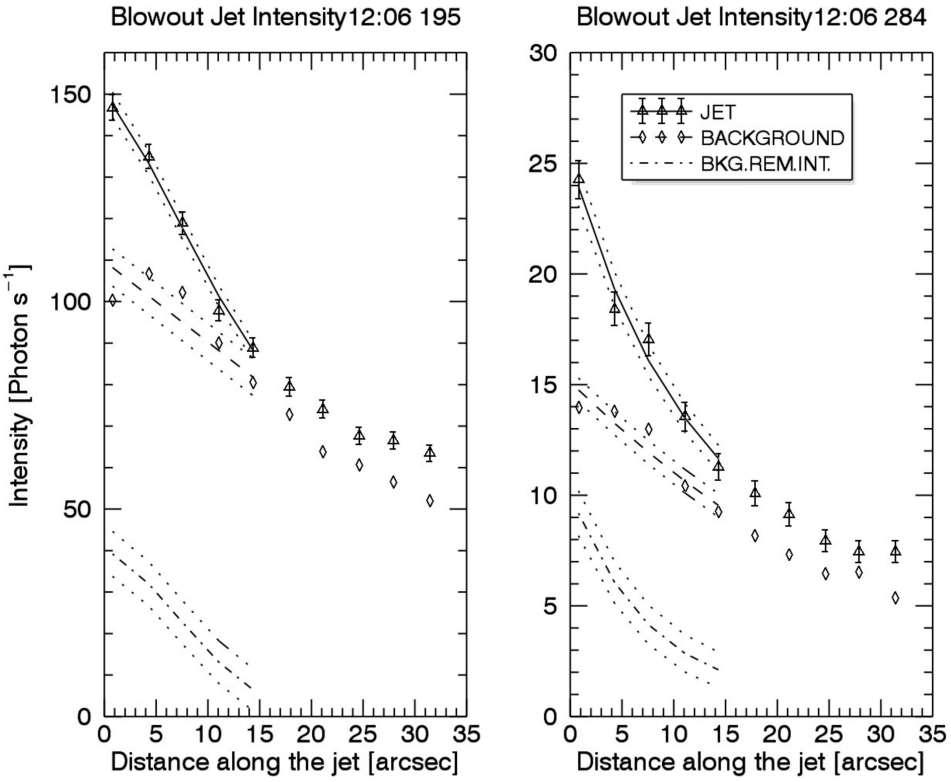

Figure 5.8 Profile of the intensity (photon s^{-1}) vs. distance along the axis of Strand1 of the blowout jet in the, 195 (left panel), and 284 Å (right panel) channels of EUVI A, at 12:06 UT on 2007 Nov 3. See Fig. 5.4 caption for other notations.

intensities and lengths or whether the differences we observe depend on the viewing angle or on the evolutionary stages jets go through over their lifetime that are randomly sampled in our images. We surmise that the background emission of the ambient corona, originating from different pathways in the two spacecraft, affects the visibility of the strands; we have already observed this for the standard jet.

Fig. 5.8 shows the intensity (photon s^{-1}) along the axis of Strand1 at 12:06 UT, as measured in the 195, and 284 Å channels of *STEREO A*/EUVI, with error bars. The background emission and the jet intensity after background subtraction are also shown. In the 171 Å channel, the jet emission does not exceed the background intensity: hence the 171 Å image is not shown and temperatures have been inferred via the 284/195 filter ratio only.

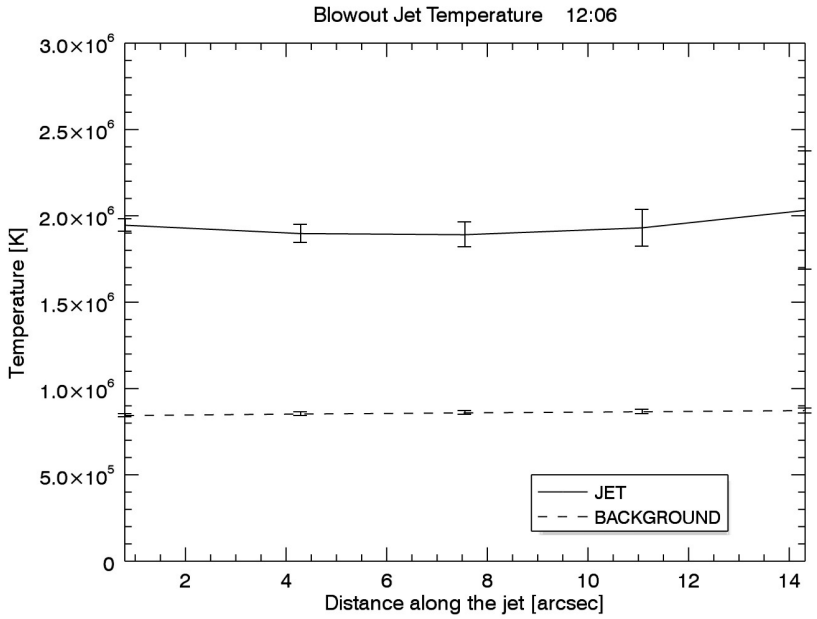

Figure 5.9 Temperature vs. distance profile for blowout jet Strand1, at 12:06 UT, from the 284/195 filter ratio calculated from data acquired by EUVI telescopes on *STEREO A*.

Fig. 5.9 gives the 284/195 temperature of Strand1, from data of the *STEREO A*/EUVI package.

The temperature profile is characterized by higher values than found in the standard jet, having values around 2×10^6 K. Because EUVI collects a higher number of photons than *Hinode*/XRT, the 1-σ error bars are smaller in these EUVI plots. Temperatures inferred from *STEREO B* range between 1.8 and 2×10^6 K, and are nearly constant over a height interval of ≈ 12 arcsec.

The CEM of Strand1 is shown in Fig. 5.10, and is quite similar to that of the standard jet: as for the standard jet, we point out that the background CEM is much higher than that of the jet. The densities inferred from the EM show an almost linear decay from the jet base to 15″ above the base, decreasing from 8×10^8 cm^{-3} to 3×10^8 to cm^{-3}. These values are slightly lower than those of the standard jet. These values however were obtained at a time (12:06 UT) that was one or two minutes prior to the probable maximum brightness in soft X-rays, based on the XRT data; whether the densities would have been higher at the time of maximum soft X-ray brightness is unclear.

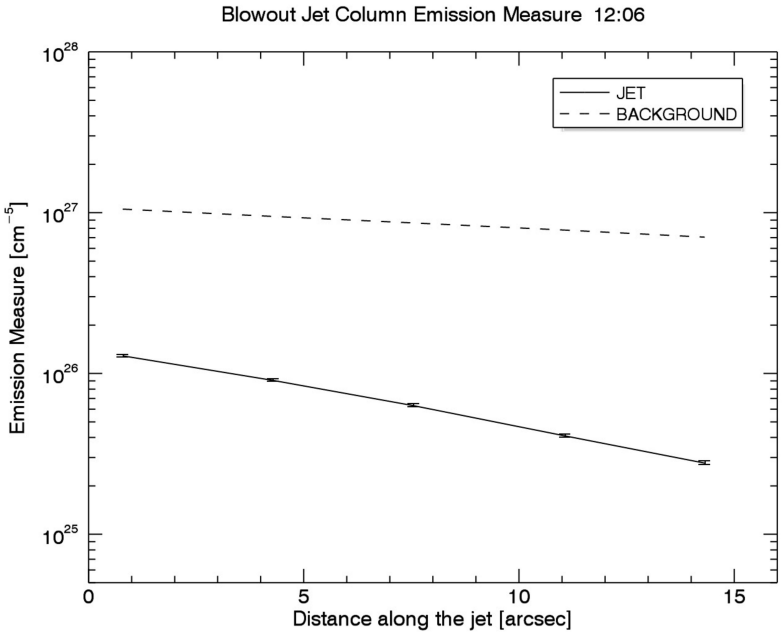

Figure 5.10 The Column Emission Measure for Strand1 of the blowout event, from temperatures inferred from the ratio 284/195. *STEREO A* data have been used, as in Figs. 5.8 and 5.9.

The same procedure, applied to *STEREO B* data, yields comparable density values, decreasing from 6×10^8 cm^{-3} to 2.8×10^8 cm^{-3}, over the same height interval (although we cannot establish an absolute scale for distances along the jet axis as seen by the two spacecraft). We examined also the other strands of the blowout: the temperatures of Strand2 and Strand3, independent of whether evaluated from *STEREO A* or *STEREO B* data, are 1.8 - 2 $\times 10^6$ K. In particular, Strand2, which can be followed over 60 arcsec, maintains a constant temperature throughout its length. Densities similarly are within the values reported above in Strand1.

As mentioned in Section 5.3, we used stacked intensity plots to obtain the outflow speed of blowout jet plasma from XRT *Al_poly* data, that have a time resolution of 40 s. It is easy to identify the three strands observed by *STEREO A* and *B* in XRT images, which provides a view from a vantage point in between the *STEREO* spacecraft. Fig. 5.11 gives the time-distance plot of Strand2, chosen because it has a longer duration than the other strands. Also, to enhance the visibility of the *Al_poly* intensity fronts an unsharp mask technique has been applied to the data. Dotted lines outline

the intensity-front trajectory along the jet axis. The shape of the intensity-fronts at lower altitudes shows that plasma accelerates from $\approx$ 100 to $\approx$ 350-400 km s^{-1} over the initial 1-2 minutes after jet initiation, reaching a higher speed than inferred for the standard jet. We point out that the high time cadence at which XRT images of the blowout have been acquired (40 s) would allow us to measure speed as high as $\approx$ 1000 km s^{-1}.

It is interesting to compare outflow speeds inferred from this technique with values inferred via a completely different method: Patsourakos et al. (2008) first made a 3D reconstruction of the trajectory of a jet they observed, and then computed the plasma outflow speed from the distance vs. time plot of the jet front. Those authors found that a phase about 30 minutes long where the jet rose at 10-20 km s^{-1}, is followed by an acceleration phase where the average outflow speed (over $\approx$ 2 minutes) is on the order of 90 km s^{-1} and rises subsequently to a speed of $\approx$ 300 km s^{-1}. The initially lower value, and the terminal speed of $\approx$ 300 km s^{-1} are consistent with those we found from stacking plots. In the view of Patsourakos et al. (2008), these speeds correspond to the untwisting of the flux tube followed by a nearly vertical rise. This scenario may as well apply to our observations.

Fig. 5.11 provides evidence for the occurrence of repeating jets, three to five of them in this case, that repeat at a time interval of $\approx$ 300 s. This behavior is not unusual: repetitive plasma outflows have been noted by Scullion et al. (2009) (although with a far different periodicity than we find here), while Morton et al. (2012) detected multiple bright ejections in time-distance plots from cross-cuts along/through a blowout jet and jet-related phenomena observed by SDO/AIA. SDO/AIA data have been used also by Liu et al. (2011) in their analysis of a standard-to-blowout jet where analogously no less than 10 plasma blobs streaming outward have been detected. Although the interpretation of these results is not easy, and further data are needed, it is likely that the observed phenomena point to repetitive reconnection events between closed and open field lines.

The data of the standard jet have a lower temporal resolution compared with the blowout jet data (110 s vs. 40 s). Anyway, the lower quality time-distance stack plot for the standard jet (not shown here) provides values of the outflow speed that are consistent with values obtained visually. Furthermore, this stack plot supports the occurrence of repetitive ejection episodes within the standard jet as well. The present analysis implies that this behavior may be shared by both the standard and the blowout jets.

As with the standard jet, we searched COR1 data for evidence of the blowout jet. Fig. 5.12 shows 4 frames of polarized brightness of the solar corona as observed by the COR1 instrument onboard the *STEREO B* mission. These are running difference images, smoothed to reduce the noise.

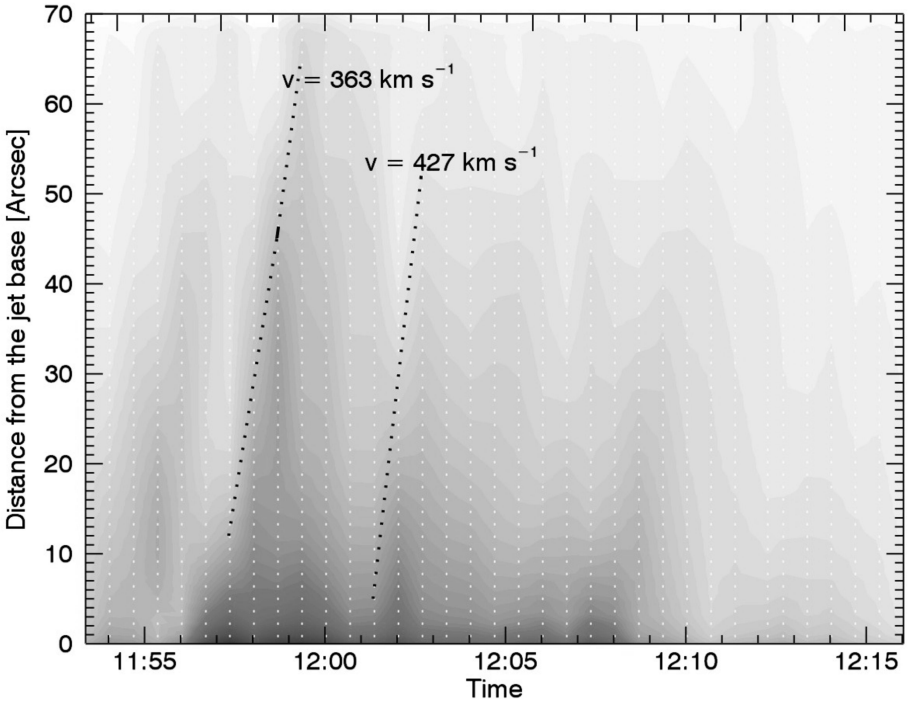

Figure 5.11 Stack plot for the Strand2 structure of the blowout jet. The superposed black dotted lines are trajectories of the jet intensity fronts. The inferred plasma outflow speed is also given. Vertical white dotted lines give the time individual frames have been acquired.

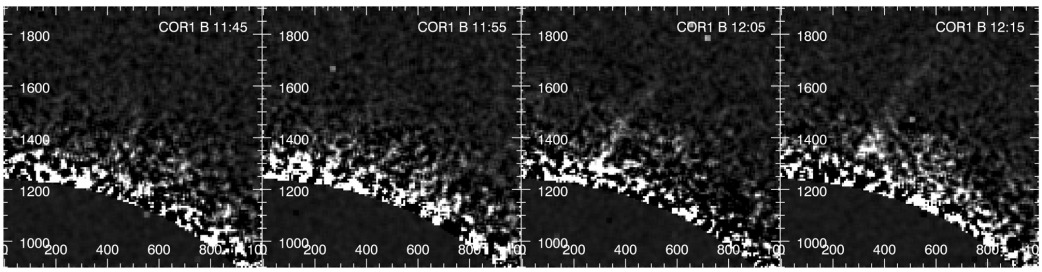

Figure 5.12 A sequence of running difference images from the COR1 coronagraph onboard the *STEREO B* satellite, showing the blowout jet reaching altitudes $\geq$ 1.4 solar radii.

The jet is clearly visible in the COR1 field of view reaching $1.8R_{sun}$ at 12:05 UT. This is consistent with an ejection that occurs at 11:55 UT and propagated upwards, accelerating beyond the 400 km s^{-1} we estimated from the XRT images and eventually overcoming the solar gravitational field to be fully ejected from the Sun.

5.5 Energy budget

In a scenario where jets originate because of a reconnection event triggered by flux emergence within an open ambient field, we may check whether standard/blowout jets imply any difference in the magnetic energy release that fueled them. In the following we try to estimate, although crudely, the energy components that contribute to the energy budget of the ejections. We assume reconnection to occur at the base of the jet, possibly slightly above the bright points base, at an altitude of order 5-10 arcsec, and assume that the magnetic energy is converted into kinetic, potential, work, wave (Alfvén) and radiative energy. We ignore conduction along field lines, as jets keep a constant temperature along their axis, and we ignore the fraction of energy that is dissipated downward with respect to the reconnection site (likely of the same order of magnitude as that released upwards).

Hence, the magnetic energy flux (F_{rec}, erg cm^{-2} s^{-1}) that is released, per event, is distributed between the enthalpy, F_{enth}; wave, F_w; kinetic, F_{kin}; potential, F_{pot} and radiative, F_{rad} energy fluxes:

$$F_{rec} = F_{enth} + F_w + F_{kin} + F_{pot} + F_{rad} \tag{5.3}$$

where

$$F_{enth} = \frac{\gamma}{\gamma - 1} pv \tag{5.4}$$

$$F_w = \sqrt{\frac{\rho}{4\pi}} \xi^2 B \tag{5.5}$$

$$F_{kin} = 1/2 \rho v^3 \tag{5.6}$$

$$F_{pot} = \rho g L v \tag{5.7}$$

$$F_{rad} = n_e n_H \chi T^{\alpha} L \tag{5.8}$$

where p, ρ, g, γ are, respectively, the plasma pressure, mass density, gravity, γ is the ratio of the specific heats ($\gamma = 5/3$), n_e is the plasma number density ($n_H = n_e$), ξ is the amplitude of unresolved non-thermal plasma motion, B is the field strength and L is the vertical extension of the jet. For F_{rad} we

Table 5.1. Physical parameters of the jets

	Standard jet	Blowout jet
T_e	1.6×10^6 K	$1.8 - 2 \times 10^6$ K
cem	8×10^{25} cm^{-5}	1×10^{26} cm^{-5}
n_e	6×10^8 cm^{-3}	6×10^8 cm^{-3}
B	2.8 G	4.5 G
v	250 km/s	400 km/s

adopted the analytic approximation and the values of α, χ given by Rosner et al. (1978) ($\alpha = 0$, $\chi = 10^{-34.94}$, with χT^α in W m^3)).

The wave energy flux is supposed to be due to waves generated at the time of reconnection when field lines change shape to relax to their final configuration. Evidence for Alfvénic waves in jets has been found by, e.g., Cirtain et al. (2007), who reported a physical displacement of the jet axis. Because we do not observe any recursive lateral shift of the jets that may hint to the wave amplitude, we make no hypothesis on the nature of excited waves and only assume that waves appear as unresolved plasma motions broadening spectral lines and that they propagate at the Alfvén speed. The wave amplitude ($\xi = 100$ km s^{-1}) is assumed to be the value given in Kim et al. (2007) who, from EIS data, found non-thermal velocities ranging from 57 to 106 km s^{-1} at the footpoints of jets. This is consistent also with Scullion et al. (2009) observations that pointed out that large jet outflows are associated with regions of high line broadening. As we do not have any information about differences in the wave flux in the two jet families, we assume F_w has the same value in the standard and blowout jet. For the field strength, B, we assume that outflows occur at approximately the local Alfvén speed, v_A ($v_A = B/\sqrt{4\pi\rho}$), and infer the magnetic field strength from this hypothesis. We point out that we likely underestimate the magnetic field strength as the bulk flows do not necessarily have the same Alfvénic speed as the small-scale reconnection flows that originate at the diffusion region. This assumption yields magnetic field strength of $\approx$ 2.8 G and 4.5 G for, respectively, the standard and the blowout event.

In Table 5.1 we show the values of the parameters we used for evaluating the energy fluxes of standard and blowout events; these are representative of what we measured over the duration and along the jets we analyzed. The magnetic field strength listed in the Table corresponds to the guess we made

about values in the reconnection region and not to the values of the field in the BP region where jets originate.

Because the kinetic energy flux depends strongly on the outflow speed, its value for the blowout jet ($\approx 3 \times 10^7$ erg cm^{-2} s^{-1}) is larger by about a factor 4 than that of the kinetic energy flux of standard events, while the blowout enthalpy flux ($\approx 1.7 \times 10^7$ erg cm^{-2} s^{-1}) is 1.6 times larger than the enthalpy flux in our standard jet. These are the forms of energy where most of the energy flux dissipates, while the other energy fluxes are about one order-of-magnitude lower (the radiative energy flux is negligible, the potential and wave energy fluxes are, in the standard vs. the blowout eruptions, respectively, 2.5×10^6 and 2.5×10^6 vs. 4×10^6 and 4×10^6 erg cm^{-2} s^{-1}).

Hence the energy released by reconnection is nearly three times as large in the blowout jet than in the standard jet. But if we take into account the multiple strands that show up in our blowout event, we can say that fueling a blowout requires 10 times a larger energy than needed to fuel our standard ejection. Altogether the energy that goes in a blowout jet is on the order of 2×10^{27} erg.

However, we neglected, so far, the cool component that appears in blowout jets and in our jet shows up in the COR1 images of Fig. 5.12. Indeed these jets are considered to be miniature versions of two-ribbon flares and although an estimate of the mass of the Coronal Mass Ejections (CME) associated with these events is still missing, a blowout CME has been recently observed by Shen et al. (2012), in SDO data, confirming that these ejections are the low energy representatives of this class of flares. Two ribbon flares are the most energetic flares: the global energetics of 38 eruptive events has been evaluated by Emslie et al. (2012), who concluded that most of the energy of these events resides in the kinetic energy of the associated CME (order of a few units times 10^{32} erg). Hence, it becomes mandatory to estimate the energy content of the CME associated with our blowout event. Although COR1 images reveal the cool component associated with the blowout we examine, we have no evidence of a CME, most likely because its size and/or density is too low to be revealed by STEREO or SOHO experiments and we have to resort to an indirect technique to make a guess of its mass.

Yashiro & Gopalswamy (2009) have reported on a statistical relationship between the X-ray fluence in the 1 to 8 Å band of solar flares and the kinetic energy of the CME associated with the flare. Drake et al. (2013) applied this relationship to ejections from active stars, possibly brighter than the Sun by a factor of order 1000, assuming the relationship to hold over a wide range of CME and flares. Here we make the same assumption and extrapolate the Yashiro & Gopalswamy (2009) relationship to smaller events, known, as we said, to be the small-scale analogs of large events.

The X-ray emission of blowout jets can be estimated from their physical parameters, typical size and lifetime and turns out to be slightly lower than 10^{26} erg, two to three order of magnitudes lower than the X-ray emission of the flares examined by Yashiro & Gopalswamy (2009). Adopting the fit to their data given by Drake et al. (2013) in their Fig. 1, it turns out that the mass of the CMEs associated to weakly X-ray emitting flares is on the order of 10^{12} g, that is on the order of 1/1000 of the average mass of CMEs. This compares well with the mass of CMEs given in the LASCO catalog, where smallest events have a mass of about 10^{13} g and accounts for their lack of visibility in the SOHO/LASCO coronagraphs.

Once the mass of the CME associated with our jet is know, we can estimate their kinetic and potential energy, which turn out to be on the order of 10^{27} erg. Hence, adding the energy residing in the cool component to the hot component energy of the blowout, results in a total energy of the order of 10^{27} to 10^{28} erg, making their total energy budget larger by about a factor 20-30 than that of standard events. Hence blowouts are typically 10^5 times less energetics than the largest solar eruptions, known to emit about 10^{32-33} erg.

We notice that the overall energy released by reconnection over our jets' lifetimes does not entirely go into feeding the ejections, as the jets are rooted in BPs whose intensity increases noticeably over the duration of the jets. This is especially true in the blowout event, where a large area undergoes a major brightness increase. This points to an even larger energy release in blowout jets than we estimated above on the basis of impulsive ejections only.

The estimates we give are obviously a crude approximation to the more rigorous estimates that might be given if, for instance, waves would be detected, CMEs observed, magnetic field measured and outflow speeds more accurately evaluated. When dealing with such small ejections, we are at present in the situation we have been for years in large flares, whose energy budget, as we mentioned, is only recently being correctly calculated (Emslie et al., 2012). However, we deem it interesting to have an even rough assessment of the jets energy budget to be used by modelers and theoreticians as an observational reference. The most uncertain term in the estimate of the energy budget is the wave term F_w: for instance, the magnetic field B may be higher than we estimated, resulting in a higher wave flux. Also, we may have mistakenly used the Alfvén speed calculating F_w. However, it is unlikely that the error we make is higher than a factor 3-4, which will leave our conclusions practically unchanged. Another source of uncertainties may reside in the wave amplitude estimate and in the evaluation of the outflowing plasma speed from the stacking plots, which are not easily interpreted. In

their analysis of a polar jet observed by the SDO/AIA assembly, Shen et al. (2012) give a total estimate of the jet energy on the order of 2×10^{29} erg. This value is consistent with the value given here, if we consider that Shen et al. (2012) arbitrarily assume the electron density to be 4×10^9 cm^{-3}, nearly one order of magnitude larger than the electron density of our events. We notice, however, that these authors deal with a jet that falls back to the Sun and thus the properties of their event may not be the same as those of the jet analyzed in this work.

5.6 Summary and conclusions

In this work we aimed at inferring differences in the physical parameters of two solar X-ray jets, one each from two previously-identified families of coronal hole X-ray jets, standard jets and blowout jets. Apart from the multi-components that characterize the blowout jet, our analysis has shown that, with respect to our standard jet, our blowout jet has: 1), possibly an electron temperature higher by $10\% - 20\%$ (although the difference in the temperature of the two jets is marginally above the statistical error and further analysis is required to resolve this issue), and, 2), an outflow speed higher by $\approx$ a factor 1.6. We note in passing that temperatures and densities we inferred are in agreement with predictions from a model by Pariat et al. (2009), which give temperatures of 1.7×10^6 K and densities of 2×10^{-16} g cm^{-3}. Also, we found, 3), that the energy dissipated by reconnection that fuels the blowout jet is about one order of magnitude larger than the energy that feeds our standard jet.

On the basis of our sample of one object from each category, these properties suggest that blowout jets, rather than standard jets, originate from the stronger magnetic field regions within coronal holes. This might suggest that jets that escape into the heliosphere are likely to belong to the blowout category, in agreement with results from our COR1 analysis (although we cannot rule out the possibility that standard jets as well escape into the heliosphere, but do not have a high enough emission measure to be detected). Should this be the case, we nevertheless have shown in Pucci et al. (2013) that the contribution of these jets to the solar wind mass loading is likely to be negligible. The same can be said as to the energy they feed to the corona, which is about a factor 10^4 smaller than that required to maintain the corona and solar wind. If blowout jets are accompanied by other features, such as type II spicules as suggested by Moore et al. (2010) and Sterling et al. (2010), these figures may possibly change, but an analysis of this scenario is beyond the scope of the present analysis.

The stack plot of the blowout (Fig. 5.11) jet reveals the occurrence of multiple reconnection events. We find the same behavior from the visual analysis of the standard event: both plots indicate the occurrence of multiple reconnection episodes. This is confirmed also by the BP where jets originate whose brightness undergoes significant enhancements associated with each jet episode: variations of the BP intensities have been observed by, e.g., Chandrashekhar et al. (2013), who also interpreted these as being generated by repeated reconnection episodes. Hence, while there is little doubt that what dictates the observed changes in BPs and generates the jets is reconnection, it is hard to say whether the stacking plots of standard and blowout have a unique interpretation. In blowout jets we know that reconnection occurs at different places within the BP; hence the repeated blobs we image in individual strands may be indicative of bursty reconnection and be analogous to blobs observed in current sheet identified in large CME events (see, e.g., Lin et al., 2005; Schettino et al., 2009; Riley et al., 2007). In this case, the stack plot of individual blowout jet strands would be consistent with, e.g., time-dependent Petschek reconnection (Priest & Forbes, 2000) occurring in the current sheet associated with these ejections. This interpretation is especially appealing, as it is believed that blowouts are miniature representations of large CMEs (see, e.g., Liu et al., 2011). On the other hand, the drift of standard jets and associated stack plots would be indicative of a reconnection region migrating to different flux surfaces, as implied in, e.g., Pariat et al. (2009) model.

Chapter 6

Birth, Life, and Death of a Solar Coronal Plume

6.1 Introduction

Solar plumes are best visible when they exist in polar regions: indeed they have long been observed at the time of eclipses, when they trace the open field lines rooted in the unipolar magnetic field of polar coronal holes (CHs). The advent of space instrumentation enormously extended our capabilities for observing plumes and provided us with a large amount of previously unavailable data about their behavior in UV radiation. These objects are interesting not only *per se*, but also because their role in solar wind is still controversial (e.g.: do they supply wind mass?). It is also uncertain whether they can be identified in the solar wind (e.g., how far do they maintain their identity in the extended corona?).

Before being able to answer these questions, we need to have better knowledge of the behavior of plumes; their generation, disappearance, lifetime, and temporal evolution of their physical parameters, are, as of today, not fully defined. In this work we focus on a single plume, one that we follow from birth to death over its nearly two-day lifetime. We aim at measuring the plume's temperature, density and outflow speed (if any) and at analyzing the evolution with time of these quantities; such time variations have not yet been discussed.

Our analysis is based on observations made by the *Atmospheric Imaging Assembly* (Lemen et al., 2012, AIA) on board the *Solar Dynamic Observatory* (Pesnell et al., 2012, SDO), over 28 and 29 August 2010. The plume is rooted in the northern CH, close to the pole of the Sun, and is visible in most AIA channels, although at differing phases of its life and with differing contrast

with respect to the background corona. It originates in a Bright Point (BP), whose radiance changes with time. In the past many plume-BP combinations have been observed (see, e.g., Del Zanna et al., 2003; Wang & Muglach, 2008); we provide further information on this issue by describing the relationship between our plume and its associated BP.

CHs are known to be sources of the high speed wind, and, with plumes being the densest regions within CHs, a seemingly reasonable assumption is that they are sources of (most of) the wind mass. In the past, authors obtained conflicting results on this issue, with some claiming plumes are quasi-static, and others claiming they may contribute significantly to the solar wind (see Table 2 of Wilhelm et al., 2011, for a compendium of different results). Most of these studies adopted the Doppler Dimming technique to obtain the speed of plasma in the intermediate corona, while the most recent investigations focussed on revealing the occurrence of outflows in plumes at lower heights in the corona (McIntosh et al., 2010; Krishna Prasad et al., 2011; Tian et al., 2011), by using space-time plots of UV radiance from data acquired by the *Solar Terrestrial Relation Observatory* (STEREO) and SDO experiments. Here we used AIA data to build space-time plots in different AIA channels and check whether the outflow speed of the propagating disturbances is a function of temperature. We also built space-time plots at a few times during the plume lifetime, looking for time evolution of the observed upflowing events as the plume fades.

Several authors inferred the electron temperature ($T_{\rm e}$) and density ($n_{\rm e}$) of plumes from either Emission Measure(EM), Differential Emission Measure (DEM), or line ratio analyses. It turns out that $T_{\rm e}$ and $n_{\rm e}$ in plumes are, respectively, slightly lower and higher than their values in the ambient corona (see Tables 3 and 4 of Wilhelm et al., 2011, for a summary of past results). A few authors have given also the profile of $T_{\rm e}$ and $n_{\rm e}$ vs. heliocentric distance over a limited range of altitudes. No information however is available about the behavior of these quantities over the plume lifetime. Because AIA observations in multiple spectral bands are available, here we adopt DEM technique that allows us to follow the changes of the physical parameters of the plume material as it evolves over time. As we describe in section 6.4, the plume turns out not to be strictly isothermal, and it is its density rather than its temperature that decreases as the plume decays.

In section 6.2 we describe the data set we analyze and the BP-plume relationship; sections 6.3 and 6.4 illustrate as functions of time the behavior, respectively, of the outflow speed and of the electron temperature and density of the plume; and in section 6.5 we summarize our results and give a crude estimate of the mass possibly provided to the solar wind by plumes.

6.2 The data and the BP-plume relationship

The data we analyze were acquired by the SDO AIA experiment over two days, from 00 UTC on 28 August, to 24 UTC on 29 August 2010. AIA takes full-disk images of the Sun, with a time cadence of 12 s, in 10 UV and EUV wavelengths, with a plate scale of 0.6″ per pixel. In the following we use data acquired in the 94 Å, 131 Å, 171 Å, 193 Å, 211 Å, 193 Å, 304 Å and 335 Å EUV channels.

We chose a region near the solar north pole within a small CH, where BPs and plumes are rooted. Although stable in size, the CH covers a small area, north of 70° latitude. The adjacent quiet sun emission may extend to high altitudes and show up as a diffuse haziness beyond the limb of the sun. This little affects the plume analysis (because, as described in section 6.4, for each image we subtract the ambient background component from the total observed emission), but may lead to an overestimate of the temperature or density of the interplume background.

Figure 6.1 gives images of the BP and plume, obtained by summing data over a 10 min accumulation time, in the 171 Å, 193 Å, and 211 Å channels, on 28 August, from 08:40 to 08:50 UTC and from 19:58 to 20:08 UTC (respectively, top and middle row) and on 29 August, from 06:00 to 06:10 UTC (bottom row), with an exposure time of 100 s in the 171 Å channel, and of 145 s in the other channels.

The dashed and dotted lines in the A panel give the position and size of the horizontal "slits" adopted to evaluate the evolution in space and time of the BP and the plume that appear in Fig. 6.2 and Fig. 6.3. The dashed boxes in the D panel give the position and size of the vertical "slits" adopted to build the space-time plots, given in Figs. 6.4, 6.5 and 6.6. The dashed box in the G panel gives the position and size of the vertical "slit" adopted to build the space-time plot, given in Fig. 6.7.

In CH regions we expect (O'Dwyer et al., 2010) the 171 Å channel to be dominated by the Fe IX 171.07 Å line (with a temperature of maximum ion abundance $T_e = 0.7 \times 10^6$ K), while the 193 Å channel maximum response is over 0.7×10^6 K$\leq T_e \leq 1.6 \times 10^6$ K. The 211 Å channel emission arises from Fe X and Fe XI lines, with maximum response at, respectively, $T_e = 1.1 \times 10^6$ K and $T_e = 1.4 \times 10^6$ K (and add to Cr IX emission, with a maximum response at $T_e = 0.9 \times 10^6$ K). Hence in Fig. 6.1 the 193 Å and 211 Å images show hotter plasma than that imaged by the 171 Å channel. Fig. 6.1 reveals that the plume plasma is cooler than the ambient corona, while loops bridging over bipoles forming the BP at the base of the plume are hotter than the plume.

The evolution of the plume and the BP over their entire lifetimes is shown,

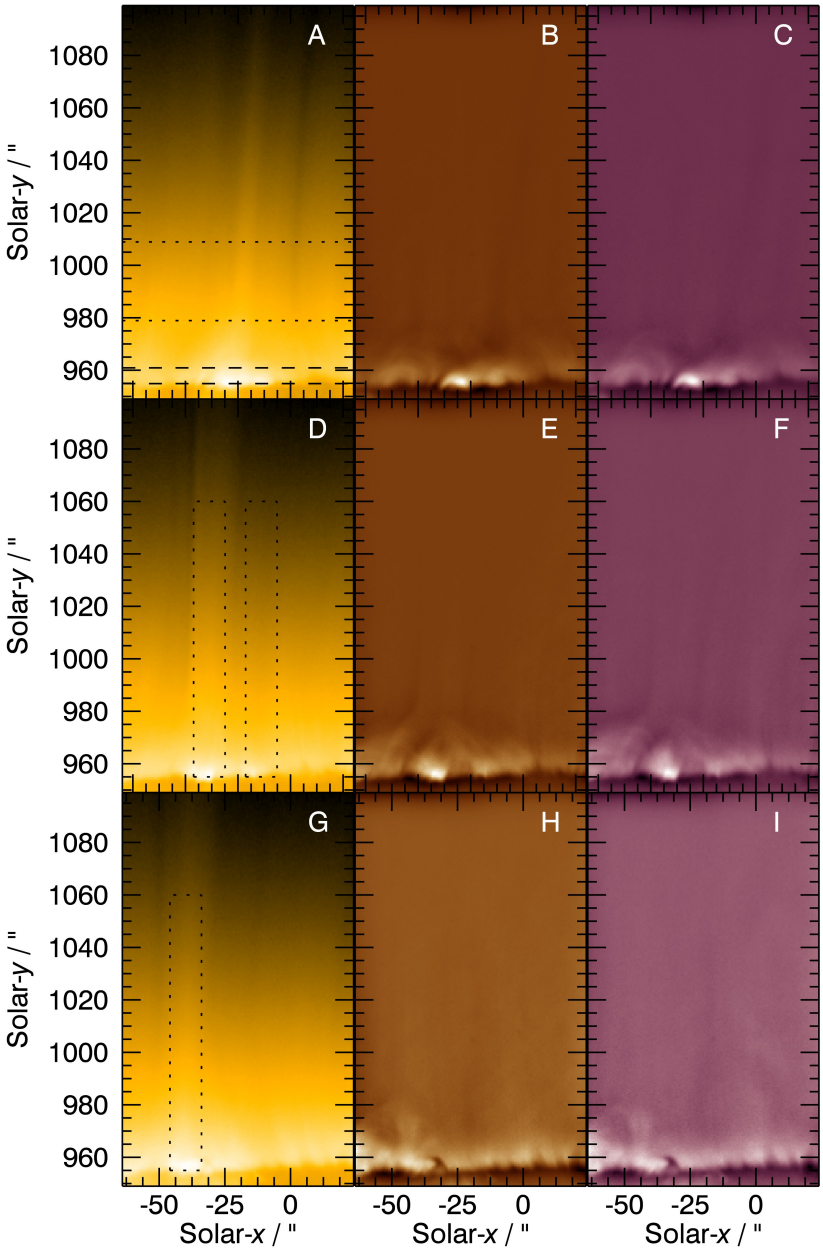

Figure 6.1 Images of the BP plume complex, in the 171 Å (left panels), 193 Å (middle panels) and 211 Å (right panels) AIA channels, from data accumulated over 10 min, i.e. fifty images for each panel. Top row (A, B, C panels) shows data from the early phase of the plume (08:40 UTC, on 28 August), while middle and bottom rows show respectively data from the peak phase (19:58 UTC on 28 August) and decaying phase (06:00 UTC on 29 August). We adopted a logarithmic scale for the colors in the 171 Å panels, to enhance the visibility of the plume at high altitudes. An unsharp mask has been used in the 193 Å and 211 Å filter images for a better display of the loops at the base of the plume. For further details see text.

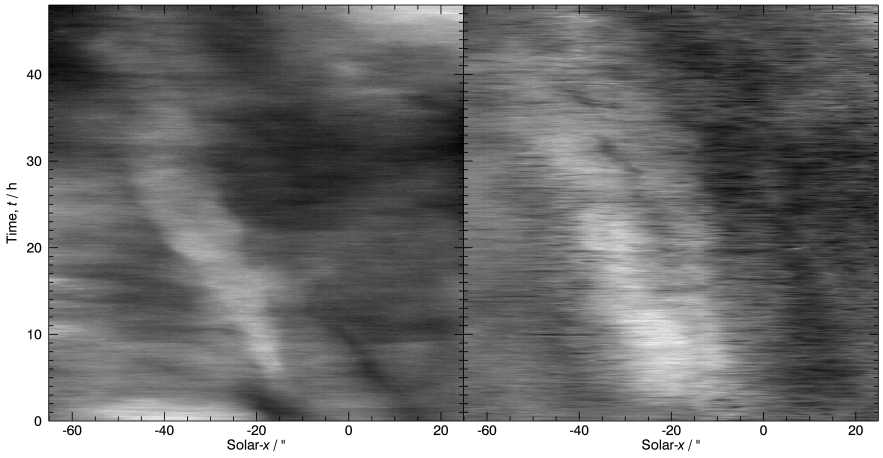

Figure 6.2 Left panel: Radiance in the AIA 171 Å channel at the location of the plume, shown against time and solar-x. Data in this plot were accumulated over an altitude interval of 30″ (between the two upper short-dashed lines in panel A of Fig. 6.1), and sampled every 120 s, over a time interval from 00:00 UTC on 28 August, to 00:00 UTC on 30 August. Right panel: Radiance in the AIA 171 Å channel at the location of the Bright Point (BP) where the plume is rooted, shown against time (y-axis) and position (x-axis). Data in this plot were accumulated over an altitude interval of 6″ (between the two lower long-dashed lines in panel A of Fig. 6.1), and sampled every 120 s, over a time interval from 00:00 UTC on 28 August, to 00:00 UTC on 30 August.

respectively in the left (plume) and right (BP) panels of figure 6.2.

These profiles have been constructed by examining plasma within virtual horizontal slits (dashed parallel lines in panel A of Fig. 6.1), that cut through the BP and/or the plume, and plotting the 171 Å channel radiance within the slit at different times. We used data accumulated over an altitude interval of 6″ for the BP and of 30″ for the plume, with a cadence of 120 s. Clearly both features are carried around the Sun by solar rotation, and the resulting longitudinal shift agrees with values given by Gupta et al. (2012) for the rotation rate at high latitudes. The west-east shift of the BP-plume complex reveals that the plume is rooted on the far side of the Sun: hence we don't know whether we see the whole, or only a fraction, of the BP total area.

The right panel of Fig. 6.2 suggests that the BP first appears at ≈ 02:00 UTC on 28 August and its radiance maximizes at ≈ 8:30 UTC. It steadily

decreases afterwards, until it dies a little before 12 UTC on 29 August. The plume first appears at ≈ 04:00 UTC on 28 August, and blends with the background from ≈ 12 UTC onward on 28 August. Hence, there is no plume before the BP emergence, but the plume survives the BP, although for a short time.

We also examined the 304 Å channel data, looking for jets that might occur before the birth of the plume: usually this channel samples relatively cold chromospheric plasma. Indeed, a blowout jet lasting from 01:35 to 02:00 UTC is clearly visible in the 304 Å data, and, although briefly and less conspicuously, in the 171 Å channel. Hence, ≈ 2 h before the plume shows up, a precursor jet occurs, consistent with the Raouafi et al. (2008) results. At later times, however, we no longer used the 304 Å channel, since for this study we chose to focus on the hotter plume emissions.

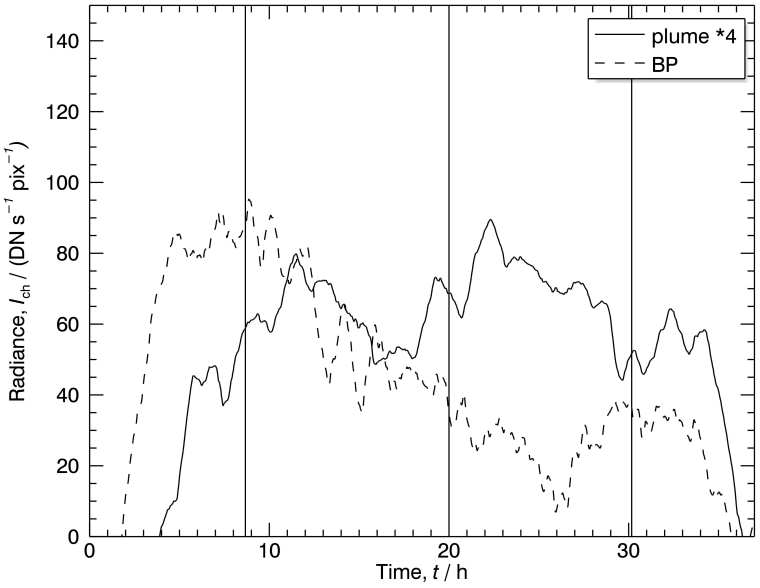

Figure 6.3 Background-removed Radiance of the BP (dashed line) and of the plume (solid line) in the 171 Å channel, measured every 120 s over the whole lifetime of the BP-plume complex. (The plume radiances are multiplied by a factor of four for clarity.) The plume and BP regions were defined in the same way as in Fig. 6.2 (i.e., using the upper- and lower-pair of dashed lines in Fig. 6.1A). Vertical lines give the times when plume data have been analyzed. See text for details.

A more direct view of the BP-plume relationship than given by Fig. 6.2 is shown in Fig. 6.3; there we give the background-subtracted radiances of the BP and the plume, in the 171 Å channel, over the lifetime of both features. The figure has been constructed from data taken every 2 min and smoothed with a running average boxcar of 40 min.

As in Fig. 6.2 data for the BP have been accumulated over the height interval between solar-y = 955″and solar-y = 961″ (i.e. 10 pixels), while plume data have been accumulated over the height interval between solar-y = 979″ and solar-y = 1009″ (50 pixels). At any time the horizontal "box" is centered at the same position for both structures and keeps a constant size, although shifting in time to follow the eastward-moving solar rotation of both structures.

Over its lifetime the BP shows brightenings and/or weakenings. The plume radiance, however, fluctuates less than the BP radiance; although initially brightening as the BP brightens, at later times the plume appears to be little affected by the BP's changes. Thus for this case it appears as if the BP is a prerequisite for the formation (and persistence) of the plume. But at later times the plume is apparently not sensitive to phenomena that modify the BP, other than dying shortly after the BP fades.

Radiance oscillations in BPs have been detected by many authors (see, e.g. Kariyappa & Varghese, 2008; Chandrashekhar et al., 2013) who claim they occur over a large variety of time scales (from minutes to hours) and are possibly periodic (with periods of the order ranging from 10 to 25 min). It is beyond the scope of this work to investigate the nature of the fluctuations here, nor, on the basis of this single case, can we draw any conclusions on the general BP-plume relationship. However, relative brightenings (order of 3 % of the time-averaged local plume emission) are characteristic aspects of plumes. Hence we conclude that, in this case, the occurrence of a BP seems to be necessary to create the conditions for the plume to develop, but the process leading to the BP is not the only factor that fuels the plume, because plume fluctuations are small compared to BP fluctuations. Indeed, as suggested by Zhang et al. (2012), only the strongest BP flashes, which we do not observe, may be associated with jets and cause plume brightenings.

6.3 Outflows in plumes

Outflows in plumes have been studied by a few authors (see, e.g. Gabriel et al., 2003; Teriaca et al., 2003) via the Doppler Dimming technique (Noci et al., 1987), applied to observations made by the *UltraViolet Coronograph and Spectrometer* (UVCS) on board the *Solar and Heliospheric Observatory*

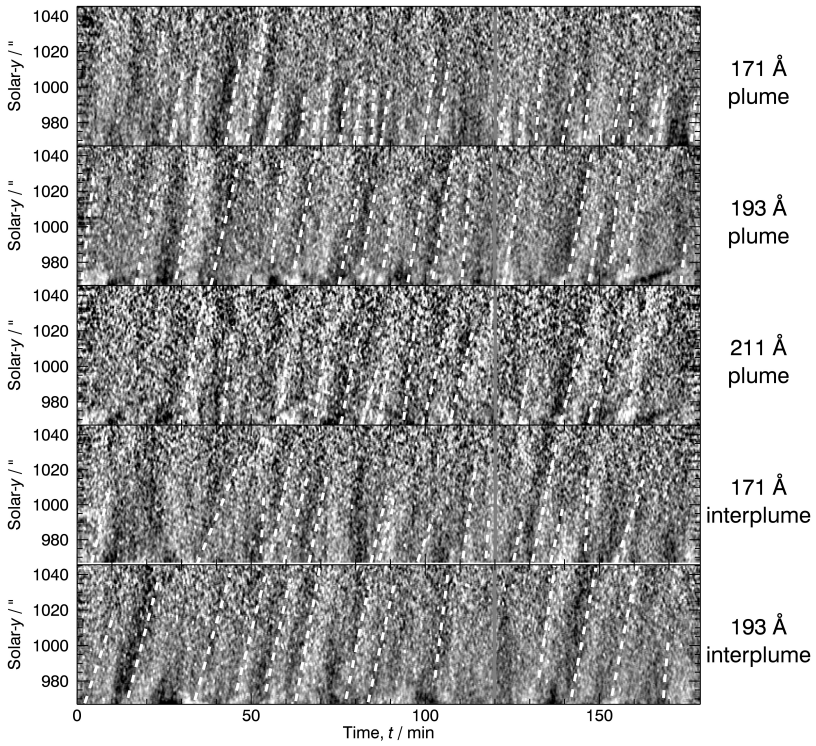

Figure 6.4 Space-time plot of the detrended radiances of the plume in the 171 Å, 193 Å and 211 Å channels (topmost 3 panels), over the time interval from 19:00 to 22:00 UTC on 28 August 2010. The ordinate gives the solar-$y/''$ and the abscissa gives time (t/min) after 19:00 UTC, on 28 August 2010. Plume data have been accumulated over the left vertical virtual slit shown in panel D of Fig. 6.1. Bottom 2 panels: same as the top two panels, in the background interplume corona. Background data have been accumulated over the right vertical virtual slit shown in panel D of Fig. 6.1. The white dashed lines have been added to help the reader trace upflowing events. The boxcar used in the detrending procedure is 75 images (15 min) wide; see text for further details.

(SOHO) at altitudes on the order of 1.4 to 2.4 solar radii.

At lower altitudes, data acquired in CHs by the SOHO *Solar Ultraviolet Measurement of Emitted Radiation* (SUMER) and/or the *Hinode EUV Imaging Spectrometer* (EIS) have been analyzed for spectroscopic signatures of upflows (see, e.g. Wilhelm et al., 2000; Tian et al., 2010); these works

provide information on the sites where the solar wind originates, but add little information on its outflow speed profile. At altitudes ranging from 100″ to 150″ above the limb of the Sun, several authors (McIntosh et al., 2010; Tian et al., 2011; Krishna Prasad et al., 2011; Gupta et al., 2012) adopted a different technique to analyze data, using space-time plots of propagating outflows. Although upflow signatures have been detected both in plumes and interplume ambient plasma, the nature of these signatures is still debated, as it is not clear whether they are due to waves or whether they represent outflowing material (McIntosh et al., 2010). McIntosh et al. (2010), for instance, from data taken by the *Extreme Ultraviolet Imaging* (EUVI) package on board STEREO, suggested that high speed outflowing jets, with a mean speed on the order of 135 km s^{-1}, might repeatedly occur in plumes. These authors built time series of detrended images, along a virtual slit set normal to the limb of the Sun. We adopt the same technique to analyze our data.

Fig. 6.4 shows space-time plots of the plume radiance in the 171 Å, 193 Å and 211 Å AIA channels (top 3 panels) and of the interplume radiance in the 171 Å and 193 Å AIA channels (bottom 2 panels), over 3 h, from 19:00 to 22:00 UTC on 28 August. The panels cover an altitude interval of 80″; the bottom level has been set to a solar-$y = 965''$. The width of the virtual slit is 12″ (20 pixels) and is centered, in the plume case, at solar-$x = -31''$ and, for the ambient background corona at solar-$x = -11''$. Figure 6.4 displays "detrended" residual radiances as functions of time, following the procedure of Tian et al. (2011): after forming initial space-time plots over the virtual slits, we subtracted off 15 min (i.e., 75 images) running boxcar averages from the initial space-time plots, and then normalized to the running average. Compared to the initial space-time plots, these detrended space-time plots improve the visibility of fainter moving features. We do not show the space-time plot of the background corona in the 211 Å AIA channel, because it is too noisy (the 211 Å channel has a lower signal to noise ratio than the 171 Å and 193 Å channels).

The result in figure 6.4 shows alternating oblique dark and bright strips that extend upwards over time; these represent plasma flows, and the larger the inclination of the strip with respect to the time (horizontal) axis, the higher the speed. The relative radiance fluctuations are low level, being on the order of a few percent. Many flows are apparent over the plotted time span; all of these flows are from the slit regions, but our spatial resolution in the x-direction is dictated by the 12″ width of the virtual slit. To help the reader visualize the upflowing events and, at least qualitatively, their speed, dashed lines have been overplotted onto propagating disturbances. These lines trace the position of the highest radiance gradient: for "thin" (in the time dimension) outflows, the line overlays the event; for "wide" outflows,

the line has been drawn to the left of the event. Clearly, both the plume and interplume panels host a variety of different outflow speeds.

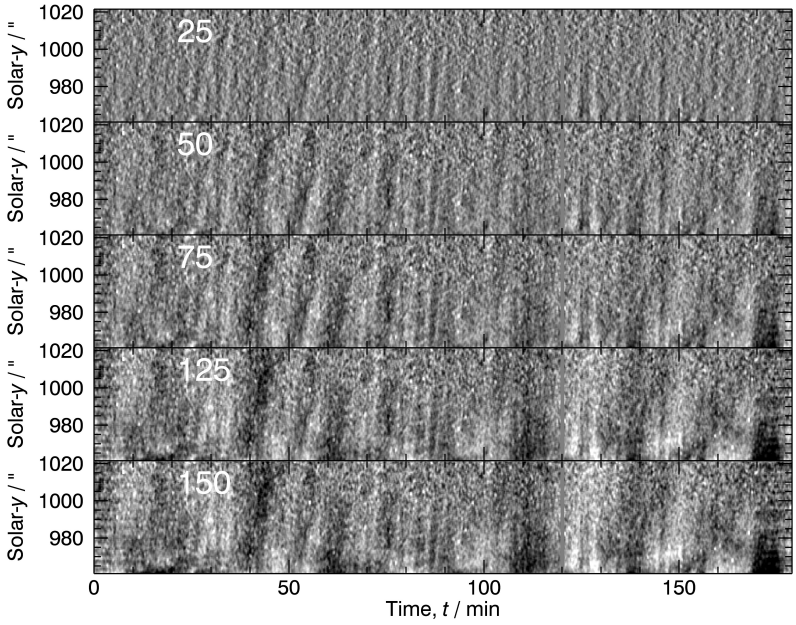

Figure 6.5 Space-time plot of the detrended radiance of the plume in the 171 Å AIA channel, over the same time interval used in Fig. 6.4 on 28 August 2010, when the plume was brightest. Otherwise the same as the upper panel of Fig. 6.4, except that the detrending procedure has been done using boxcars of widths span times ranging from 5 min (top panel) to 30 min (bottom panel) (i.e. from 25 to 150 images).

Before discussing the results of Fig. 6.4, we check whether the choice of the width of the boxcar in the detrending procedure affects the visibility of the events. Fig. 6.5 shows space-time plots of the AIA 171 Å radiance, over the same time interval used in Fig. 6.4, built from boxcar widths ranging from 25 to 150 images, i.e. from 5 to 30 min. It turns out that long duration events, such as that occurring at $t = (42 \text{ to } 50)$ min, may go unnoticed when narrow boxcars are adopted; this is because the wider the boxcar, the greater the radiance of long events. On the contrary, the isolated, thinnest (briefest) events, such as that at $t = 80$ min, when wider boxcars are used, tend to blend within the wide "events" that show up when large size boxcars are adopted. We conclude that outflowing episodes can be detected independent of the width of the boxcar, although the longest events are better identified

with wider boxcars and short duration outflows are more easily spotted with narrower boxcars.

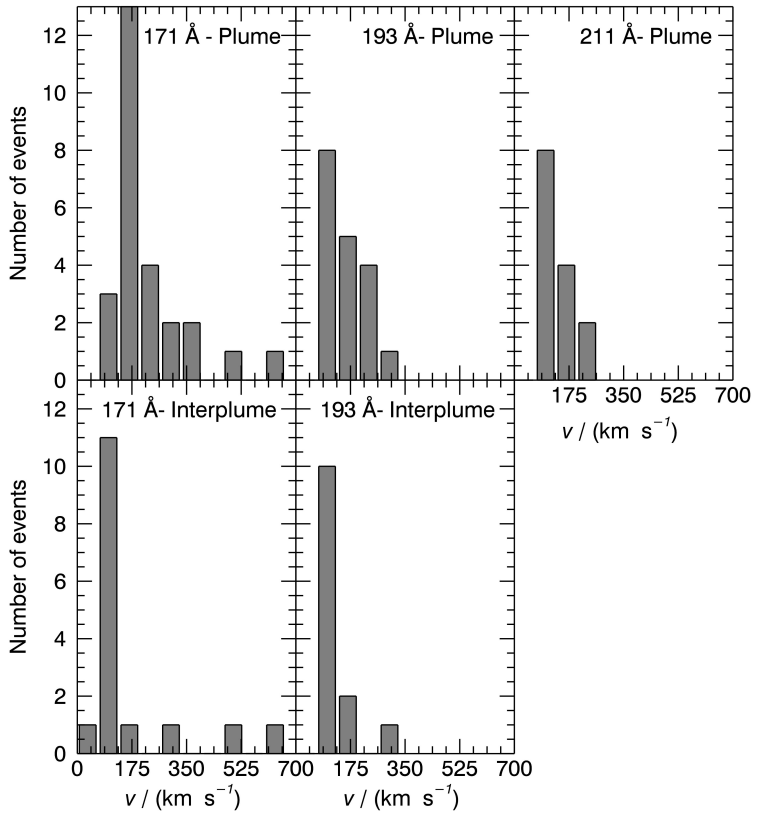

Figure 6.6 Histograms showing outflow-speed (v/ km s^{-1}) distributions of outflowing events in the plume (top row) and interplume background (bottom row) corona, in the 171 Å, 193 Å, 211 Å AIA channels for the plume, and in the 171 Å and 193 Å channels for the interplume background corona, on 28 August 2010, inferred from the data shown in Fig. 6.4. Boxcar width: 75 images.

Going back to Fig. 6.4, we point out that, in the 171 Å channel, the plume hosts a larger number of events (26) than the background interplume ambient corona (16). The speed distributions of the upflows are shown in Fig. 6.6, both for the plume (top row) and the background (bottom row). The histograms have a bin size of 66 km s^{-1}: In the 171 Å channel, the plume distribution peaks at $v \approx 167$ km s^{-1}, with a median value of 185 km s^{-1}, while in the interplume ambient corona the distribution peaks at $v \approx 100$ km s^{-1}, with a median value of 110 km s^{-1}. Hence, the plume upflowing

disturbances are more numerous and have a higher speed than disturbances in the ambient corona.

Fig. 6.7 gives the space-time distribution over a 2 h interval (05:00 to 07:00) UTC on 29 August at a time close to the final stage of the plume. Alternating bright/dark strips are still visible, with an upflow speed possibly even higher than that observed at earlier times; the distribution of upflowing events peaks at $v \approx 167$ km s^{-1}, but the median value is now ≈ 258 km s^{-1}. The event rate, however, is about the same as we detected during the earlier time period, being 8/h here compared to 8.7/h in the initial stage of the plume's life in Fig. 6.6. We conclude that the time series analysis of images taken at different stages in the plume's evolution reveals that the upflowing disturbances are seen throughout the plume lifetime, without major changes, either in their frequency of occurrence, or in the peak of their outflow propagation speed distributions.

We now examine whether the occurrence of outflows depends on temperature, i.e. on their observation in different AIA channels. To this end, we compare space-time plots in the 171 Å, 193 Å and 211 Å AIA channels. Fig. 6.4 shows that outflows occur in all channels, although not necessarily at the same time, nor with the same width (i.e. time duration). For instance, the 171 Å upflow at $t = 50$ min is missing in the 193 Å, channel emission. On the other hand, a 193 Å upflow at $t = 110$ min is missing in the 171 Å channel. The altitude reached by the bright strips before becoming too noisy to be identified is not relevant for our current investigations, because the apparent fading of the trajectories may depend on instrumental factors rather than on the physics of the events.

The middle and right panels of Fig. 6.6 give the distribution of the outflow speed in the 193 Å and 211 Å AIA channels. It turns out that the peak and median values of the 171 Å disturbances ($v \approx 167$ km s^{-1} and 185 km s^{-1}) are higher than those from the 193 Å and 211 Å channel distributions. The latter share the same value of the peak ($v \approx 100$ km s^{-1}), and the median value of the two distributions is quite similar (143 km s^{-1} and 124 km s^{-1}, respectively, for the 193 Å and 211 Å channel). Often the speed of outflowing events has been compared with the sound speed, $C_s/(\text{ m s}^{-1}) = 152\ (T_e/\text{K})^{1/2}$ (Priest, 1984), to ascertain whether the observed disturbances might be interpreted in terms of slow magnetosonic waves propagating upwards. In this case, we expect a temperature dependence of the outflow speed which is not observed in our data, as disturbances in the 171 Å channel propagate at a higher speed than disturbances in the "hotter" 193 Å and 211 Å channels. We will come back to this issue in section 6.5.

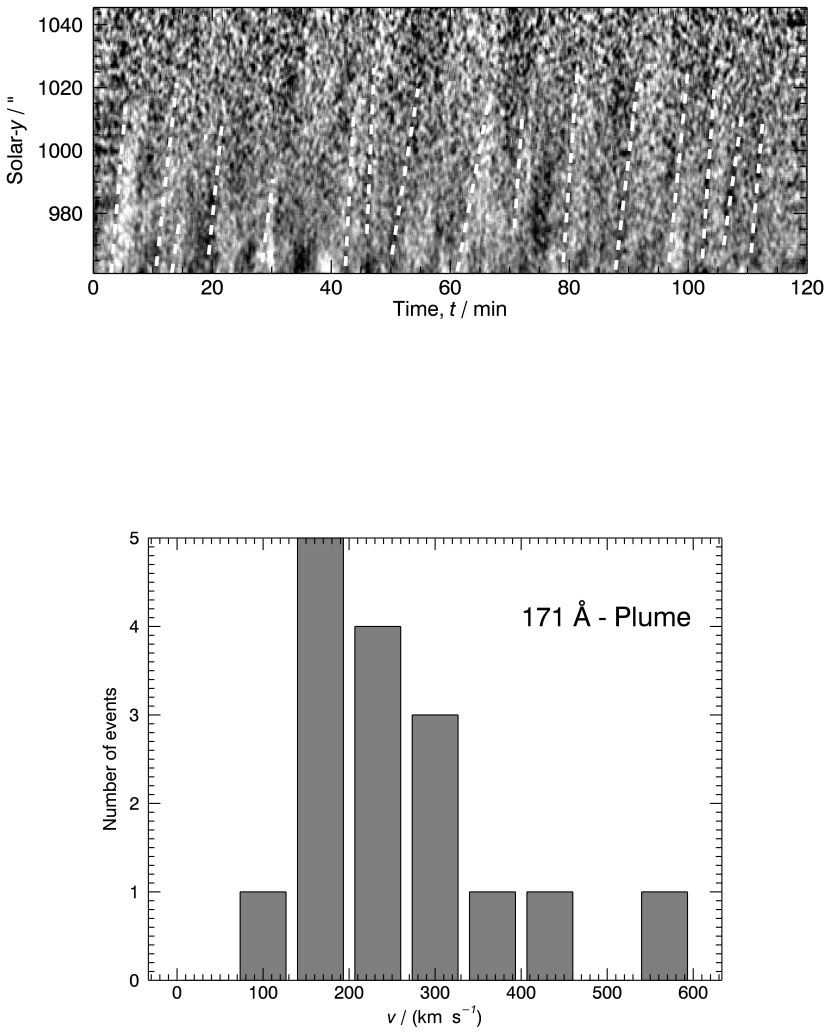

Figure 6.7 Top panel: Space-time plot of the detrended 171 Å radiance of the plume region on 29 August 2010, in the 171 Å over the 2 h time interval 05:00 UTC - 07:00 UTC; this time period is during the final stage of the plume's life. Boxcar width used was 75 images. White dashed lines trace upflowing events. Bottom panel: histogram showing the upflow speed distribution of outflowing events, over the same time interval as the upper panel.

6.4 Electron density and Temperature in Plumes

If plumes were strictly isothermal, the ratio of the emission in two different AIA channels would give their temperature, provided that the plasma sampled by the two AIA filters originates from the same regions and that ionization equilibrium holds. In that case the measured radiances, $I_{\rm ch}$ (data number per second per pixel), depend on the filter responses, $F_{\rm ch}$, which in turn are a function of temperature, $T_{\rm e}$ (and also on the elemental abundances), as show by the following relationship:

$$I_{\rm ch} = \int F_{\rm ch}(T_{\rm e}) n_{\rm e}^2 {\rm d}l \tag{6.1}$$

where $n_{\rm e}$ is the plasma density and where the integral extends along the line-of-sight (LOS) path. The capability of using data from many AIA channels leads to a more precise evaluation of $T_{\rm e}$, as all the ratios should converge to a unique temperature value. However, taking into consideration the results from section 6.3, where we found evidence for the occurrence of upflows of differing temperatures, we are lead to dismiss the hypothesis of isothermal plumes. So instead of the above isothermal-assumption formulation, we will use a different technique to evaluate the electron temperature and density.

To this end we rewrite Eq. 6.1 in a slightly different way,

$$I_{\rm ch} = \int F_{\rm ch} \epsilon(T_{\rm e}) {\rm d}T_{\rm e}, \tag{6.2}$$

where $\int \epsilon(T_{\rm e}){\rm d}T_{\rm e} = \int n_{\rm e}^2 {\rm d}l$ and $\epsilon(T_{\rm e}) = \frac{n_{\rm e}^2 {\rm d}l}{{\rm d}T_{\rm e}}$ is the DEM. This alternative formulation allows us to evaluate the amount of plasma at different temperatures within the plume. There are several algorithms to infer the $\epsilon(T_{\rm e})$ as a function of $T_{\rm e}$ distribution from observed radiances; here we adopt the technique recently developed by Plowman et al. (2013), that allows a fast reconstruction of $\epsilon(T_{\rm e})$ distributions and has been tested on AIA (and EIS) data. We refer the reader to Plowman et al. (2013) for details on their method. The AIA $F_{\rm ch}$ functions have been determined by combining the wavelength-dependent instrumental response with the emissivity model given by the CHIANTI 7.1 version, with the empirical corrections to the 94 and 131 Å channels suggested by Boerner et al. (2014).

In order to evaluate the physical parameters of plumes, we have to take into account that plumes are embedded in an ambient medium, the background corona; this background is multi-thermal as well, and often only slightly fainter than the plumes. The residual emission of the plume, which in principle can be determined by subtracting the background emission from

the LOS-integrated radiance, is hard to determine in practice. This is especially true when, for example, the background radiance changes across the width of the plume, or when using data from channels where the emission of the plumes is only marginally higher than that of the background. Hence, in order to deal with count rates high enough to minimize the statistical uncertainty of the data used in the $\epsilon(T_e)$ calculation, we chose instead to work with the integrated plume+background radiance at the plume location, and to evaluate the background emission at positions devoid of plumes.

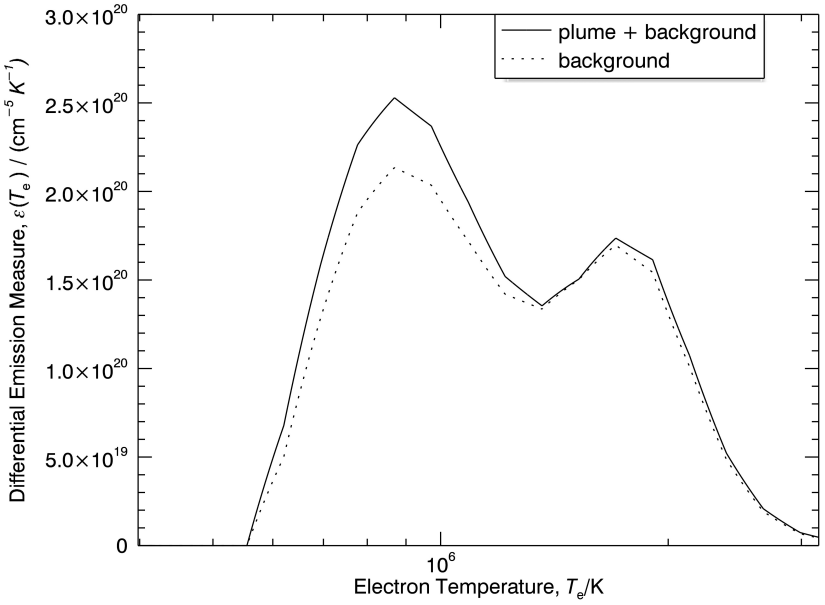

Figure 6.8 Differential Emission Measure, $\epsilon(T_e)$, vs. Electron Temperature, T_e, over the time interval from 19:58 UTC to 20:08 UTC on 28 August 2010, from the 94 Å, 131 Å, 171 Å, 193 Å, 211 Å, 335 Å channels. The solid line gives the $\epsilon(T_e)$ of the LOS-integrated emission along the axis of the plume (i.e. it is the plume+background $\epsilon(T_e)$) at a solar-$y = 1003''$. The dotted line gives the $\epsilon(T_e)$ profile in a region devoid of plumes (i.e. it is the background $\epsilon(T_e)$) at the same solar-y. The Emission Measure of the plume+background and of the background plasma can be evaluated by integrating $\epsilon(T_e)$ over dT and turn out to be, respectively, 3.0×10^{26} cm^{-5} and 2.7×10^{26} cm^{-5}.

Fig. 6.8 shows the $\epsilon(T_e)$ vs. T_e profiles of the LOS-integrated emission, at a solar-$y = 1003''$ along the axis of the plume (solid line), and at a position devoid of plumes (dotted line). The difference between these two curves

therefore represents the $\epsilon(T_e)$ vs. T_e profile of the plume itself. Here, the original data, acquired on 28 August 2010, have been integrated over the 10 min interval from 19:58 to 20:58 UTC, when the plume reached its peak radiance. The figure shows that the $\epsilon(T_e)$ of the plume+background is slightly higher than the background $\epsilon(T_e)$ in the regime 0.7×10^6 K $\leq T_e \leq 1.1\times10^6$ K, but above $T_e = 1.1 \times 10^6$ K all of the emission originates in the background. Integrating over temperature, we obtain an EM of the plume+background of 3.0×10^{26} cm^{-5}, which is higher by only 10 % over the background EM of 2.7×10^{26} cm^{-5}.

We checked the validity of our approach by selecting a region, within our dataset, at a time where the background and the plume+background were clearly identifiable, and worked with the background and the residual (background-subtracted) plume radiance to build separate $\epsilon(T_e)$ vs. T_e profiles for the background and for the plume. It turns out that the $DEMs$ evaluated by the two methods agree within a few percent.

Fig. 6.8 also shows that the background $\epsilon(T_e)$ profile is composed of two components, respectively peaking at T_e values of 0.9×10^6 K and 1.8×10^6 K. Taking into account the widths of the two distributions (assumed to be Gaussians centered at the peak values of T_e/K), it turns out that the background corona is at an average temperature of 1.2×10^6 K, a value on the high side of the coronal electron temperatures listed by Wilhelm et al. (2011). From the residual plume emission, we analogously infer an average plume temperature of 8.5×10^5 K, consistent with plume temperatures given by Wilhelm et al. (2011). It is beyond the scope of this work to discuss in detail the coronal temperatures. We do however remark that the value we obtained refers to an area within a small coronal hole (possibly affected by the projection of high structures) where local differences between background regions are apparent: it is obvious from the images in Fig. 6.1 that the radiance of the background corona either side of the plume is not the same. In figure 6.9 we show the evolution with solar-y, along the axis of the plume, of the plume $\epsilon(T_e)$ vs. T_e profiles (obtained from the difference between the plume+background and the background $\epsilon(T_e)$ curves, as described above), over the height range from solar-y = 979″ to solar-y = 1015″, at 08:40 and 19:58 UTC on 28 August, that represent the initial and peak stage in the plume evolution. Data have been accumulated over 10 min; the figure gives profiles at four values of solar-y (979″, 991″, 1003″, 1015″). This shows that the highest values in the $\epsilon(T_e)$ vs. T_e profiles occur at $\approx T_e$ = (6 to 8) $\times10^5$ K , possibly with a small shift towards lower temperatures with increasing solar-y. The slight asymmetry in the profiles of the $\epsilon(T_e)$ vs. T_e plots may be due to a partially unsuccessful removal of the background, with its contribution having not been fully subtracted from the plume emission; we cannot however rule out the possi-

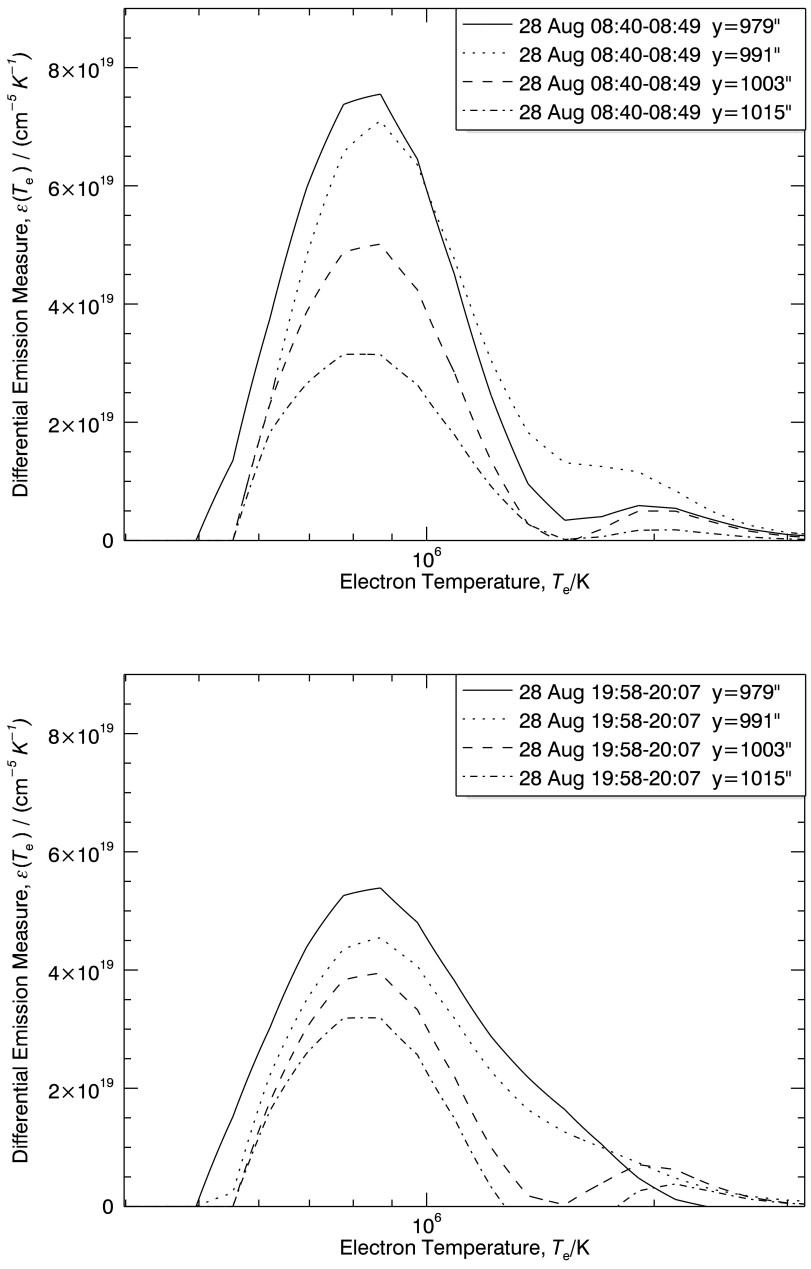

Figure 6.9 Differential Emission Measure, $\epsilon(T_{\rm e})$, vs. Electron Temperature, $T_{\rm e}$, at solar-y = 979″, 991″, 1003″, and 1015″, along the axis of the plume (respectively solid, dotted, dashed, dot-dashed lines) at two representative times of the plume's life. Left panel: profile at 08:40 UTC on 28 August 2010, during the initial stage of the plume's life. Right panel: profile at 19:58 UTC on 28 August, during the brightest stage of the plume's life. The background $\epsilon(T_{\rm e})$ profile has been subtracted from the plume+background $\epsilon(T_{\rm e})$ profile before plotting the plume $\epsilon(T_{\rm e})$ profile.

Solar-$y/''$	979	991	1003	1015
Time (UTC)	Plume electron density, n_e/cm^{-3}			
28 aug 08:40	3.1×10^8	3.2×10^8	2.4×10^8	1.9×10^8
28 aug 19:58	1.8×10^8	1.7×10^8	1.4×10^8	1.1×10^8
29 aug 06:00	1.7×10^8	1.3×10^8	1.1×10^8	9.3×10^7
Time (UTC)	Background electron density, n_e/cm^{-3}			
28 aug 08:40	1.1×10^8	1.0×10^8	9.2×10^7	8.3×10^7
28 aug 19:58	1.1×10^8	9.8×10^7	8.8×10^7	8.0×10^7
29 aug 06:00	1.1×10^8	9.9×10^7	8.9×10^7	8.1×10^7

Table 6.1 Density of the plume plasma.

bility of a tiny amount of plasma at high temperature within the plume. The plume plasma, while not being strictly isothermal, changes its temperature by only a factor ≤ 1.5 within the plume at each solar-y. For instance if we approximate with a Gaussian the profile at solar-$y = 1003''$ (dashed curve in the left panel of figure 6.9), we evaluate that ≈ 68 % of the plasma has temperatures between 6.5×10^5 K $\leq T_e \leq 1.1 \times 10^6$ K. Densities calculated from EMs (see Table 6.1), taking into account the increasing width vs. solar-y of the plume, turn out to decrease over a solar-y interval of $\approx 40''$ by ≈ 50 % to 60 %, independent of time. These densities decrease with time over the life of the plume by an amount that changes with solar-y, ranging from a factor of about 60 % at the lower solar-y ($979''$and $991''$), to about a factor 2 at the highest solar-y ($1015''$) we sample. Over the entire lifetime of the plume, its density is highest at its birth.

Figure 6.10 gives the $\epsilon(T_e)$ vs. T_e profiles at solar-$y = 979''$ and $1003''$ along the plume's axis, at times representative of the initial (08:40 UTC, 28 August), peak (19:58 UTC, 28 August), and decay (06:00 UTC, 29 August) phase of the plume. Data have been accumulated over 10 min starting at these times, and all AIA channels listed in section 6.2, with the exception of the 304 Å channel, have been used.

Table 6.1 shows a resume of our results: densities at different heights and times in the plume are compared with the ambient coronal densities at the same altitude and same time. In order to estimate densities in the background corona we assumed a LOS length of 0.5 solar radii.

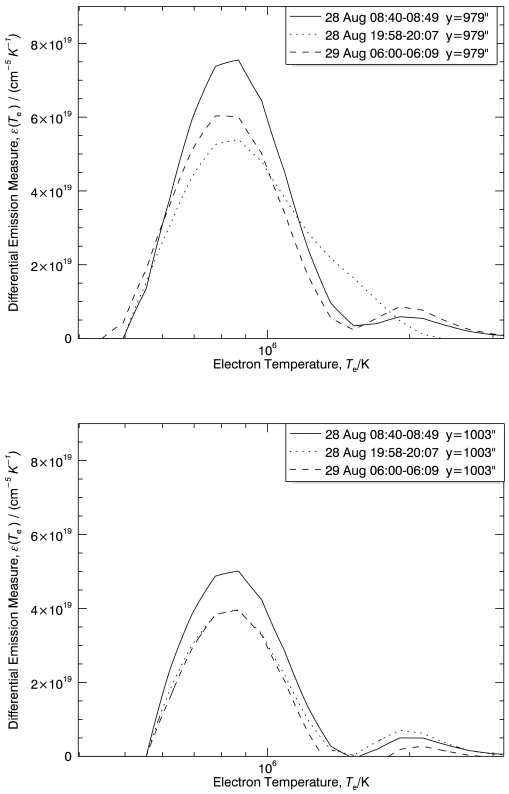

Figure 6.10 Time evolution of Differential Emission Measure, $\epsilon(T_{\rm e})$, vs. Electron Temperature, $T_{\rm e}$, along the axis of the plume, after subtracting the background $\epsilon(T_{\rm e})$. Left: at solar-y = 979″, at the initial (solid line), peak (dashed line) and final (dotted line) stage of the life of the plume. Right: same as left, but at solar-y = 1003″.

6.5 Discussion and conclusions

We have examined the behavior of a plume at several stages over its lifetime with the aim of clarifying its time evolution. In this section, we discuss separately the results we obtained for the three main areas we examined: the BP-plume relationship, outflows, and plume physical parameters.

6.5.1 The BP-plume relationship

The plume is rooted in a polar BP; the plume appears just after the BP appears, and disappears shortly after the BP disappears.

Del Zanna et al. (2003) suggested that for at least some cases, plumes have BPs at their bases only during the early stages of the plumes' lives. Our observations for this plume instead show the plume to have a BP at its base for essentially the entirety of the plume's life. Here we have examined only one case, and so obviously and we cannot draw general conclusions. We do emphasize however that long-lasting data are required to define the characteristics of the BP-plume association. In our case, we agree with Del Zanna et al. (2003) in that BPs may be a prerequisite of plumes, but we cannot say that the association holds only in the first stages of the plume lifetime, because in our case the BP lives for nearly the entirety of the plume's life, with the BP starting two hours before the plume starts, and the plume fading one hour after the BP fades (see Fig. 6.3).

Fig. 6.2 shows that the plume is brightest early in its lifetime; as it evolves in time the plume becomes fainter and wider, finally blending with the inter-plume medium. The temperature of the plume does not change with time, but its density decreases. Hence the visibility of the plume depends crucially on its density. Over the plume's lifetime the density changes by less than a factor of 2 at the lowest altitude. At higher altitudes, solar-$y = 979''$ and above, the density decreases by ≈ 2, implying a decrease of at least a factor 4 in plume XUV emission. Comparing the plume and background densities Table 6.1 shows that, early in the plume's life, densities along the plume's axis are about a factor 3 higher than those of the ambient corona at solar-$y = 979''$and $991''$, and a factor 2.5 higher than those of the ambient corona at solar-$y = 1003''$and $1015''$. Late in the plume's life, the densities reduce to being only 50 % higher than the background at the base and only 10 % higher than the background at high altitudes.

This decrease over time may affect also the observability of plumes in the interplanetary medium. The issue of the plume survival at large heliocentric distances has been debated for years, but the identification of plumes with distant solar wind structures, such as Pressure Balanced Structures (McCo-

mas et al., 1996; Poletto et al., 1996) or microstreams (Neugebauer, 2012), has not yet been universally accepted. If our observations show behavior typical of all plumes, then plumes have a high density only over a limited fraction of their lifetime, and so detection of a specific plume at interplanetary distances may be easier (or less-difficult) only over a portion of that plume's life.

According to Wang (1998), plumes acquire a high density as a consequence of the evaporation of material triggered by reconnection-induced energy deposition, and eventually decay by radiative cooling. Assuming, as in Wang (1998), an evaporation time $\tau_{ev} \approx L/u$, where L is a vertical dimension and u a characteristic flow speed, the formation of the plume a couple of hours after the BP implies $u \approx 6$ km s^{-1}, which seems acceptable. The radiative cooling time, τ_{rad}, is given by $\tau_{rad} \approx 3p/(2n^2\Lambda)$, where Λ is the radiative loss function and p the plasma pressure; for $T_e \approx 10^6$ K, $\Lambda \approx 10^{-22}$ g s^{-3} cm^5 (Priest, 1984). Assuming $n \approx 3.1 \times 10^8$ cm^{-3}, it turns out that $\tau_{rad} \approx 3$ h, which is a little longer than the time-lag between the disappearance of the BP and the time when the plume blends with the background (see Fig. 6.3). We don't know the reason for this discrepancy, but we point out that the lifetime of the BP might be longer, in case the fraction of its area behind the limb survives its visible side component, although at a very low radiance level.

Why does the plume fluctuate independently of the BP fluctuations? A possibility is that the BP brightens in response to reconnection episodes at its magnetic base. Looking at Fig. 6.1, panels B and C, the many loops that show up in different locations seem to indicate that the BP base field could be made up of a number of magnetic fragments of each polarity that, later on, emerge, converge and annihilate, eventually leading to the (loops and) BP disappearance (von Rekowski & Hood, 2008). The plume, on the other hand, likely originates from reconnection between the BP and the ambient unipolar field, and this process is not necessarily related to the process leading to the BP's fluctuations.

6.5.2 Outflows in plumes and background regions

As mentioned in section 6.3, the outflow speed of disturbances seen in the space-time maps has been often compared with the sound speed, to check whether the observed events might be interpreted as signatures of magneto-acoustic upward propagating waves. Such waves would be expected to induce spectral-line radiance oscillations traveling with a speed equal to or lower than the sound speed (Edwin & Roberts, 1983). Recently, Krishna Prasad et al. (2011) and Gupta et al. (2012), on the basis of, respectively, AIA and

SUMER data, present evidence supporting this scenario. Because Gupta et al. (2012) used data in the 171 Å and 193 Å AIA channels, their results are more easily compared with our work. These authors conclude that the characteristics of the observed events comply with the wave requirements, as the observed ratio of the propagating speed of the disturbances in the 171 Å and 193 Å channels is close enough to its theoretically-expected value (1.19 in their observations compared to 1.25 in the theory). If we take into account the temperature of maximum emission in CHs and quiet Sun (which should be representative enough of the plume conditions) given by O'Dwyer et al. (2010) for the 171 Å and 193 Å channels, the expected theoretical ratio may be a little higher. However, Gupta et al. (2012) themselves warn the reader that the alternative upflowing events scenario cannot be ruled out unless coordinated observations (combining imaging and spectroscopic data) become available.

In our analysis the magnetoacoustic wave hypothesis is not tenable, because the 171 Å perturbations have a higher propagation speed than the 193 Å events. The reason for this discrepancy is not clear. It may originate from the fainter jets, which were not included in the analysis of Gupta et al. (2012), but which in our work are the jets with higher propagation speeds. Hence, we are led to favor the interpretation of McIntosh et al. (2010) and Tian et al. (2011) who from, respectively, STEREO and AIA data, conclude that the observed disturbances represent high-speed outflows.

Tian et al. (2011) do not give the outflow speed distributions in different AIA channels, and the distribution they show peaks at a somewhat lower value ($\approx 130\,\mathrm{km\,s^{-1}}$ vs. $167\,\mathrm{km\,s^{-1}}$) than our 171 Å distribution (see Fig. 6.6). If we consider events in all AIA channels we get a mean speed of 150 km $\mathrm{s^{-1}}$, in good agreement with Tian et al. (2011), being within the Gaussian width (30 km $\mathrm{s^{-1}}$) of their distribution. We should also consider that the upward speed may show some variability, depending on the individual data set being analyzed. We point out that the occurrence rate and the speed distribution of propagating disturbances do not depend on the age of our plume, as both remain about constant as the plume approaches the time of its disappearance (see Fig. 6.7).

An interesting issue that has been mentioned, although briefly, also by Tian et al. (2011), is the occurrence of upflowing events in the background interplume corona. Fig. 6.6 (bottom row) gives our measurements of the speed distribution of the 171 Å and 193 Å upflow events in the background corona. A comparison of this with the top row analogous plume distributions of Fig. 6.6 reveals that, apart from a lower number of events, there is no major difference between the plume and interplume distributions of the 193 Å channel while in the 171 Å channel the peak value of the background

corona outflow speed distribution is somewhat lower. Furthermore, both distributions (plume and interplume) do not show any temperature dependence of the outflow speed. Because the background ambient corona has a lower density than the plume, we do not know whether the interplume regions host fewer events, or whether their detection is more difficult due to their lower-density environment. A detailed analysis of this problem is beyond the aim of this presentation. If however future studies substantiate that upflows occur in the ambient corona, the implications for those upflows as solar wind sources, and their implications for plume-versus-interplume contributions to the solar wind, should be re-considered. Solar minimum conditions, when the occurrence of bright features along the Sun-Earth LOS is minimized, are a better fit for these types of investigations.

We cannot say from our data whether the observed events reach high heliocentric distances and feed the solar wind. If we assume they do, we may give an upper estimate of the mass contributed by the disturbances to the wind. We will assume plumes covering some 10 % of a typical polar CH extending down to a 70° latitude; this percentage occupation (Ahmad & Withbroe, 1977) is probably an upper limit to the actual coverage of plumes. If upflows rise from the whole plume area - a further unknown factor - with a characteristic speed of 100 km s^{-1} and a density of 10^8 cm^{-3}, it turns out that about 60 % of the wind mass may originate from plumes within one polar coronal hole. However, not knowing how much of the plume area is outflowing, nor knowing out to what distance from the Sun the outflows persist and if plasma accelerates enough to escape from the sun, this figure may be easily affected by one order of magnitude uncertainty (or even more, should outflows die within a short distance from the limb). We point out that the work of Llebaria et al. (2002), where plume trajectories and plume speeds have been followed over time intervals of the order of hours and out to heliocentric distances of the order of a few solar radii, suggest that plume outflows may actually contribute substantially to the solar wind.

A further factor that might be used to understand whether plumes contribute to solar wind, is the comparison of their First Ionization Potential (FIP) bias with that measured in fast wind (von Steiger et al., 2000). According to some workers (Widing & Feldman, 1992; Wilhelm & Bodmer, 1998; Curdt et al., 2008), the FIP bias in plumes differs enough from that of the fast wind to rule the plumes out as fast-wind contributors. It is however fair to say that the issue is not completely settled, as Del Zanna et al. (2003) claim there is no significant fractionation in plumes. As our data are not fit for an abundance analysis we do not deal any further with this issue.

6.5.3 Physical parameters of plumes

The values of densities given in Table 6.1 and the temperatures we quote in section 6.4 are more or less consistent with values inferred by other authors. Possibly, the slightly higher value of the ambient coronal temperature in our analysis results from data being acquired inside a small hole, when the LOS is likely affected by features along the LOS-integration path. What is worth noting however is that our inferred plume temperatures remain approximately unchanged over the lifetime of the plume, as this implies that plumes die due to a density reduction over time, at least for the single plume examined here.

This result, together with the observed lack of change with time in the occurrence of outflows, may lead to a scenario where plumes, at least those associated with BPs, are sort of a 'bush' residing above a base that is powered by reconnection episodes; those episodes would be triggered more frequently than elsewhere by the BP magnetic fields. The reconnections would lead to high-density plasma evaporation, making plumes denser and better visible than the surrounding ambient corona. Under this scenario, outflows we observe as low-level radiance enhancements may represent the outcome of reconnections that are relatively energetic compared to the comparatively-gentle magnetic events occurring in nearby surrounding areas of the CH, resulting in the plumes standing out in the ambient CH corona. As long as the BP magnetic field does not disperse or annihilate, reconnection events keep occurring. The 193 Å and 211 Å panels of Fig. 6.1 (panels B,C,E,F,H, I) suggest that the compact loops that are observed early in the lifetime of the BP tend to grow fainter, and possibly wider, as time goes by. This may indicate that the BP base fields become more sparse: over time, we likely are lead to more sparse evaporating episodes and, hence, to a decrease in the overall plume's density and, eventually, to the plume death as the BP base fields fade and become indistinguishable from the coronal background ambient fields. We surmise that individual evaporating episodes may keep occurring all through the plume lifetime, but their number decreases with time, until they become as few and weak as we observe in the background corona.

Chapter 7

Conclusions and Future Work

In this Thesis several high quality data sets from different imaging instruments onboard of *Hinode*, *Stereo* and *SDO* missions have been analysed in order to study and characterize transient phenomena within CHs. A deeper understanding of these small scale but energetic and recurrent coronal features is fundamental in order to estimate the overall energy contribution of CHs to the corona and their mass supply to the fast solar wind.

The main results of the three years study have been here presented as three separate works, each focussing on a different transient phenomenon that can be observed within CHs: X-ray BPs, polar coronal jets and coronal plumes.

In the first work two long and continuous data sets from the *Hinode*/XRT have been analysed to study the intensity variabilities of multiple BPs and their relationship with the nearby occurrence of coronal jets. We found, in conjunction with coronal jets, evidences for activity propagation among multiple BPs. We suggested a new interpretation for these, at least apparent, propagation phenomena, in which slow brightenings of the whole BP complex are due to gradual phenomena related to emergence or cancellation of bipolar magnetic fields. On the other hand, sudden changes of the scenario, namely sharp BP intensity maxima and jets, result from connectivity variations that are triggered when a magnetic field stability threshold is reached, often at the interface between the bipolar emerging field and the unipolar ambient field. In these abrupt sequences a relative large amount of magnetic energy can be released and converted into either thermal or kinetic energy.

Differences in the magnetic configuration before such stability threshold is reached are the discriminating factors for the type of ejection that occurs. In the second work we have performed a physical parameter analysis of the two main types of coronal jets that can be observed within a CH, the so called standard and blowout jets. Data obtained mainly from *Hinode* XRT and

STEREO EUVI have allowed us to infer temperatures, densities and outflow speeds as a function of time and distance along the axis for the two analysed jets. We found our blowout jet being slightly hotter than the standard jet, with faster outflows and multi-component structure. All these factors lead us to conclude that the energy required to fuel the blowout eruption is approximately ten times larger than that for the standard jet. Basing our speculation on these samples we suggested that the blowout events originate in those regions within CH that are characterized by stronger magnetic fields. This fact, together with the COR1 observations of the studied events (see Fig. 5.12), might suggest that blowout jets, compared to standard eruptions, have a higher probability to escape into the heliosphere and to contribute to the fast solar wind.

Once the dimension, the density and the outflow speed of the jet plasma have been measured it is possible to give an upper estimate of the mass flux that jets of the two types transport to the solar wind and, assuming a given frequency of events, to infer a value for the wind mass loading contributed by polar jets (see Pucci et al., 2013, for a detailed analysis). Because there are insufficient data to establish the percentage of ejections which eventually fall back to the Sun and because the jets we analyzed in our second work are probably among the more energetic within their respective class of events, the estimate we give is an upper limit to the jet wind mass loading. We use the physical parameters measured for standard and blowout jets (see table 5.1), with the assumption that 2/3 of the total number of jets belong to the standard category (Moore et al., 2010). The base width of standard and/or blowout jets varies in between 2×10^3 km and 2×10^4 km, and the lifetime of blowout is estimated to be twice as long as the lifetime of standard events, which is on the order of 700 s. Combining this data with the rate of jet event per day (60–240) that can be obtained from the literature (Cirtain et al., 2007; Savcheva et al., 2007), we get the following values for the mass flux ($\mathrm{cm}^{-2}\ \mathrm{s}^{-1}$) at the Earth distance:

- Minimum mass flux
  - for standard jets = $4.6 \times 10^4\ \mathrm{cm}^{-2}\ \mathrm{s}^{-1}$
  - for blowout jets = $1.4 \times 10^5\ \mathrm{cm}^{-2}\ \mathrm{s}^{-1}$
- Maximum mass flux
  - for standard jets = $2.4 \times 10^7\ \mathrm{cm}^{-2}\ \mathrm{s}^{-1}$
  - for blowout jets = $7.2 \times 10^7\ \mathrm{cm}^{-2}\ \mathrm{s}^{-1}$

In the lower limit the obtained values are negligible compared to the known solar wind mass flux ($\approx 2 \times 10^8$ cm^{-2} s^{-1}) while the sum of standard and blowout contribution gives approximately one-half of the solar wind in the upper limit. We can conclude that if jets contribute to the solar wind, blowout eruotions play a prevailing role compared with standard ones. However, if we consider that some jets fall back to the Sun (Culhane et al., 2007) and that our test cases are likely to be among the brightest jets of their category, we conclude that the contribution to the wind mass flux from X-ray jets likely is not significant. In other words, X-ray jets seem to be not capable, by their own mass loading alone, to fuel the wind mass flux.

In the third work we have studied the other CH feature that have been studied since the first observations of the corona and hence soon related with the origin of the fast solar wind: the polar plumes. This third work has been based on extremely high quality data obtained from the *SDO* AIA instrument. The focus has been posed on: studying the relationship between the selected long lasting plume and a BP at its base, finding the physical properties of the plume plasma and their evolution with time and, finally, estimating the plume's mass supply to the solar wind.

We found that the plume and the BP in which the plume is rooted appear and disappear almost simultaneously. Nevertheless, these two CH features undergo intensity fluctuations which are clearly not related with each other. We have suggested that this different behavior can be explained considering the fact that the birth of the plume is probably due to reconnection between the bipolar field of the BP and the unipolar ambient field. On the other hand, gradual fluctuations of the BP are mostly due to the emergence of the bipolar field, as described in our first work, and are not strictly related with the previous process.

Adopting DEM techniques we measured plume plasma densities and temperatures during the plume evolution, finding values that agree with literature. At the end of the plume life we found a clear decrease of the density (see table 6.1) while temperature seems to remain quite constant. We thus suggested that the plume disappearing is due to a density decrease induced by fewer reconnection events at its base.

The analysis of detrended space-time maps builded in different AIA channels has shown that our plume hosts upward propagating disturbances with a mean speed of ≈ 150 km s^{-1}, ruling out the hypothesis of magnetoacoustic waves. Assuming that the observed outflows reach high heliocentric distances and feed the solar wind, and under the assumption that plumes cover about 10% of a typical CH extending down to a 70° latitude, we have shown in section 6.5.2 that the mass flux at 1 AU of the solar wind originating in plumes reaches more than 1×10^8 cm^{-2} s^{-1}, accounting for about 60 % of the total

solar wind mass flux.

Comparing the results from the second and the third work we can conclude that both plumes and jets fade out because of a density decrease and not due to cooling processes. Furthermore, while jets seems not to be able to contribute significantly to the solar wind mass flux, plumes, and the sorrounding interplumes regions, may probably play a key role as mass supplier.

As mentioned in chapter 6, some authors (see e.g. Raouafi et al., 2008) controversially claim that X-ray jets are the precursors of plumes. The data analysed in our work does not allow us to deeper investigate the relationship between these two CH feature. We are planning to combine XRT jet observations with AIA plumes images to understand how the occurrence of X-ray jets are related with the formation or the disappearence of plumes. Furthermore, we would like to study the plumes evolution within an equatorial CH, which gives the opportunity to compare the EUV images obtained with AIA with simultaneous magnetograms from the Helioseismic and Magnetic Imager on board of the SDO missions. From these comparison we would be able to confirm our hypotesis about how gradual and abrupt changes in magnetic topology influences the different CHs feature that we have studied in this work.

On a longer time scale, the launch of the *Solar Orbiter* mission (Müller et al., 2013), scheduled for 2017, will open great opportunities to observe CH from a totally new point of view. Going down to 0.28 astronomical unit from the Sun, the *Solar Orbiter* will observe the Sun and the solar corona from a tilted orbit providing wonderful new observations of the polar CHs and of its features.

Acknowledgements

First of all I would like to thank Giannina Poletto for her guidance through these four years of studies at the Arcetri Astrophysical Observatory and at the University of Firenze. I really feel lucky to could work with Giannina who has supported me through my first steps in this research field and whose encouragement has been fundamental for my professional and personal growth.

I thank my supervisor Marco Romoli for all the help I continuously received and for being a model and an example to imitate.

Next I thank Federico Landini for his infinite patience in solving or just listening to my scientific or personal problems.

I wish to thank Maurizio Pancrazzi, Mauro Focardi and Roberto Baglioni for the friendly environment that I have found at Arcetri and that I have really enjoyed during these years.

I thank Alphonse C. Sterling for his continuos and irreplaceable scientific support in writing all the papers.

My thanks go also to the referees and to all those people who have read the articles and this thesis for their helpful comments that lead to an improvement of my work.

Finally, special thanks go to my wife Iselin, my children Erika, Sira, Benjamin and to my parents Giovannella and Marco for their invaluable support and affection.

Stefano Pucci

Bibliography

Ahmad, I. A., & Withbroe, G. L. 1977, *EUV analysis of polar plumes*, Sol. Phys., 53, 397

Arnaud, M., & Rothenflug, R. 1985, *An updated evaluation of recombination and ionization rates*, A&AS, 60, 425

Aschwanden, M. J., Nitta, N. V., Wuelser, J.-P., & Lemen, J. R. 2008, *First 3D Reconstructions of Coronal Loops with the STEREO A+B Spacecraft. II. Electron Density and Temperature Measurements*, ApJ, 680, 1477

Asplund, M., Grevesse, N., Sauval, A. J., Allende Prieto, C., & Kiselman, D. 2004, *Line formation in solar granulation. IV. [O I], O I and OH lines and the photospheric O abundance*, A&A, 417, 751

Balogh, A., & Forsyth, R. J. 1998, *The Results of the ULYSSES Mission: A Survey of the Heliosphere in Three Dimensions*, in ESA Special Publication, Vol. 417, Crossroads for European Solar and Heliospheric Physics. Recent Achievements and Future Mission Possibilities, 45

Boerner, P. F., Testa, P., Warren, H., Weber, M. A., & Schrijver, C. J. 2014, *Photometric and Thermal Cross-calibration of Solar EUV Instruments*, Sol. Phys., 289, 2377

Bohlin, J. D., Frost, K. J., Burr, P. T., Guha, A. K., & Withbroe, G. L. 1980, *Solar Maximum Mission*, Sol. Phys., 65, 5

Bradshaw, S. J., & Mason, H. E. 2003, *The radiative response of solar loop plasma subject to transient heating*, A&A, 407, 1127

Brueckner, G. E., Howard, R. A., Koomen, M. J., et al. 1995, *The Large Angle Spectroscopic Coronagraph (LASCO)*, Sol. Phys., 162, 357

Carroll, B. W., & Ostlie, D. A. 1996, *An Introduction to Modern Astrophysics*, Pearson Addison-Wesley

Chandrashekhar, K., Krishna Prasad, S., Banerjee, D., Ravindra, B., & Seaton, D. B. 2013, *Dynamics of Coronal Bright Points as Seen by Sun Watcher Using Active Pixel System Detector and Image Processing (SWAP), Atmospheric Imaging Assembly (AIA), and Helioseismic and Magnetic Imager (HMI)*, Sol. Phys., 286, 125

Chen, H.-D., Zhang, J., & Ma, S.-L. 2012, *The kinematics of an untwisting solar jet in a polar coronal hole observed by SDO/AIA*, Research in Astronomy and Astrophysics, 12, 573

Cirtain, J. W., Golub, L., Lundquist, L., et al. 2007, *Evidence for Alfvén Waves in Solar X-ray Jets*, Science, 318, 1580

Culhane, L., Harra, L. K., Baker, D., et al. 2007, *Hinode EUV Study of Jets in the Sun's South Polar Corona*, PASJ, 59, 751

Curdt, W., Wilhelm, K., Feng, L., & Kamio, S. 2008, *Multi-spacecraft observations of polar coronal plumes*, A&A, 481, L61

Deforest, C. E., Hoeksema, J. T., Gurman, J. B., et al. 1997, *Polar Plume Anatomy: Results of a Coordinated Observation*, Sol. Phys., 175, 393

DeForest, C. E., Lamy, P. L., & Llebaria, A. 2001, *Solar Polar Plume Lifetime and Coronal Hole Expansion: Determination from Long-Term Observations*, ApJ, 560, 490

Del Zanna, G., Bromage, B. J. I., & Mason, H. E. 2003, *Spectroscopic characteristics of polar plumes*, A&A, 398, 743

Domingo, V., Fleck, B., & Poland, A. I. 1995, *The SOHO Mission: an Overview*, Sol. Phys., 162, 1

Doschek, G. A., Landi, E., Warren, H. P., & Harra, L. K. 2010, *Bright Points and Jets in Polar Coronal Holes Observed by the Extreme-Ultraviolet Imaging Spectrometer on Hinode*, ApJ, 710, 1806

Drake, J. J., Cohen, O., Yashiro, S., & Gopalswamy, N. 2013, *Implications of Mass and Energy Loss due to Coronal Mass Ejections on Magnetically Active Stars*, ApJ, 764, 170

Edwin, P. M., & Roberts, B. 1983, *Wave propagation in a magnetic cylinder*, Sol. Phys., 88, 179

Emslie, A. G., Dennis, B. R., Shih, A. Y., et al. 2012, *Global Energetics of Thirty-eight Large Solar Eruptive Events*, ApJ, 759, 71

Feldman, U. 1992, *Elemental abundances in the upper solar atmosphere.*, Phys. Scr, 46, 202

Feldman, U., & Widing, K. G. 2003, *Elemental Abundances in the Solar Upper Atmosphere Derived by Spectroscopic Means*, Space Sci. Rev., 107, 665

Filippov, B., Golub, L., & Koutchmy, S. 2009, *X-Ray Jet Dynamics in a Polar Coronal Hole Region*, Sol. Phys., 254, 259

Friedman, H. 1963, *U. S. Naval Research Laboratory Report*, AJ, 68, 678

Gabriel, A. H., Bely-Dubau, F., & Lemaire, P. 2003, *The Contribution of Polar Plumes to the Fast Solar Wind*, ApJ, 589, 623

Golub, L., Krieger, A. S., Harvey, J. W., & Vaiana, G. S. 1977, *Magnetic properties of X-ray bright points*, Sol. Phys., 53, 111

Golub, L., Krieger, A. S., Silk, J. K., Timothy, A. F., & Vaiana, G. S. 1974, *Solar X-Ray Bright Points*, ApJ, 189, L93

Golub, L., & Pasachoff, J. M. 1997, *"The Solar Corona"*, "Cambridge University Press"

Golub, L., Deluca, E., Austin, G., et al. 2007, *The X-Ray Telescope (XRT) for the Hinode Mission*, Sol. Phys., 243, 63

Grevesse, N., & Sauval, A. J. 1998, *Standard Solar Composition*, Space Sci. Rev., 85, 161

Gupta, G. R., Teriaca, L., Marsch, E., Solanki, S. K., & Banerjee, D. 2012, *Spectroscopic observations of propagating disturbances in a polar coronal hole: evidence of slow magneto-acoustic waves*, A&A, 546, A93

Habbal, S. R., Withbroe, G. L., & Dowdy, Jr., J. F. 1990, *A comparison between bright points in a coronal hole and a quiet-sun region*, ApJ, 352, 333

Hannah, I. G., & Kontar, E. P. 2012, *Differential emission measures from the regularized inversion of Hinode and SDO data*, A&A, 539, A146

Howard, R. A., Moses, J. D., Vourlidas, A., et al. 2008, *Sun Earth Connection Coronal and Heliospheric Investigation (SECCHI)*, Space Sci. Rev., 136, 67

Kaiser, M. L., Kucera, T. A., Davila, J. M., et al. 2008, *The STEREO Mission: An Introduction*, Space Sci. Rev., 136, 5

Kano, R., Hara, H., Shimojo, M., et al. 2004, *SolarB X-Ray Telescope (XRT)*, in Astronomical Society of the Pacific Conference Series, Vol. 325, The Solar-B Mission and the Forefront of Solar Physics, ed. T. Sakurai & T. Sekii, 15

Kariyappa, R., Deluca, E. E., Saar, S. H., et al. 2011, *Temperature variability in X-ray bright points observed with Hinode/XRT*, A&A, 526, A78

Kariyappa, R., & Varghese, B. A. 2008, *Intensity oscillations and heating of the coronal X-ray bright points from Hinode/XRT*, A&A, 485, 289

Kim, Y.-H., Moon, Y.-J., Park, Y.-D., et al. 2007, *Small-Scale X-Ray/EUV Jets Seen in Hinode XRT and TRACE*, PASJ, 59, 763

Kimura, H., & Mann, I. 1998, *Brightness of the solar F-corona*, Earth, Planets, and Space, 50, 493

Kosugi, T., Matsuzaki, K., Sakao, T., et al. 2007, *The Hinode (Solar-B) Mission: An Overview*, Sol. Phys., 243, 3

Krishna Prasad, S., Banerjee, D., & Gupta, G. R. 2011, *Propagating intensity disturbances in polar corona as seen from AIA/SDO*, A&A, 528, L4

Lemen, J. R., Title, A. M., Akin, D. J., et al. 2012, *The Atmospheric Imaging Assembly (AIA) on the Solar Dynamics Observatory (SDO)*, Sol. Phys., 275, 17

Lin, J., Ko, Y.-K., Sui, L., et al. 2005, *Direct Observations of the Magnetic Reconnection Site of an Eruption on 2003 November 18*, ApJ, 622, 1251

Liu, C., Deng, N., Liu, R., et al. 2011, *A Standard-to-blowout Jet*, ApJ, 735, L18

Llebaria, A., Saez, F., & Lamy, P. 2002, *The fractal nature of the polar plumes*, in ESA Special Publication, Vol. 508, From Solar Min to Max: Half a Solar Cycle with SOHO, ed. A. Wilson, 391–394

Lundquist, C. A. 1979, *Skylab's astronomy and space sciences*, NASA Special Publication, 404

Machado, M. E., Moore, R. L., Hernandez, A. M., et al. 1988, *The observed characteristics of flare energy release. I - Magnetic structure at the energy release site*, ApJ, 326, 425

Madjarska, M. S. 2011, *Dynamics and plasma properties of an X-ray jet from SUMER, EIS, XRT, and EUVI A & B simultaneous observations*, A&A, 526, A19

Mártínez Pillet, V., Aparicio, A., & Sánchez, F. 2005, *Payload and Mission Definition in Space Sciences*

Mazzotta, P., Mazzitelli, G., Colafrancesco, S., & Vittorio, N. 1998, *Ionization balance for optically thin plasmas: Rate coefficients for all atoms and ions of the elements H to NI*, A&AS, 133, 403

McComas, D. J., Hoogeveen, G. W., Gosling, J. T., et al. 1996, *ULYSSES observations of pressure-balance structures in the polar solar wind.*, A&A, 316, 368

McIntosh, S. W., Innes, D. E., de Pontieu, B., & Leamon, R. J. 2010, *STEREO observations of quasi-periodically driven high velocity outflows in polar plumes*, A&A, 510, L2

Moore, R. L., Cirtain, J. W., Sterling, A. C., & Falconer, D. A. 2010, *Dichotomy of Solar Coronal Jets: Standard Jets and Blowout Jets*, ApJ, 720, 757

Moore, R. L., Sterling, A. C., Falconer, D. A., & Robe, D. 2013, *The Cool Component and the Dichotomy, Lateral Expansion, and Axial Rotation of Solar X-Ray Jets*, ApJ, 769, 134

Moreno-Insertis, F., Galsgaard, K., & Ugarte-Urra, I. 2008, *Jets in Coronal Holes: Hinode Observations and Three-dimensional Computer Modeling*, ApJ, 673, L211

Morton, R. J., Srivastava, A. K., & Erdélyi, R. 2012, *Observations of quasi-periodic phenomena associated with a large blowout solar jet*, A&A, 542, A70

Müller, D., Marsden, R. G., St. Cyr, O. C., & Gilbert, H. R. 2013, *Solar Orbiter . Exploring the Sun-Heliosphere Connection*, Sol. Phys., 285, 25

Narukage, N., Sakao, T., Kano, R., et al. 2011, *Coronal-Temperature-Diagnostic Capability of the Hinode/ X-Ray Telescope Based on Self-Consistent Calibration*, Sol. Phys., 269, 169

Neugebauer, M. 2012, *Evidence for Polar X-Ray Jets as Sources of Microstream Peaks in the Solar Wind*, ApJ, 750, 50

Nisticò, G., Patsourakos, S., Bothmer, V., & Zimbardo, G. 2011, *Determination of temperature maps of EUV coronal hole jets*, Advances in Space Research, 48, 1490

Noci, G., Kohl, J. L., & Withbroe, G. L. 1987, *Solar wind diagnostics from Doppler-enhanced scattering*, ApJ, 315, 706

O'Dwyer, B., Del Zanna, G., Mason, H. E., Weber, M. A., & Tripathi, D. 2010, *SDO/AIA response to coronal hole, quiet Sun, active region, and flare plasma*, A&A, 521, A21

Ogawara, Y., Takano, T., Kato, T., et al. 1991, *The SOLAR-A Mission - An Overview*, Sol. Phys., 136, 1

Pariat, E., Antiochos, S. K., & DeVore, C. R. 2009, *A Model for Solar Polar Jets*, ApJ, 691, 61

Pasachoff, J. M., Rušin, V., Druckmüller, M., et al. 2009, *The 2008 August 1 Eclipse Solar-Minimum Corona Unraveled*, ApJ, 702, 1297

Patsourakos, S., Pariat, E., Vourlidas, A., Antiochos, S. K., & Wuelser, J. P. 2008, *STEREO SECCHI Stereoscopic Observations Constraining the Initiation of Polar Coronal Jets*, ApJ, 680, L73

Pesnell, W. D., Thompson, B. J., & Chamberlin, P. C. 2012, *The Solar Dynamics Observatory (SDO)*, Sol. Phys., 275, 3

Plowman, J., Kankelborg, C., & Martens, P. 2013, *Fast Differential Emission Measure Inversion of Solar Coronal Data*, ApJ, 771, 2

Poletto, G., Gary, G. A., & Machado, M. E. 1993, *Interactive flare sites within an active region complex*, Sol. Phys., 144, 113

Poletto, G., Parenti, S., Noci, G., et al. 1996, *Searching for coronal plumes in ULYSSES observations of the far solar wind.*, A&A, 316, 374

Priest, E., & Forbes, T., eds. 2000, *Magnetic reconnection : MHD theory and applications*

Priest, E. R. 1984, *Solar magneto-hydrodynamics*, Geophysics and Astrophysics Monographs, Dordrecht: Reidel, 1984

Pucci, S., Poletto, G., Sterling, A. C., & Romoli, M. 2013, *An upper limit to the solar wind mass loading by X-ray polar jets*, in American Institute of Physics Conference Series, Vol. 1539, 62–65

Raouafi, N.-E., Petrie, G. J. D., Norton, A. A., Henney, C. J., & Solanki, S. K. 2008, *Evidence for Polar Jets as Precursors of Polar Plume Formation*, ApJ, 682, L137

Reisenfeld, D. B., McComas, D. J., & Steinberg, J. T. 1999, *Evidence of a solar origin for pressure balance structures in the high-latitude solar wind*, Geophys. Res. Lett., 26, 1805

Riley, P., Lionello, R., Mikić, Z., et al. 2007, *"Bursty" Reconnection Following Solar Eruptions: MHD Simulations and Comparison with Observations*, ApJ, 655, 591

Rosner, R., Tucker, W. H., & Vaiana, G. S. 1978, *Dynamics of the quiescent solar corona*, ApJ, 220, 643

Russell, H. N. 1929, *On the Composition of the Sun's Atmosphere*, ApJ, 70, 11

Sakao, T., Kano, R., Narukage, N., et al. 2007, *Continuous Plasma Outflows from the Edge of a Solar Active Region as a Possible Source of Solar Wind*, Science, 318, 1585

Savcheva, A., Cirtain, J., Deluca, E. E., et al. 2007, *A Study of Polar Jet Parameters Based on Hinode XRT Observations*, PASJ, 59, 771

Schettino, G., Poletto, G., & Romoli, M. 2009, *UV Transient Brightenings Associated with a Coronal Mass Ejection*, ApJ, 697, L72

Schou, J., Scherrer, P., Bush, R., et al. 2012, *Design and Ground Calibration of the Helioseismic and Magnetic Imager (HMI) Instrument on the Solar Dynamics Observatory (SDO)*, Solar Physics, 275, 229

Scullion, E., Popescu, M. D., Banerjee, D., Doyle, J. G., & Erdélyi, R. 2009, *Jets in Polar Coronal Holes*, ApJ, 704, 1385

Shen, Y., Liu, Y., Su, J., & Deng, Y. 2012, *On a Coronal Blowout Jet: The First Observation of a Simultaneously Produced Bubble-like CME and a Jet-like CME in a Solar Event*, ApJ, 745, 164

Shibata, K., Ishido, Y., Acton, L. W., et al. 1992, *Observations of X-ray jets with the YOHKOH Soft X-ray Telescope*, PASJ, 44, L173

Shimojo, M., Hashimoto, S., Shibata, K., et al. 1996, *Statistical Study of Solar X-Ray Jets Observed with the YOHKOH Soft X-Ray Telescope*, PASJ, 48, 123

Shimojo, M., & Shibata, K. 2000, *Physical Parameters of Solar X-Ray Jets*, ApJ, 542, 1100

Sterling, A. C., Harra, L. K., & Moore, R. L. 2010, *Fibrillar Chromospheric Spicule-like Counterparts to an Extreme-ultraviolet and Soft X-ray Blowout Coronal Jet*, ApJ, 722, 1644

Teriaca, L., Poletto, G., Romoli, M., & Biesecker, D. A. 2003, *The Nascent Solar Wind: Origin and Acceleration*, ApJ, 588, 566

Tian, H., McIntosh, S. W., Habbal, S. R., & He, J. 2011, *Observation of High-speed Outflow on Plume-like Structures of the Quiet Sun and Coronal Holes with Solar Dynamics Observatory/Atmospheric Imaging Assembly*, ApJ, 736, 130

Tian, H., Tu, C., Marsch, E., He, J., & Kamio, S. 2010, *The Nascent Fast Solar Wind Observed by the EUV Imaging Spectrometer on Board Hinode*, ApJ, 709, L88

Vaiana, G. S., Krieger, A. S., Van Speybroeck, L. P., & Zehnpfennig, T. 1970, Bull. Am. Phys. Soc., 15, 611

van Beek, H. F., Hoyng, P., Lafleur, B., & Simnett, G. M. 1980, *The Hard X-ray Imaging Spectrometer /HXIS/*, Sol. Phys., 65, 39

van de Hulst, H. C. 1950, *On the polar rays of the corona (Errata: 11 VIII)*, Bull. Astron. Inst. Netherlands, 11, 150

von Rekowski, B., & Hood, A. W. 2008, *Solar coronal heating by magnetic cancellation - III. Thermodynamics*, MNRAS, 384, 972

von Steiger, R., Schwadron, N. A., Fisk, L. A., et al. 2000, *Composition of quasi-stationary solar wind flows from Ulysses/Solar Wind Ion Composition Spectrometer*, J. Geophys. Res., 105, 27217

Wang, Y.-M. 1998, *Network Activity and the Evaporative Formation of Polar Plumes*, ApJ, 501, L145

Wang, Y.-M., & Muglach, K. 2008, *Observations of Low-Latitude Coronal Plumes*, Sol. Phys., 249, 17

Widing, K. G., & Feldman, U. 1992, *Element abundances and plasma properties in a coronal polar plume*, ApJ, 392, 715

Wilhelm, K. 2006, *Solar coronal-hole plasma densities and temperatures*, A&A, 455, 697

Wilhelm, K., & Bodmer, R. 1998, *Solar EUV and UV Emission Line Observations Above a Polar Coronal Hole*, Space Sci. Rev., 85, 371

Wilhelm, K., Dammasch, I. E., Marsch, E., & Hassler, D. M. 2000, *On the source regions of the fast solar wind in polar coronal holes*, A&A, 353, 749

Wilhelm, K., Abbo, L., Auchère, F., et al. 2011, *Morphology, dynamics and plasma parameters of plumes and inter-plume regions in solar coronal holes*, A&A Rev., 19, 35

Woods, T., Eparvier, F., Hock, R., et al. 2012, *Extreme Ultraviolet Variability Experiment (EVE) ontheSolar Dynamics Observatory (SDO): Overviewof-Science Objectives, Instrument Design, DataProducts, and Model Developments*, Solar Physics, 275, 115

Wuelser, J.-P., Lemen, J. R., Tarbell, T. D., et al. 2004, *EUVI: the STEREO-SECCHI extreme ultraviolet imager*, in Society of Photo-Optical Instrumentation Engineers (SPIE) Conference Series, Vol. 5171, Telescopes and Instrumentation for Solar Astrophysics, ed. S. Fineschi & M. A. Gummin, 111–122

Yashiro, S., & Gopalswamy, N. 2009, *Statistical relationship between solar flares and coronal mass ejections*, in IAU Symposium, Vol. 257, IAU Symposium, ed. N. Gopalswamy & D. F. Webb, 233–243

Yokoyama, T., & Shibata, K. 1995, *Magnetic reconnection as the origin of X-ray jets and Hα surges on the Sun*, Nature, 375, 42

Young, P. R., Del Zanna, G., Landi, E., et al. 2003, *CHIANTI-An Atomic Database for Emission Lines. VI. Proton Rates and Other Improvements*, ApJS, 144, 135

Zhang, Q. M., Chen, P. F., Guo, Y., Fang, C., & Ding, M. D. 2012, *Two Types of Magnetic Reconnection in Coronal Bright Points and the Corresponding Magnetic Configuration*, ApJ, 746, 19